Figures and tables for

Determination of Metal Quality of Aluminium and Its Alloys

By

DERYA DISPINAR

A thesis submitted to
The University of Birmingham
For the degree of
DOCTOR OF PHILOSOPHY

School of Metallurgy and Materials
The University of Birmingham
January 2005

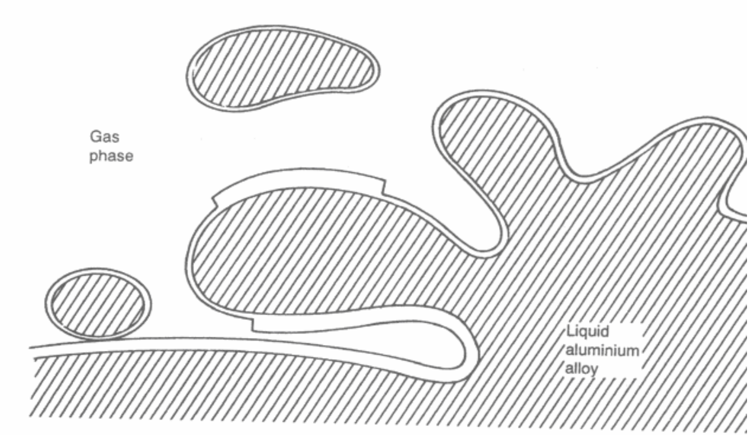

Figure 2.1: *Surface turbulence; probably the most common mechanism of introducing bifilm into the melt: The folding of the film, dry side to dry side, will trap gas between the surfaces[5]*

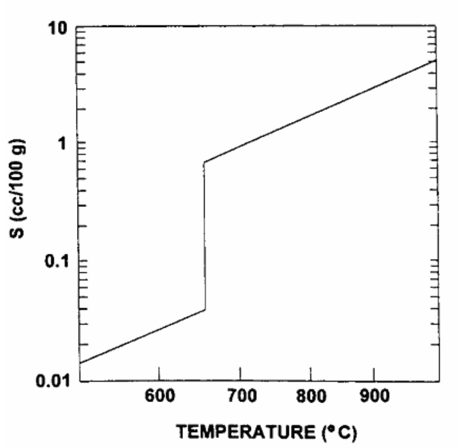

Figure 2.2: *Solubility of hydrogen in pure aluminium [34]*

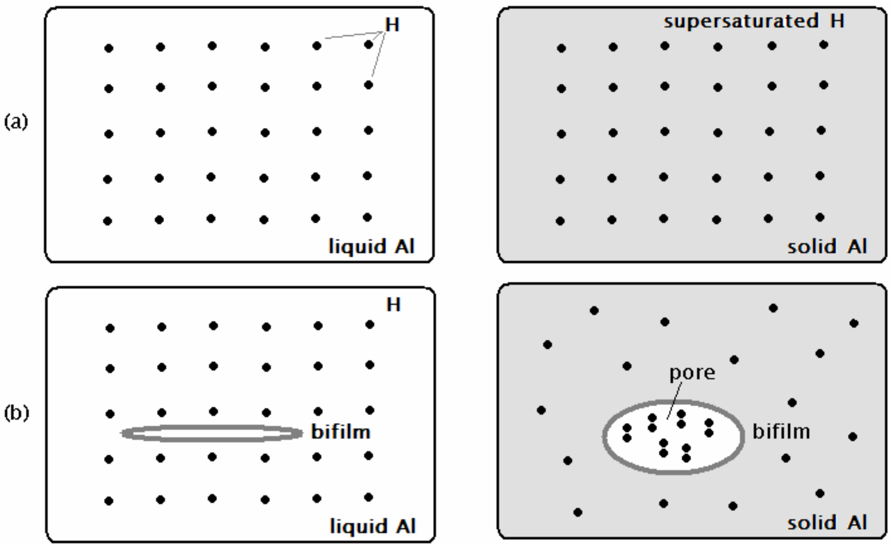

Figure 2.3: *(a) Supersaturation of hydrogen in the absence of bifilm*

(b) pore formation and diffusion of hydrogen into the gap between the bifilm

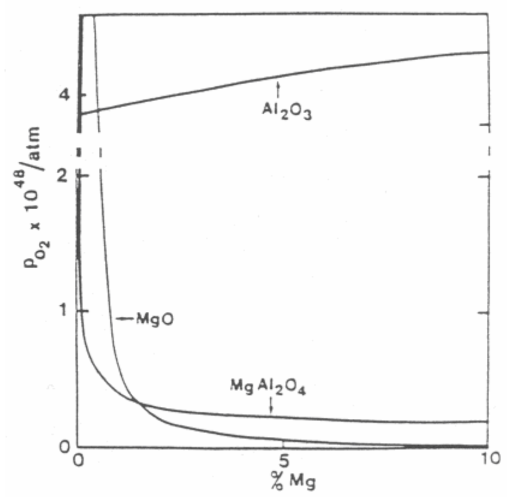

Figure 2.4: *Oxygen partial pressure and oxide structure[42]*

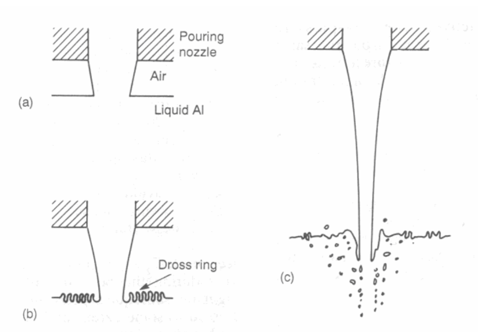

Figure 2.5: *the effect of increasing height on a falling stream of liquid [5];*
a) the oxide film remains intact,
b) the oxide film being detached and accumulating to form a dross ring,
c) the oxide film and air being entrained in the bulk melt

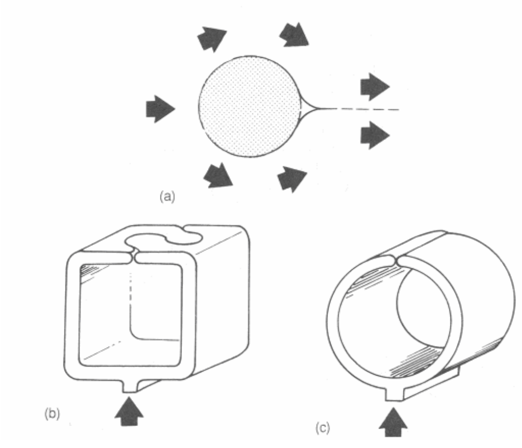

Figure 2.6: *confluence geometry: separation and rejoining involves the formation of films [5]*
a) at the side, b) randomly, c) on the top

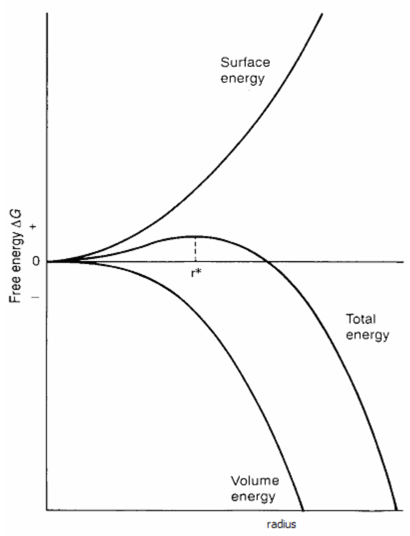

Figure 2.7: *Energies of a growing pore [5]*

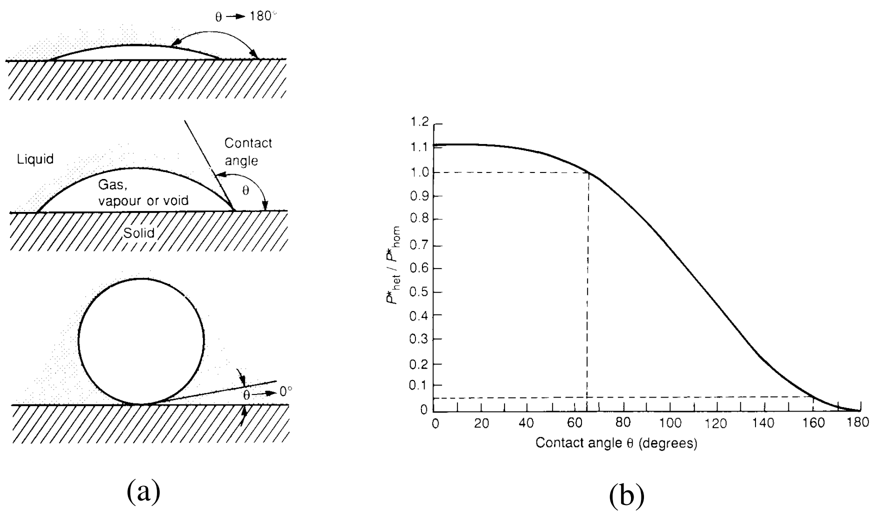

Figure 2.8: *Geometry of a bubble [5]: (a) wetting and contact angle between liquid and solid (b) energy association between homogeneous and heterogeneous nucleation*

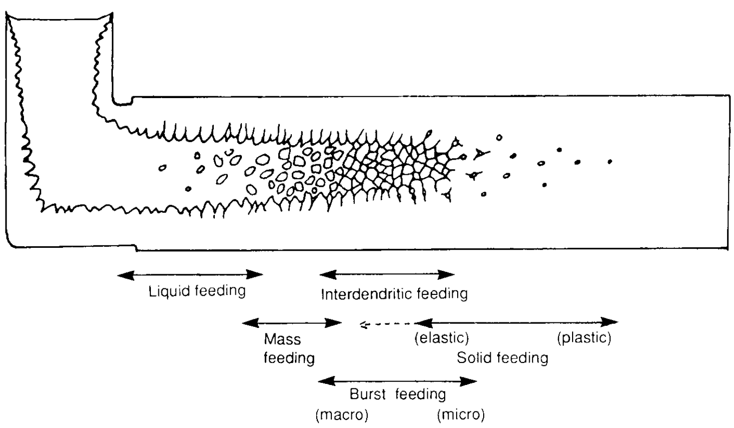

Figure 2.9: *Feeding mechanisms in a solidifying casting [5]*

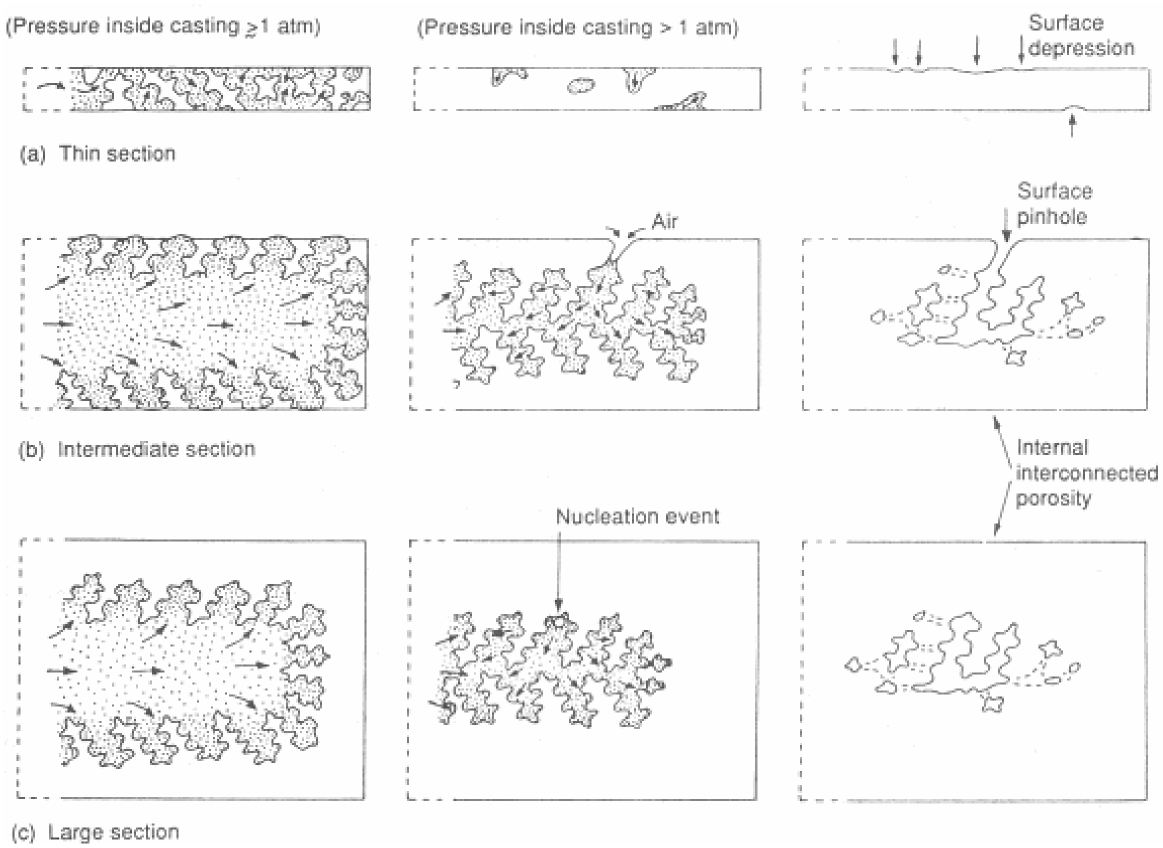

Figure 2.10: *Volumetric shrinkage in long freezing range alloy depending on the thickness of casting [5]*

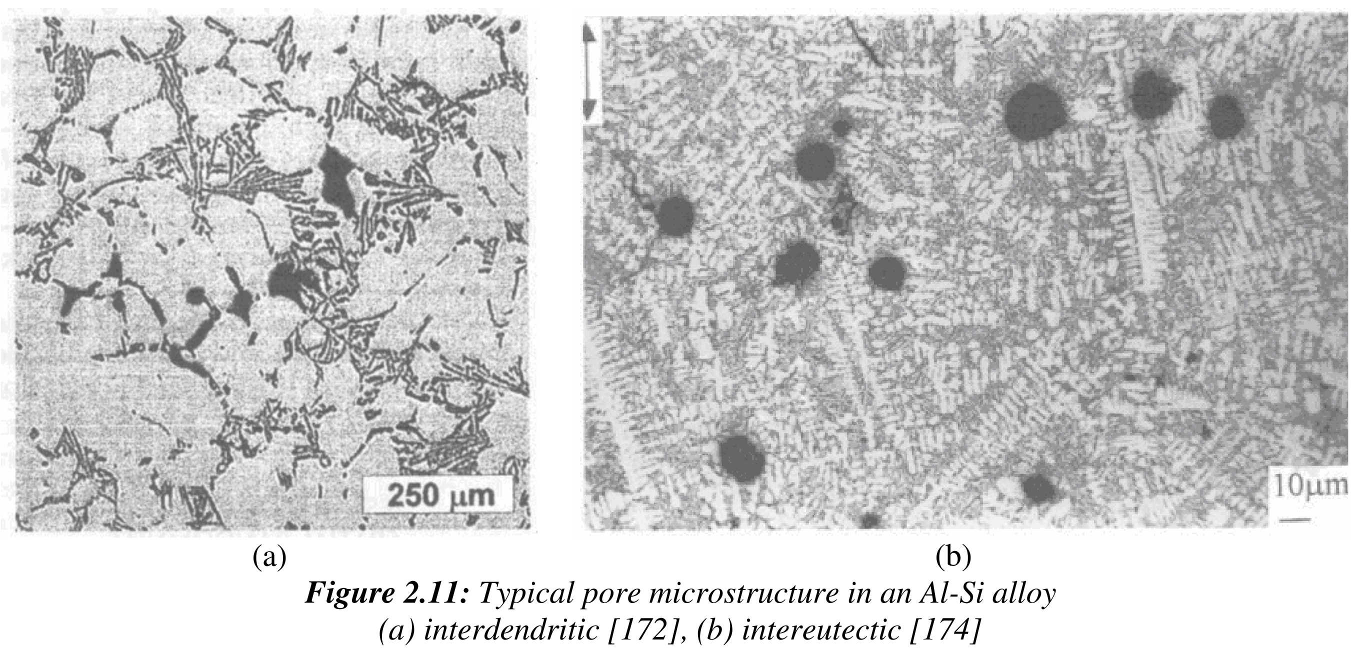

(a) (b)

Figure 2.11: *Typical pore microstructure in an Al-Si alloy (a) interdendritic [172], (b) intereutectic [174]*

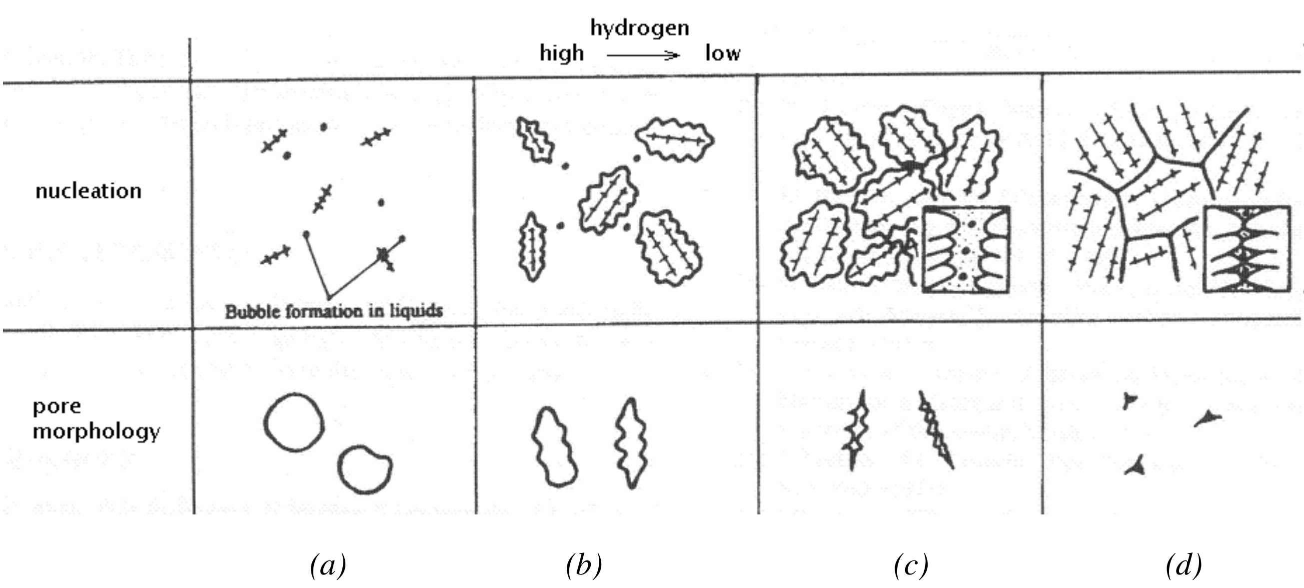

Figure 2.12: *Porosity morphology associated with the hydrogen level of the melt [88]*
(a) High hydrogen content: diffusion into bifilms starts in liquid
(b) High-medium hydrogen content: high liquid fraction
(c) Medium-low hydrogen content: growing in interdendritic structure
(d) Low hydrogen content: not enough driving force to expand the bifilms

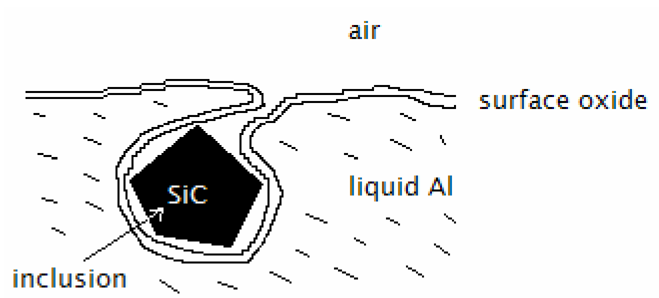

Figure 2.13: *Schematic demonstration of entrainment of an inclusion [5]*

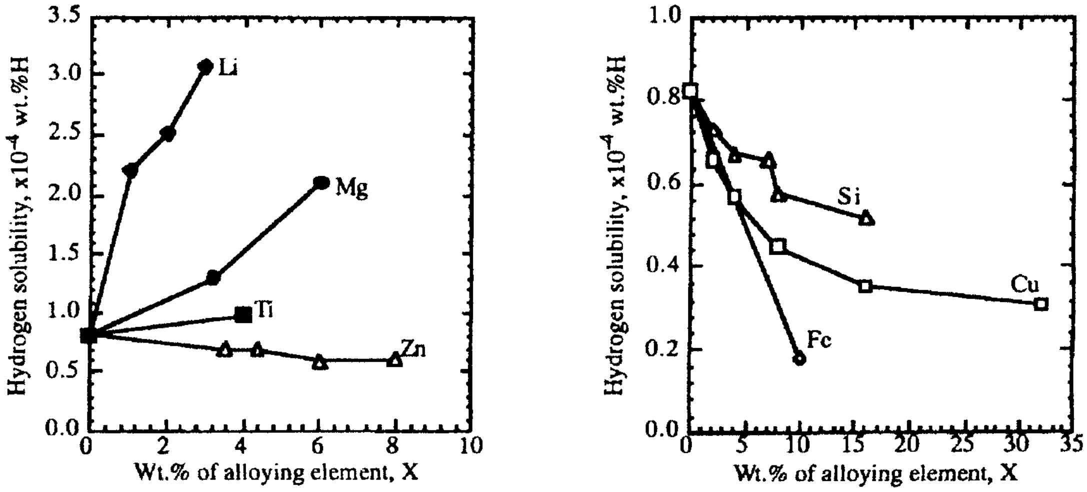

Figure 2.14: *Effects of alloying elements on hydrogen solubility in liquid Al at 973K, 1 atm partial pressure of hydrogen [36]*

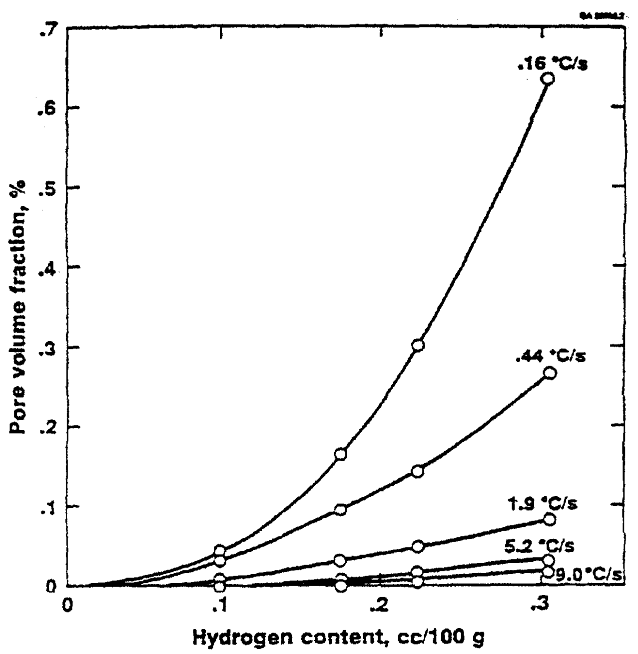

Figure 2.15: *The relation between porosity, hydrogen and cooling rate[80]*

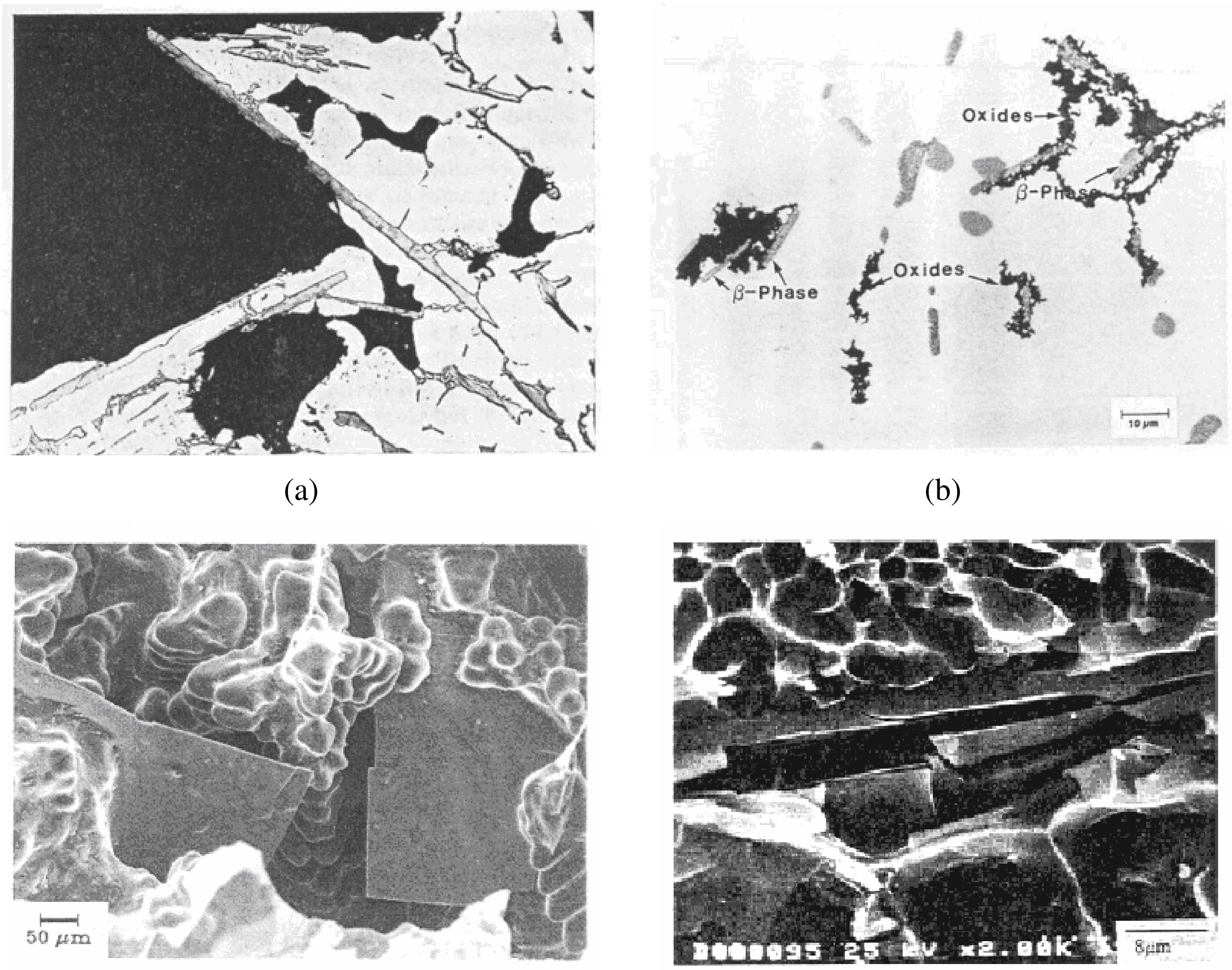

(a) (b)

(c) (d)

Figure 2.16: *Porosity formation and intermetallics:*
a) nucleating on bifilm [174], b) nucleation on oxides [211],
c) shrinkage and β-phase[215] , d) β-phase on oxide [105]

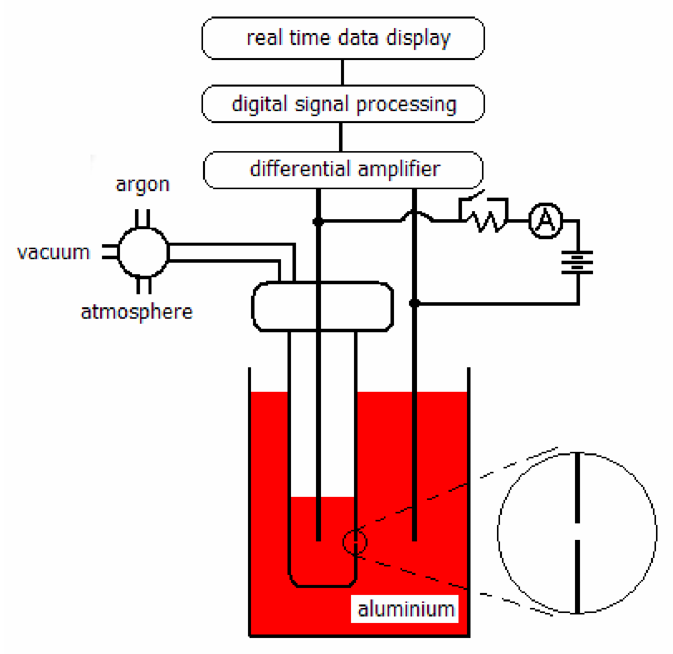

Figure 2.17: *Schematic representation of LiMCA [220]*

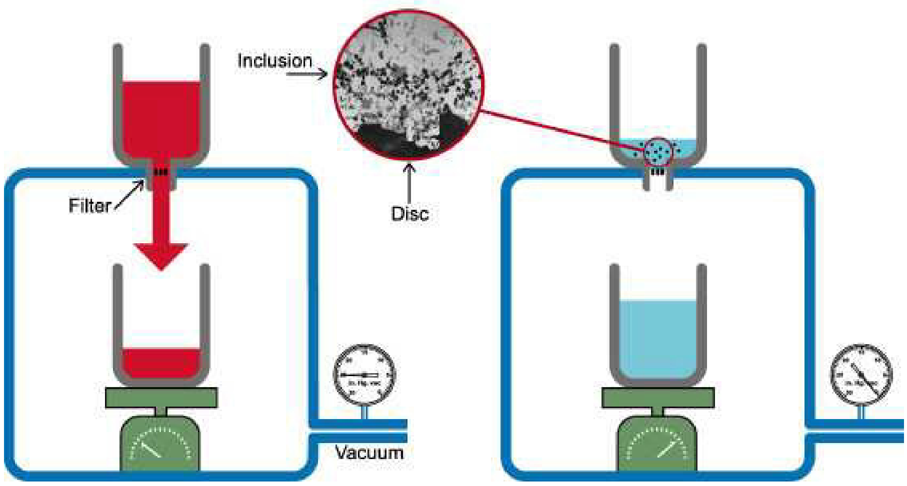

Figure 2.18: *Schematic representation of PoDFA test [220]*

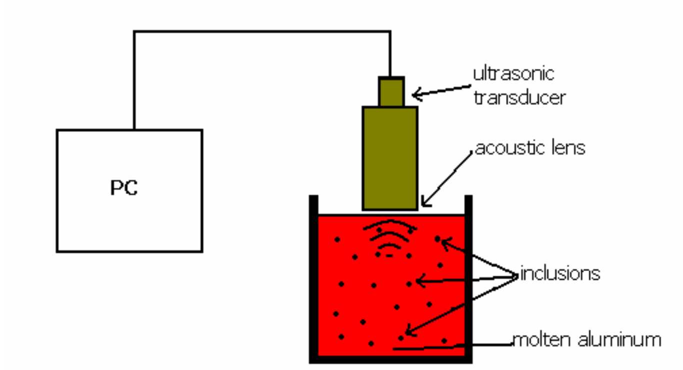

Figure 2.19: *Schematic diagram of ultrasonic technique*

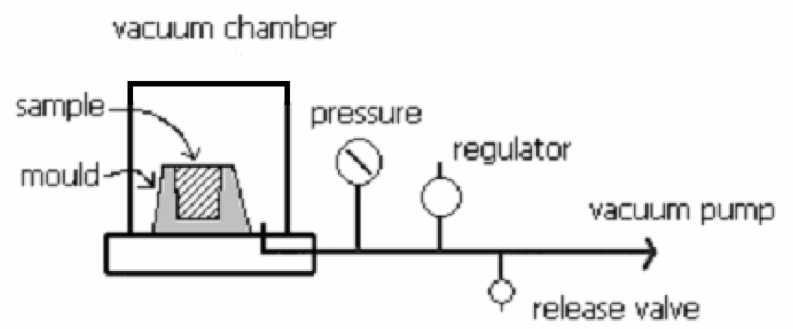

Figure 2.20: *Schematic RPT apparatus*

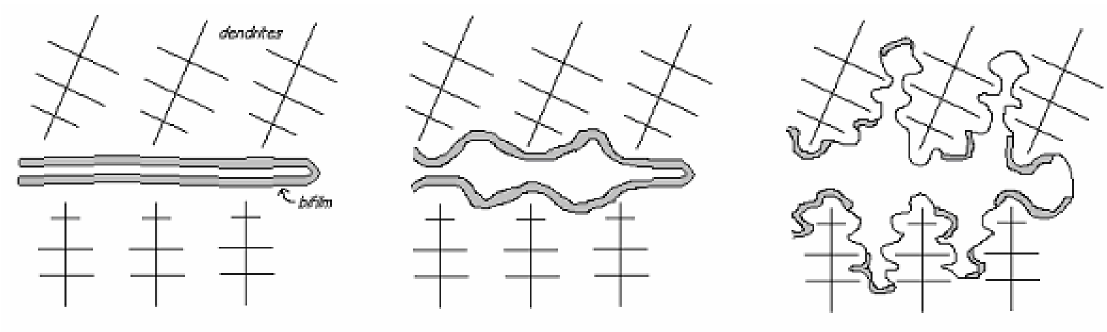

Figure 2.21: *bifilms and porosity formation [5]*

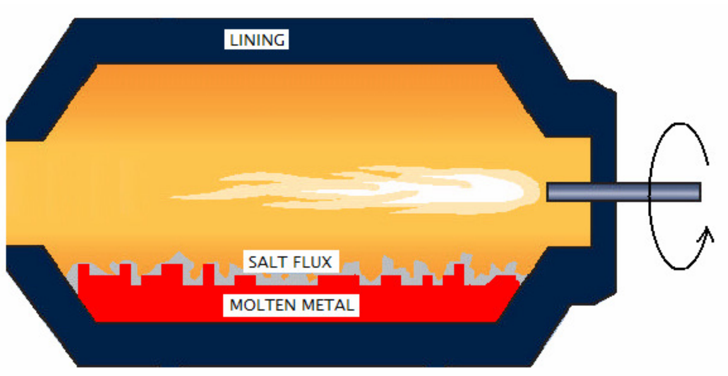

Figure 2.22: *Schematic section of a 5t capacity Rotary Furnace*

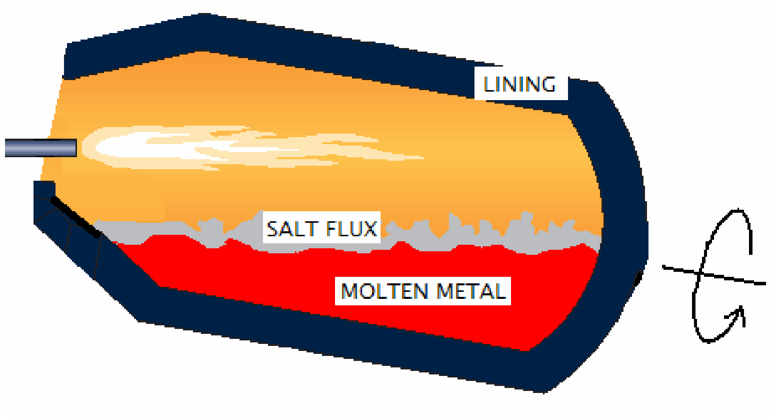

Figure 2.23: *Schematic drawing of Tilt Rotary Furnace*

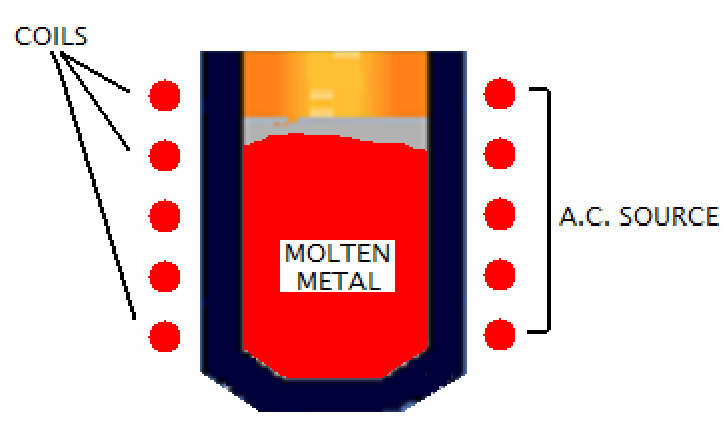

Figure 2.24: *Induction Furnace*

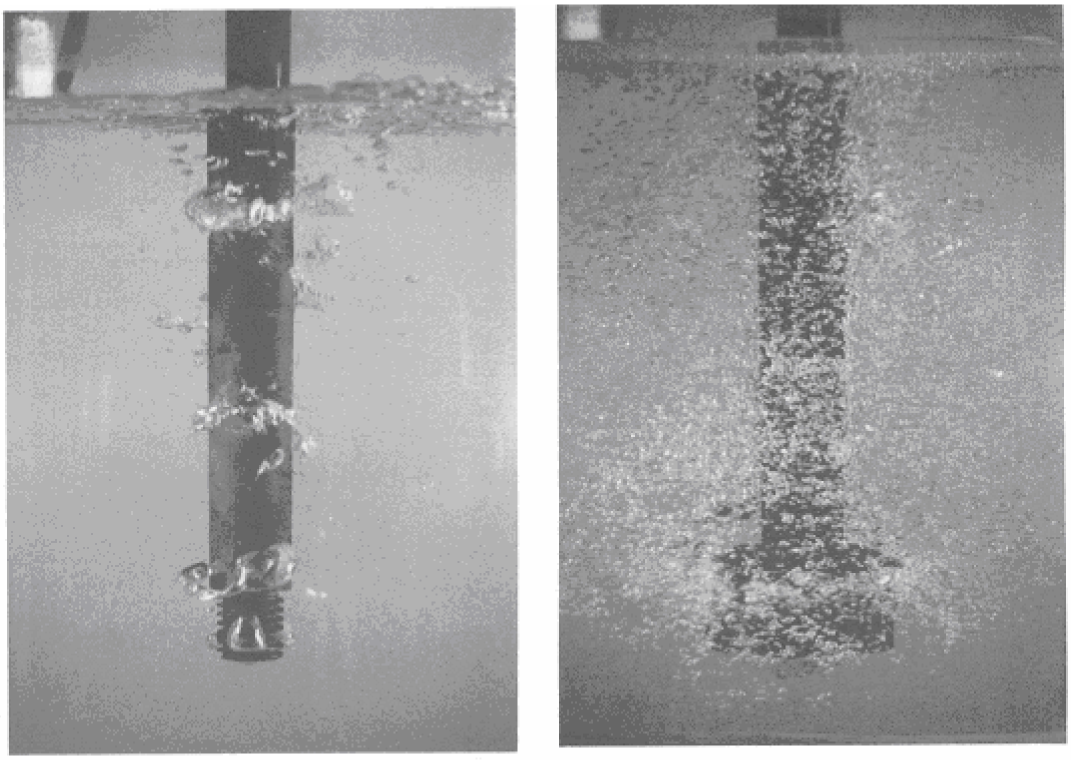

(a) (b)

Figure 2.25: *different type of degassers (illustrated by air in water) bubble size and distribution in a) lance, b) rotary degassing head [236]*

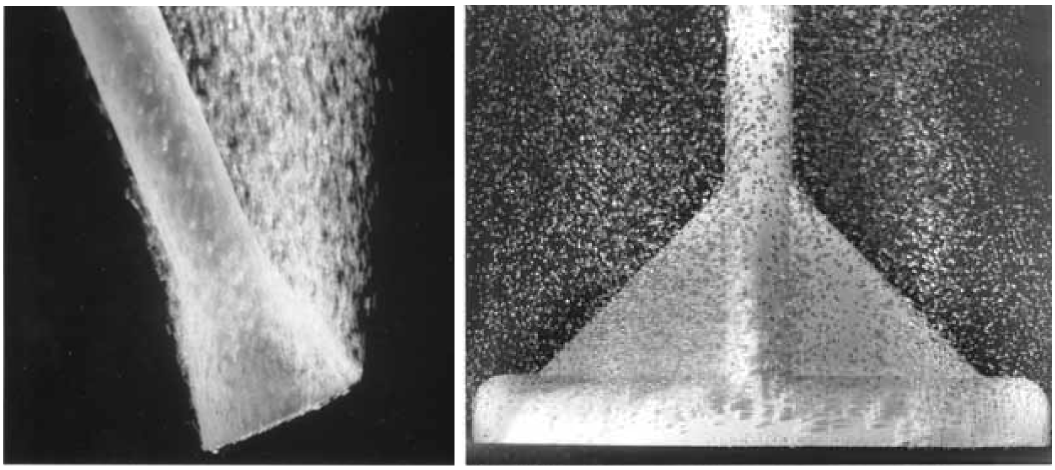

(a) (b)

Figure 2.26: *different type of diffusers (illustrated by the use of air bubbles in water) stationary ceramic diffusers a) disc-type, b) T-type [237]*

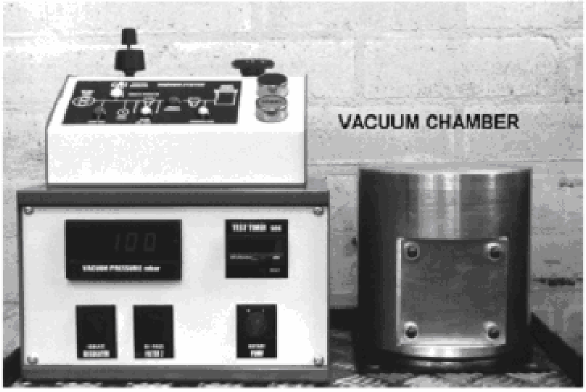

(a)

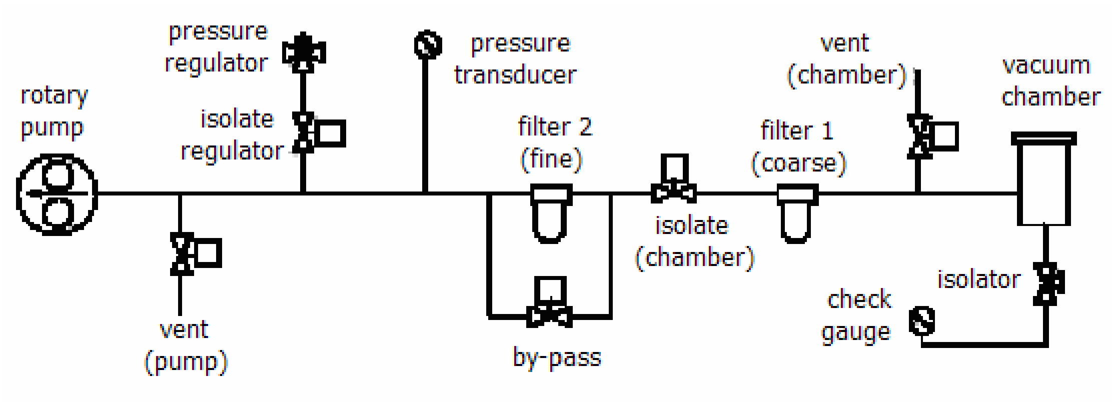

(b)

Figure 3.1: *(a) RPT machine and (b) schematic circuit drawing*

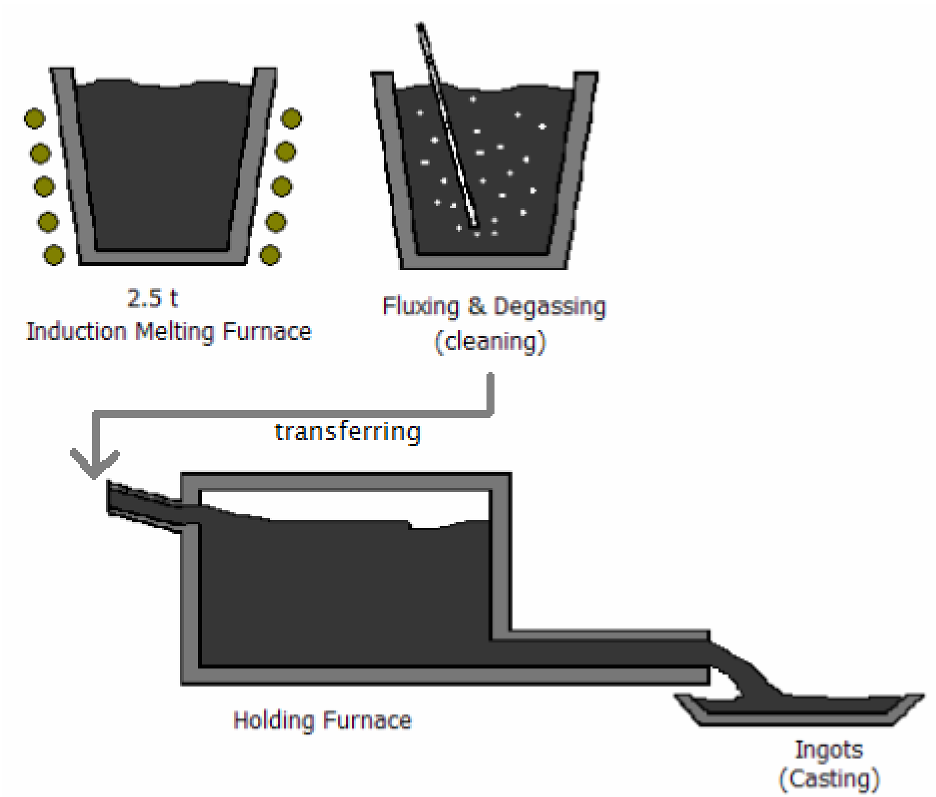

Figure 3.2: *a schematic representation of aluminium ingot production*

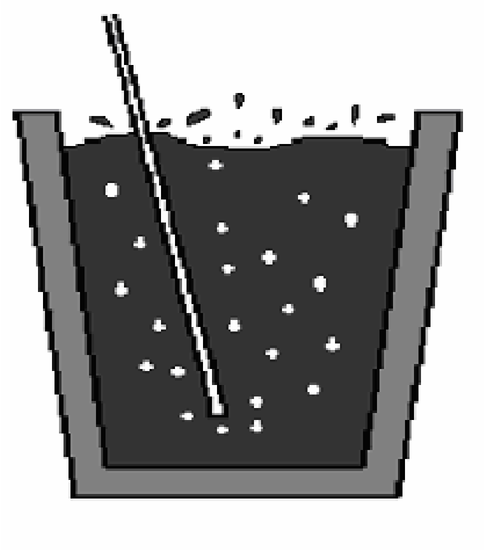

Figure 3.3: *schematically shown surface turbulence during fluxing and degassing*

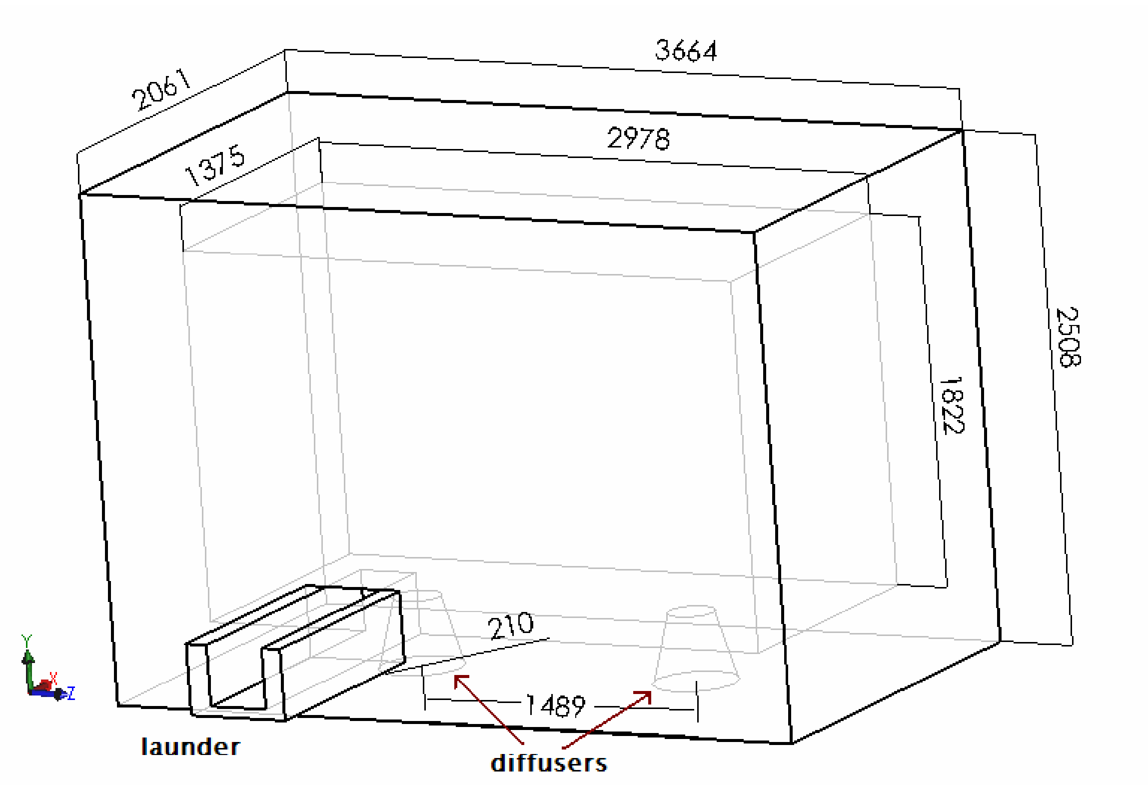

Figure 3.4: *Dimensions of the holding furnace and location of diffusers*

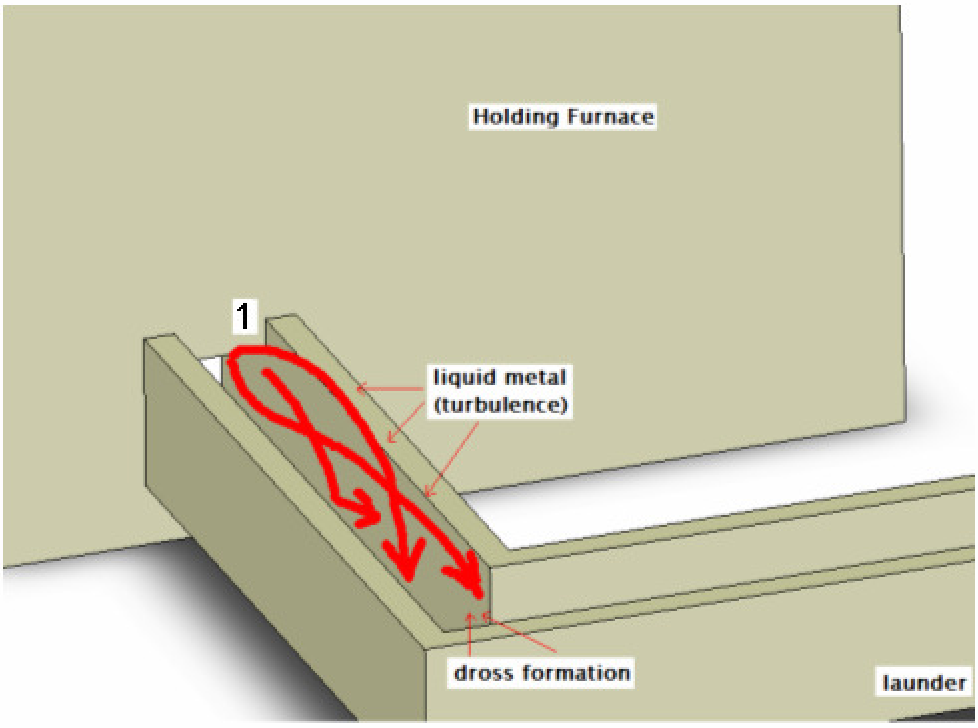

(a)

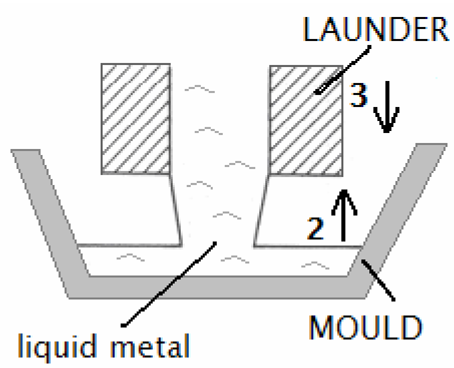

(b)

Figure 3.5: *Schematic illustration of changes made at the casting trials*

(a) - '1' More care was taken to avoid the severe turbulence on tapping.

(b) - '2' The launder was lowered to be as close to the casting mould possible

- '3' The casting and filling speed were decreased

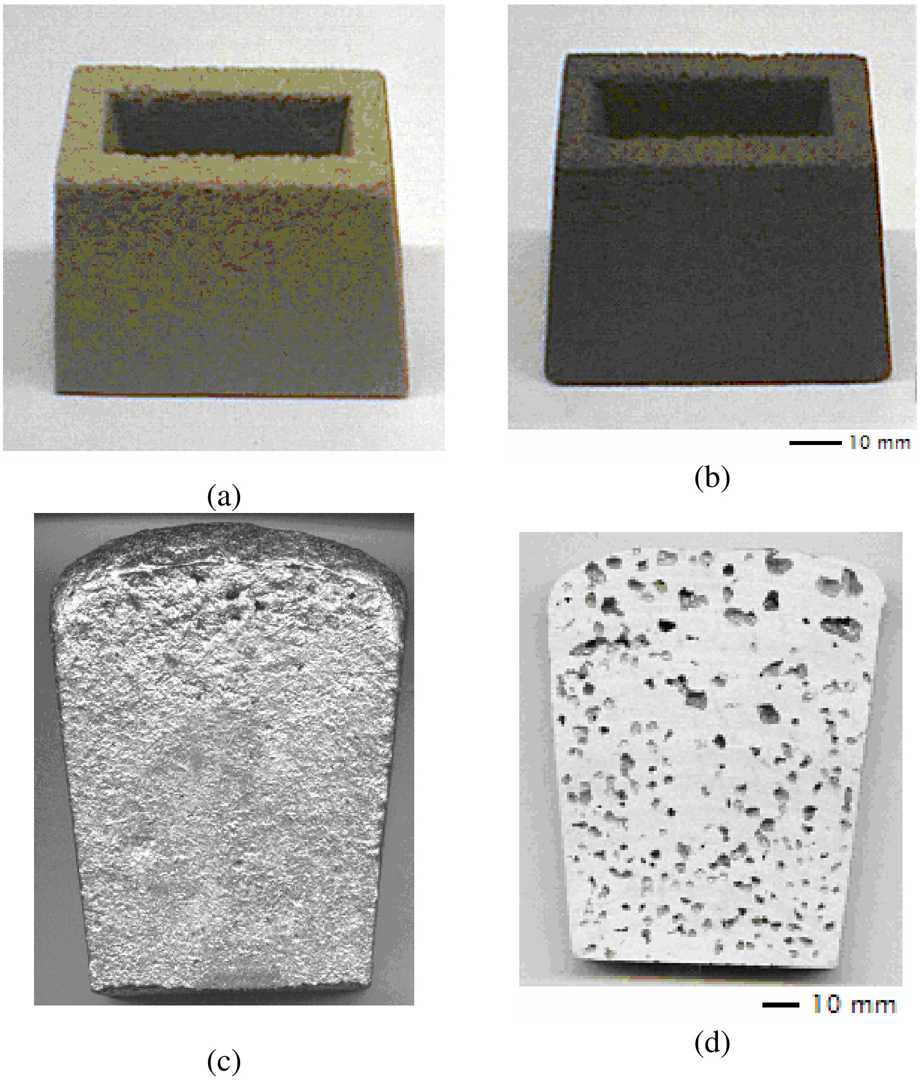

Figure 3.6: *Sand moulds that were used in RPT:*
a) resin binder,
b) sodium silicate + coal dust mixture;
and metal samples cast in the moulds
c) an outer view (50x35x15 mm);
d) a section through the centre.

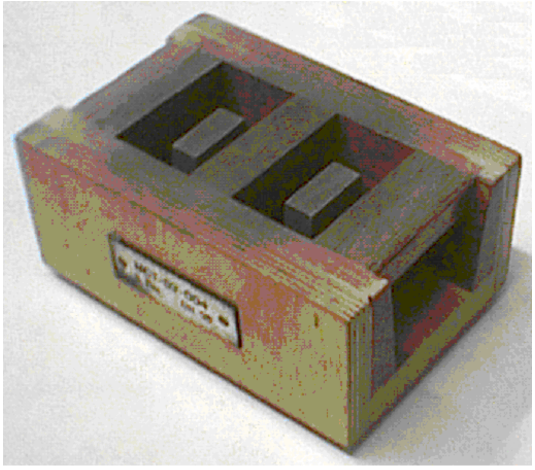

(a)

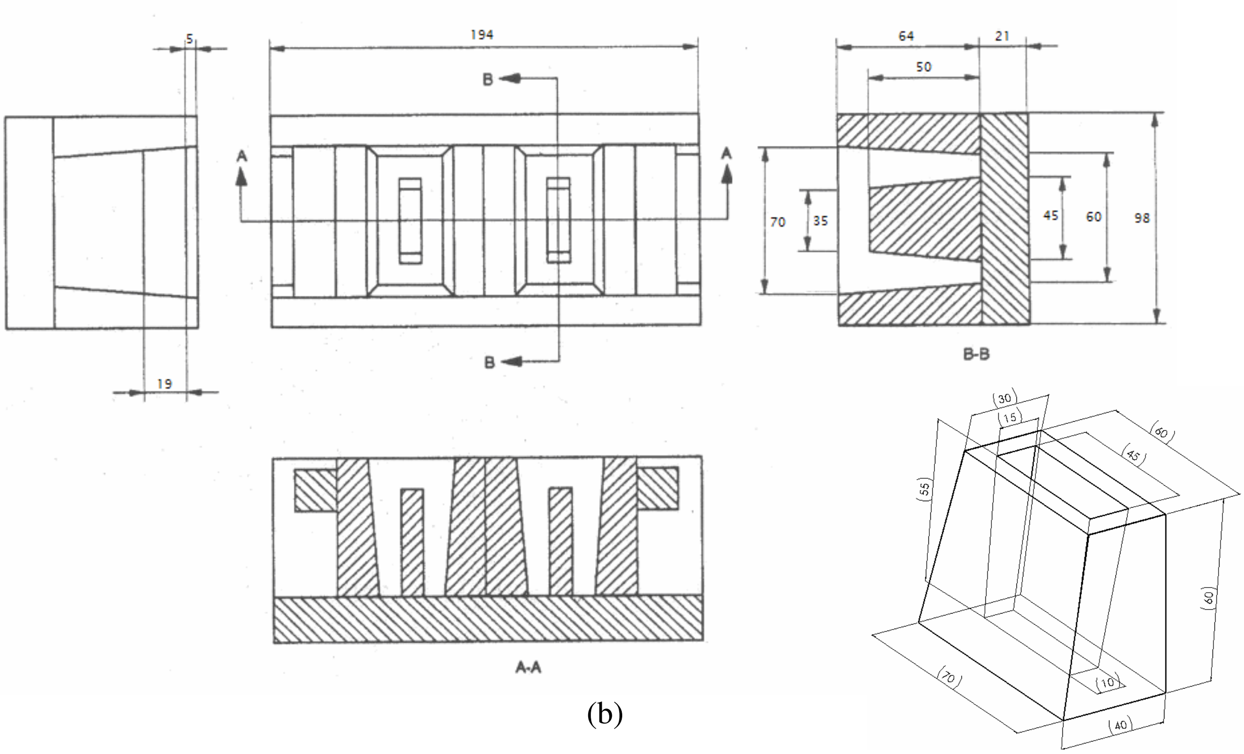

(b)

Figure 3.7: *Pattern design: (a) core box, (b) dimensions*

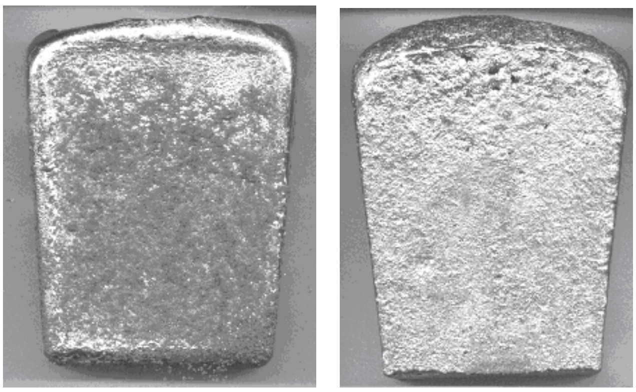

Figure 3.8: *a) sand particles adhered on surface of RPT sample, b) better surface finish with addition of coal dust*

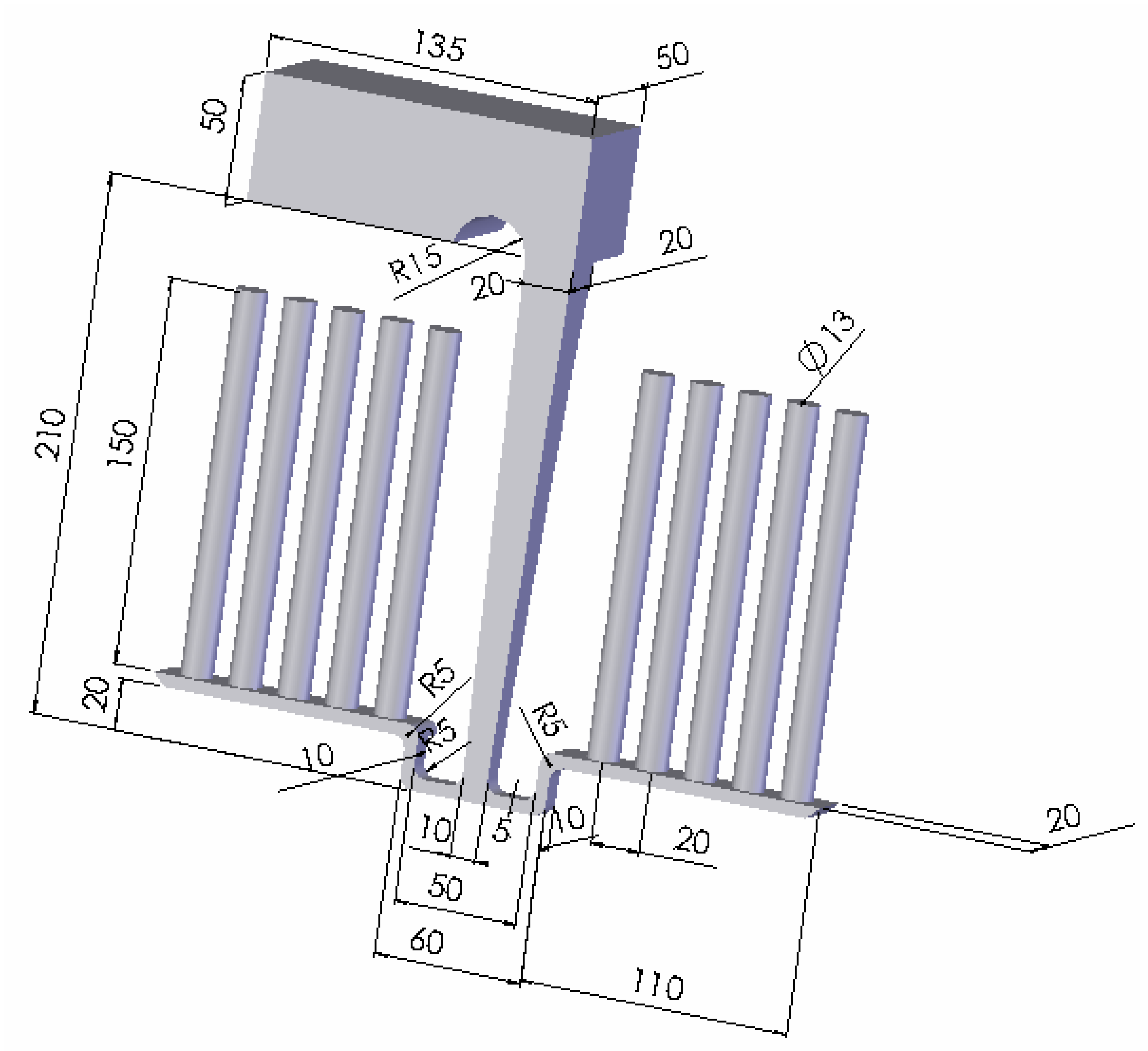

***Figure 3.9:** Schematic diagram of tensile test piece mould showing the dimensions of the optimised mould*

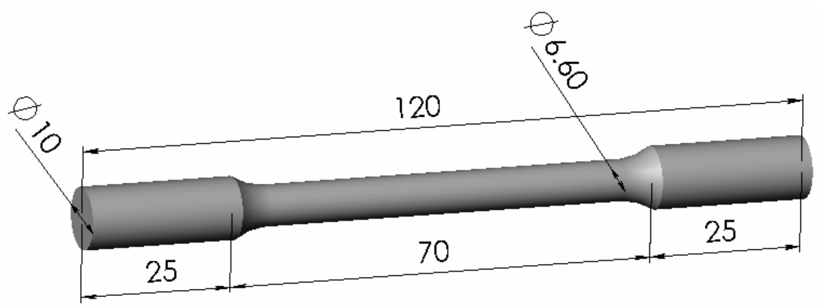

***Figure 3.10:** Tensile test bar dimensions used for mechanical tests*

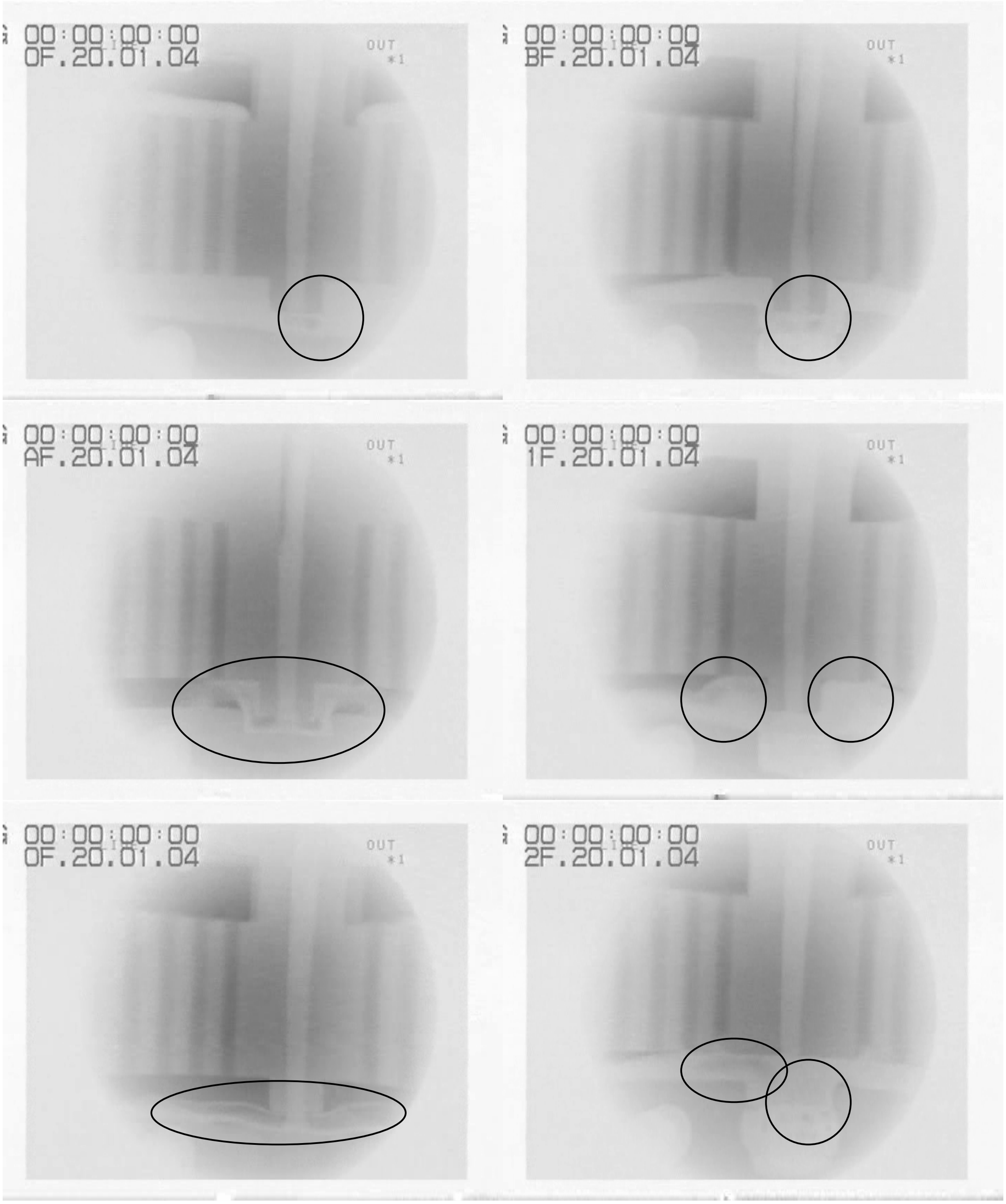

(a)

Figure 3.11: *Real time X-Ray studies with different gating designs; entrapment of bubbles and severe turbulence was observed (dark regions are gaps and white regions are liquid metal in the marked points)*

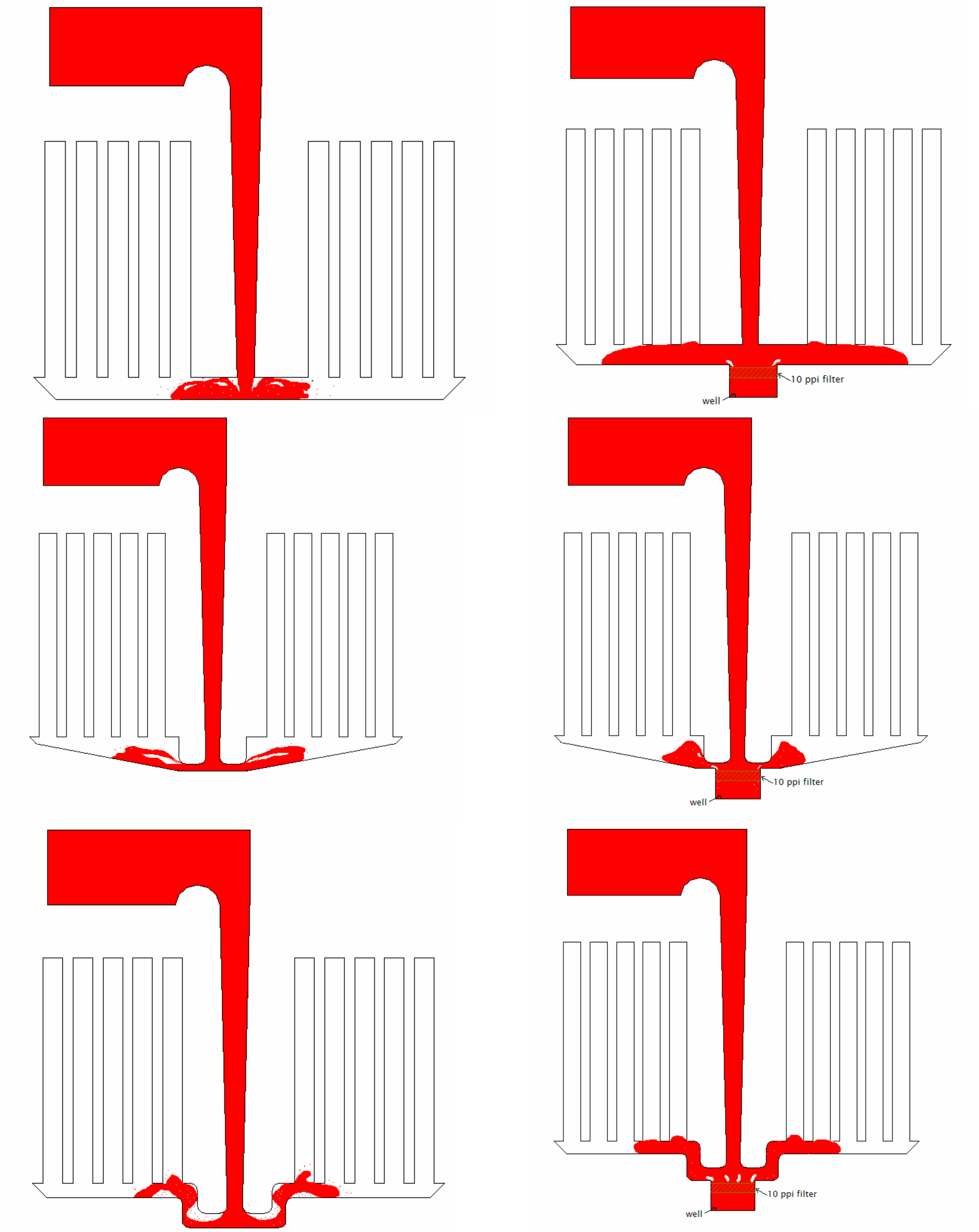

(b)

Figure 3.12: *Schematic illustration of mould fillings taken from real time X-Ray studies(Figure 3.11)*

Left row: Different patterns,

Right Row: same pattern as left row but with filters placed under sprue

(dark regions are liquid metal and white regions are air entrapment and gap)

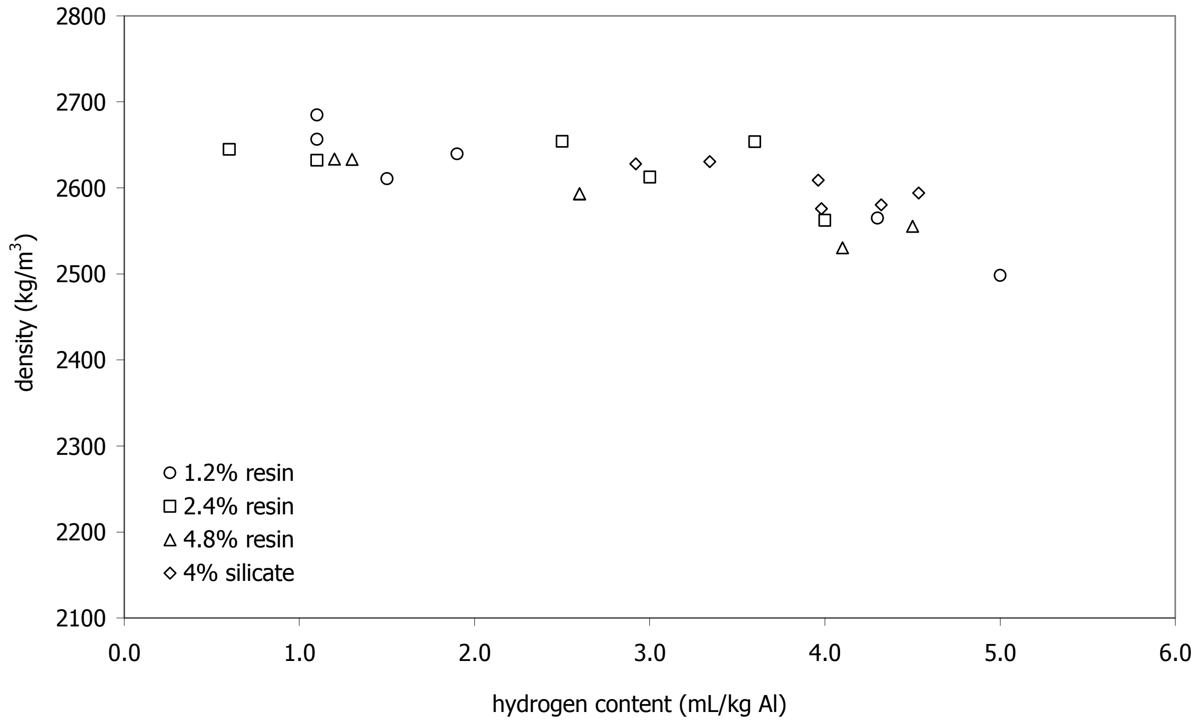

Figure 4.1: *RPT sample density change with hydrogen (solidified at 100 mbar –alloy LM4)*

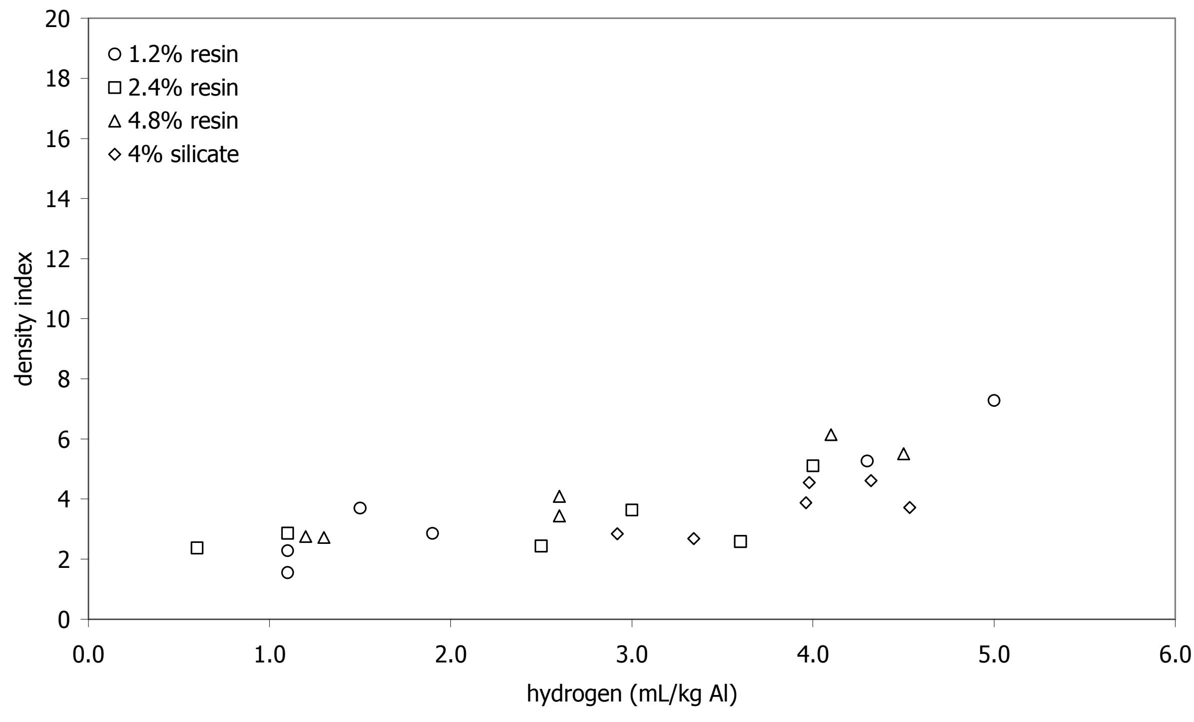

Figure 4.2: *density index change at 100 mbar –alloy LM4*

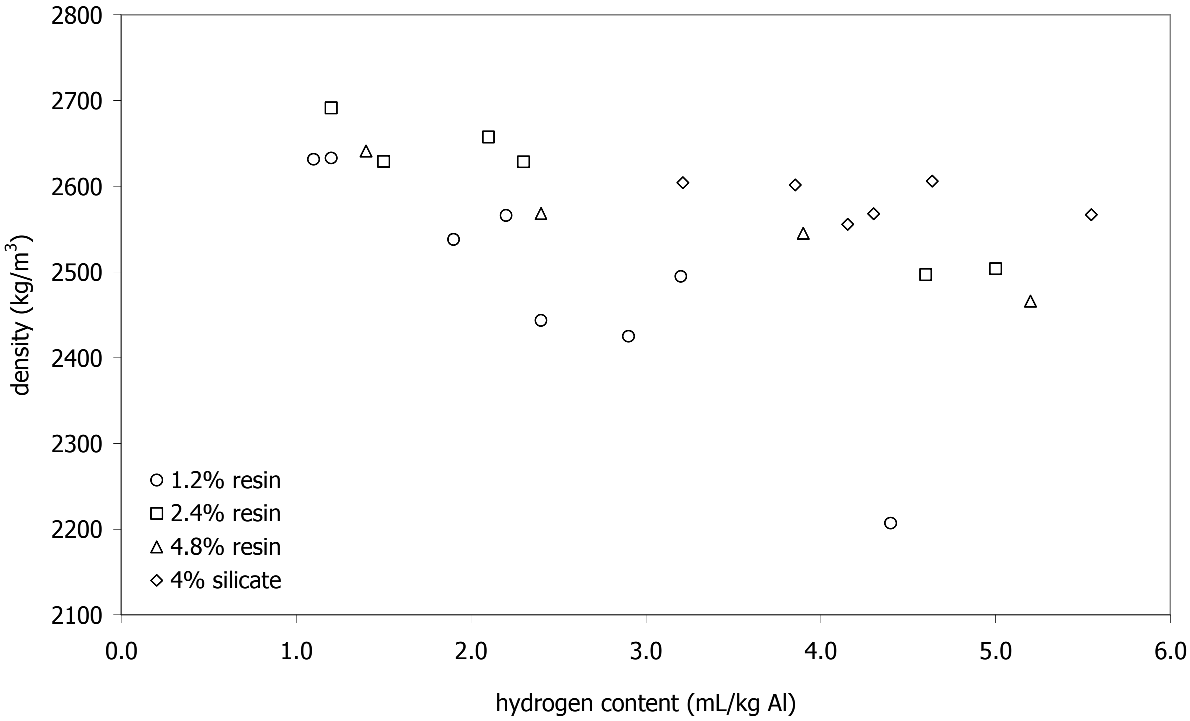

Figure 4.3: *RPT sample density change with hydrogen (solidified at 10 mbar –alloy LM4)*

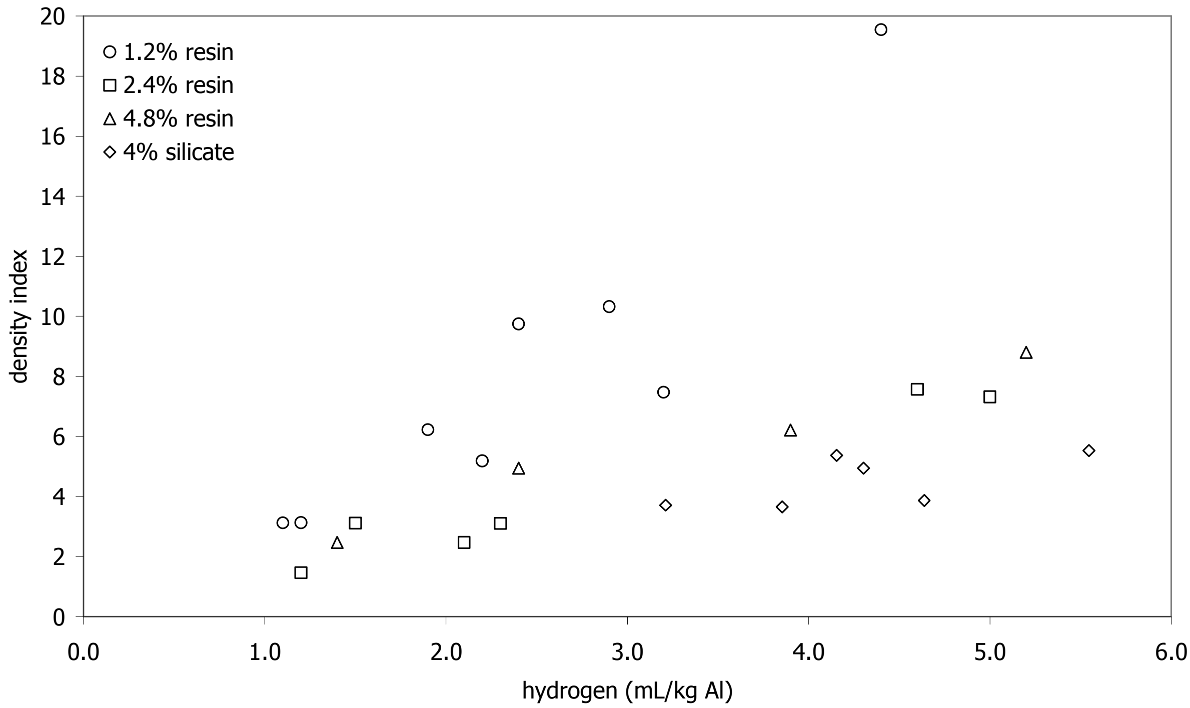

Figure 4.4: *density index change at 10 mbar –alloy LM4*

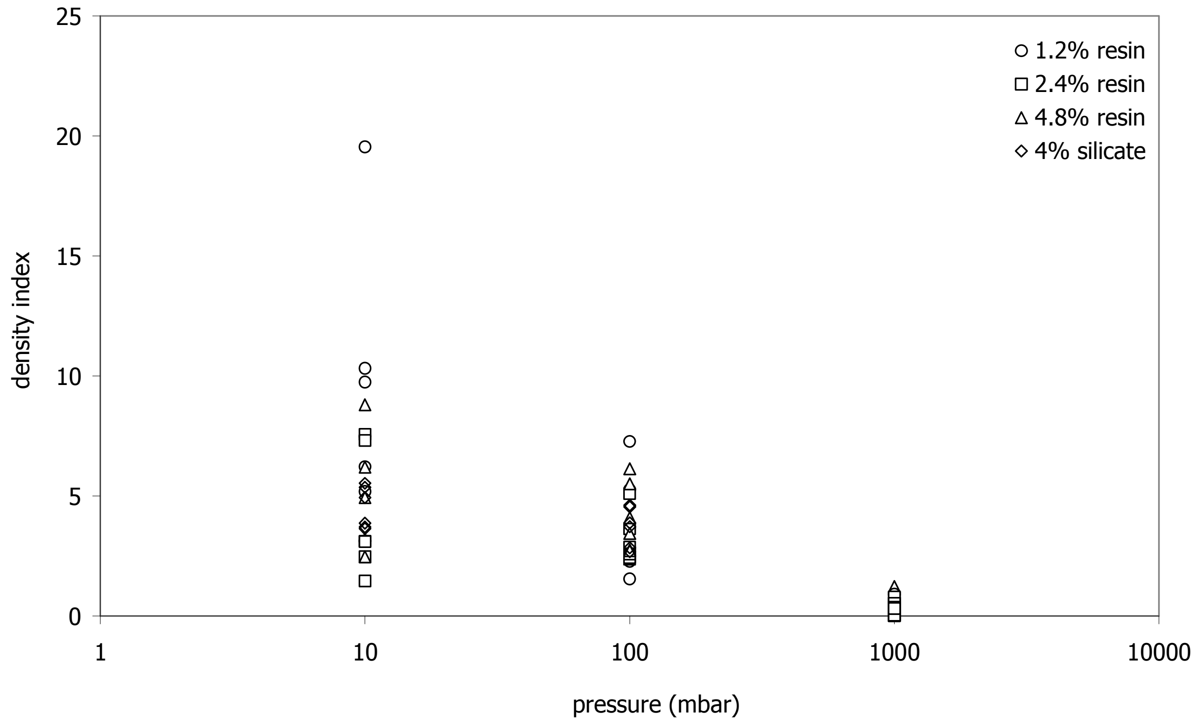

Figure 4.5: *density index variation at different pressures –alloy LM4*

Test Pressure / Binder Content	10 mbar	100 mbar
1.2% resin	 H_2: 2.9 mL/kg	 H_2: 2.2 mL/kg
2.4% resin	 H_2: 4.6 mL/kg	 H_2: 2.3 mL/kg
4.8% resin	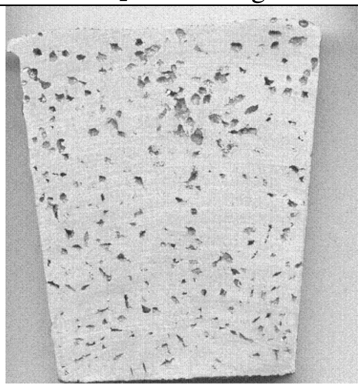 H_2: 3.2 mL/kg	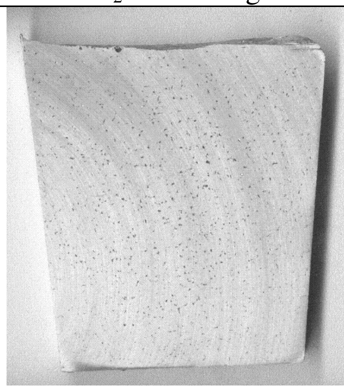 H_2: 2.4 mL/kg
4% $NaSiO_3$	 H_2: 4.2 mL/kg	 H_2: 2.0 mL/kg

Figure 4.6: *Sectioned surface of the reduced pressure test samples cast at moulds with different binder contents (alloy LM4)*

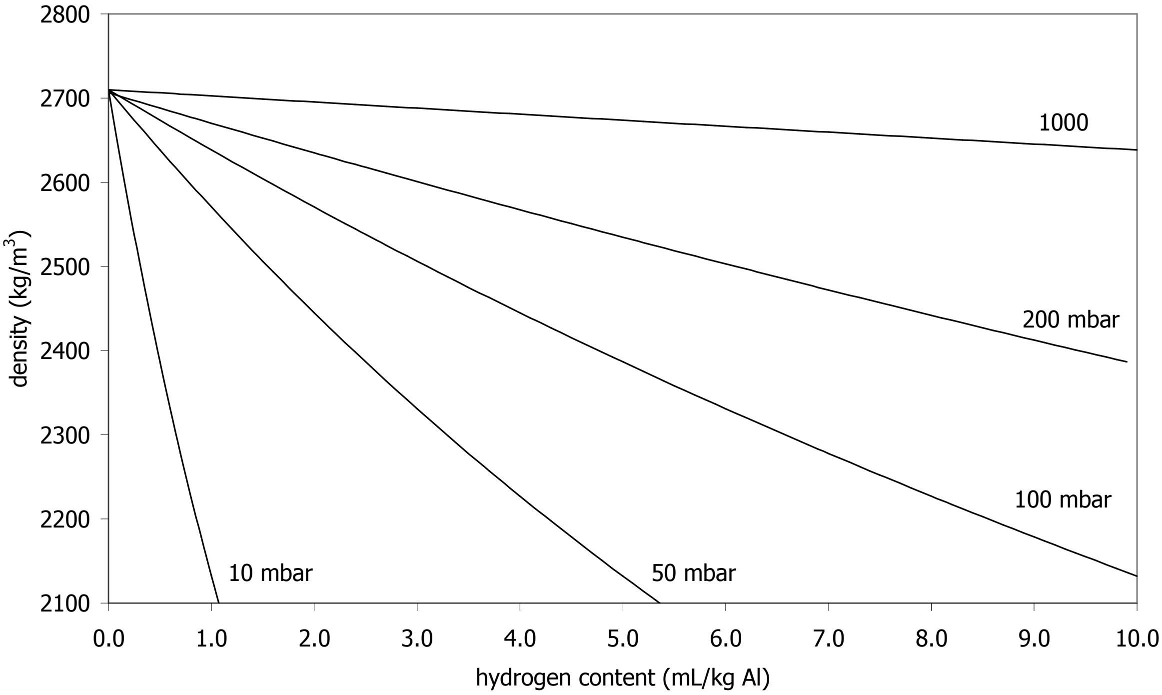

Figure 4.7: *theoretical density-hydrogen relationship at different vacuum levels*

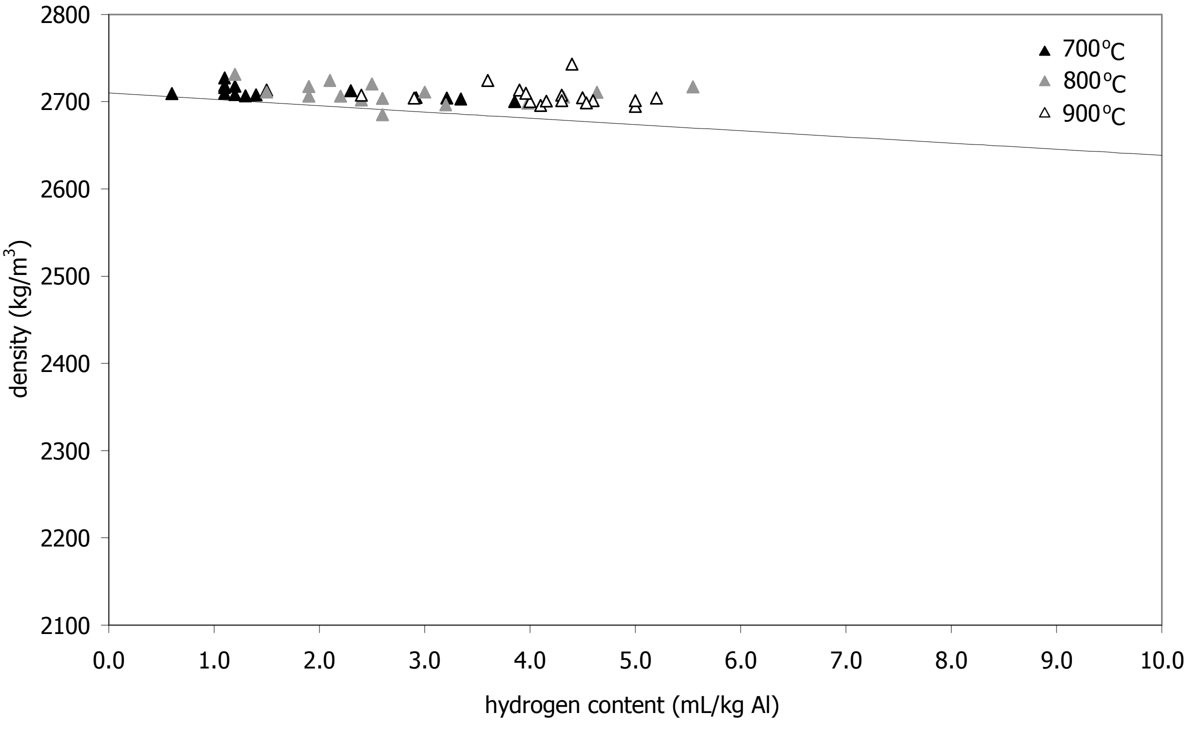

(a) 1000 mbar

(the line represents the theoretical relationship from Figure 4.7)

Figure 4.8: *comparison of theoretical relationship of density change with hydrogen from RPT samples obtained at different vacuum levels –alloy LM4*
(a)1000 mbar

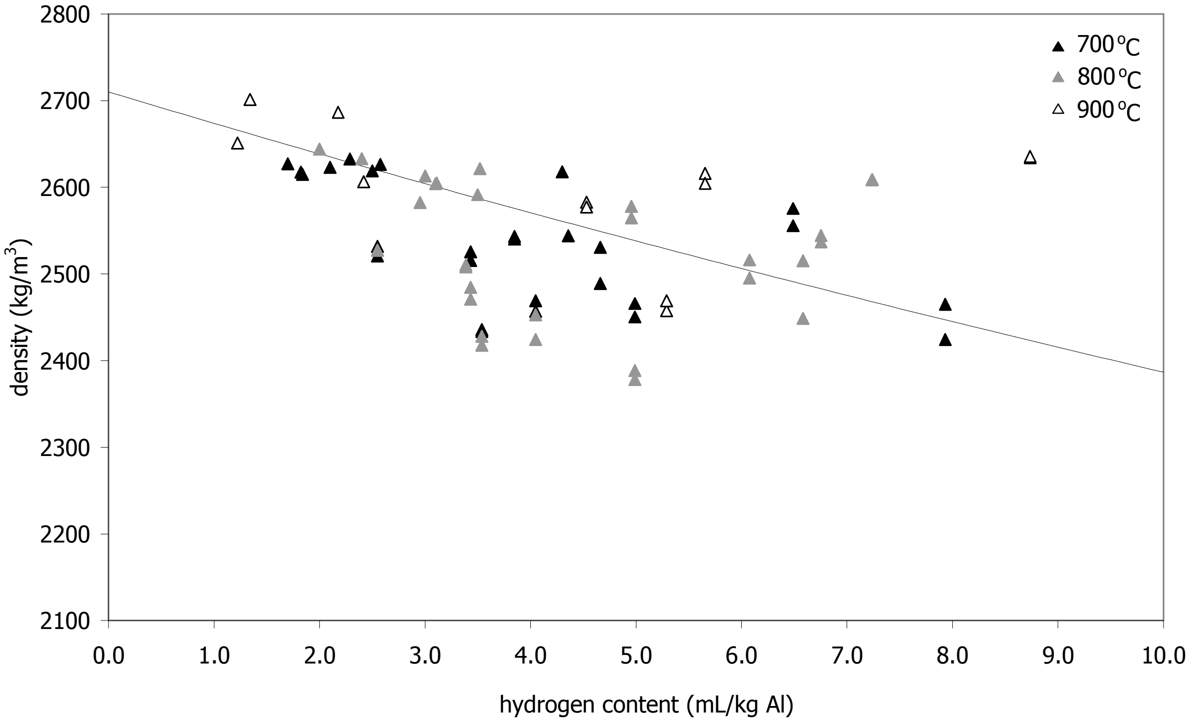

(b) 200 mbar

(the line represents the theoretical relationship from Figure 4.7)

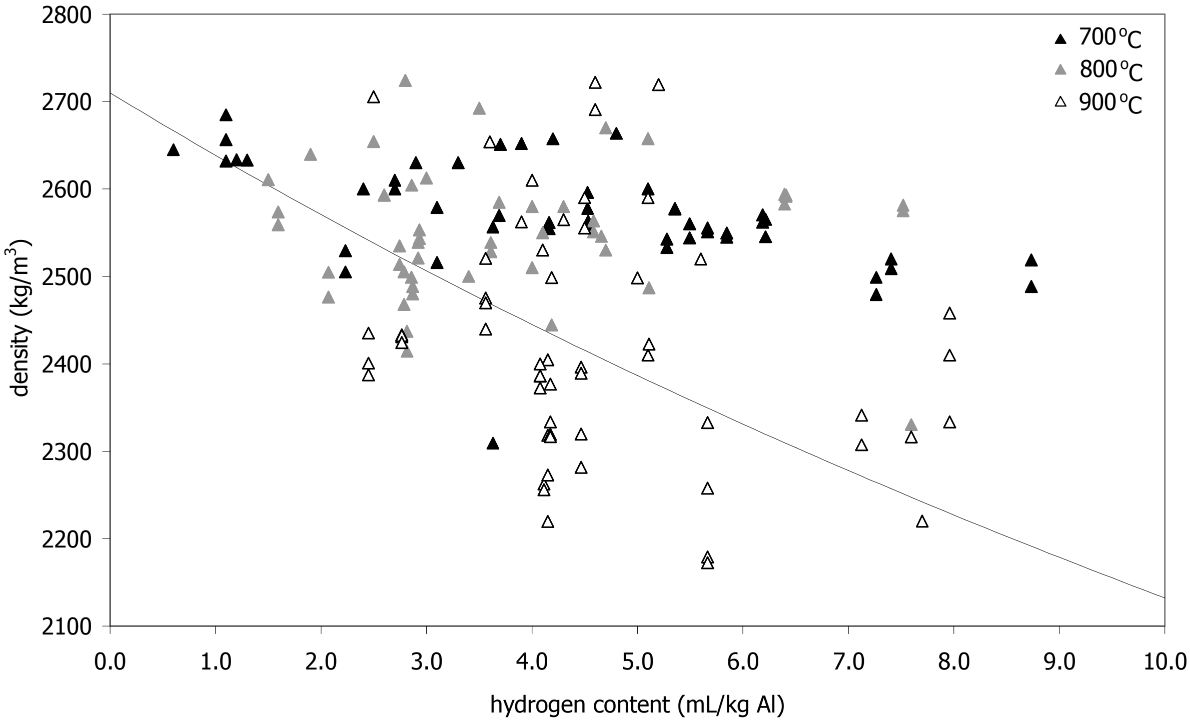

(c) 100 mbar

(the line represents the theoretical relationship from Figure 4.7)

Figure 4.8: *comparison of theoretical relationship of density change with hydrogen from RPT samples obtained at different vacuum levels –alloy LM4 (continued) (b) 200 mbar, (c) 100 mbar*

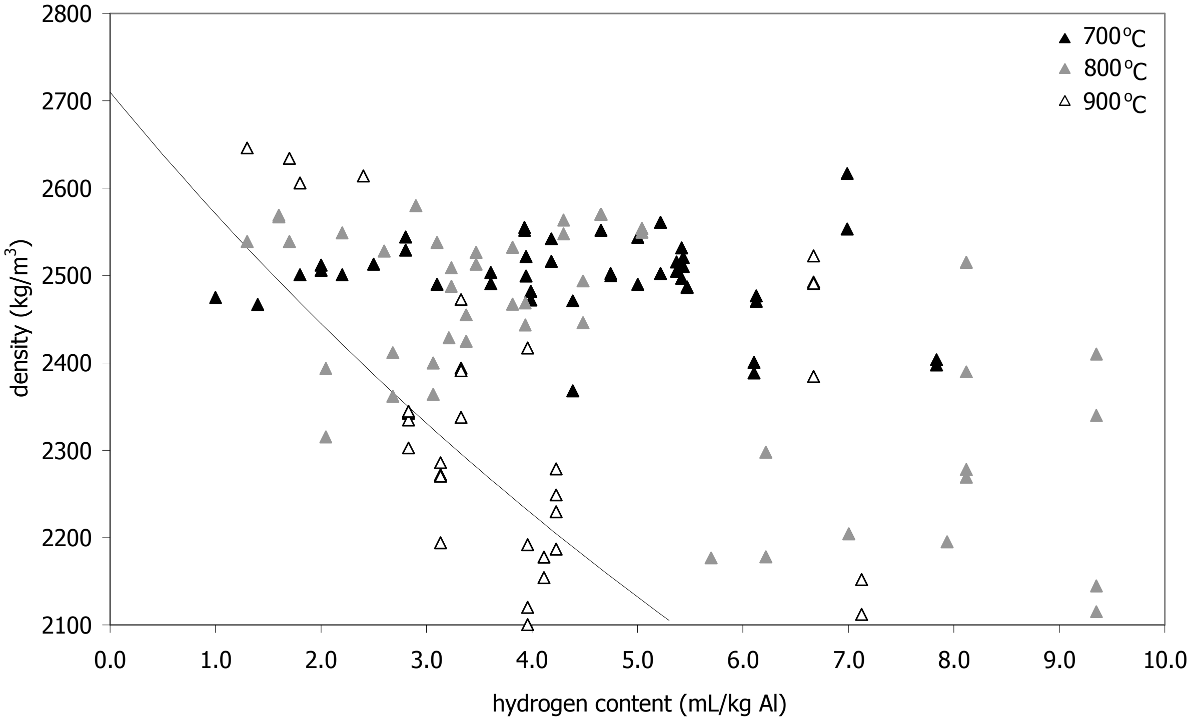

(d) 50 mbar

(the line represents the theoretical relationship from Figure 4.7)

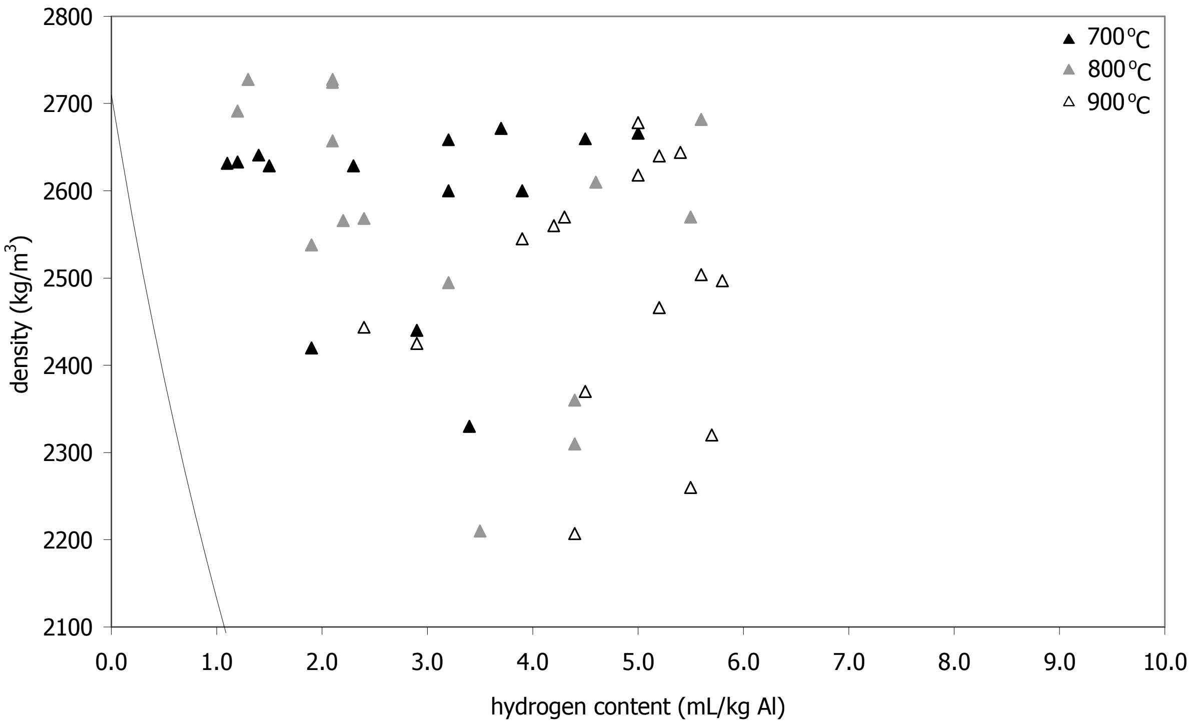

(e) 10 mbar

(the line represents the theoretical relationship from Figure 4.7)

Figure 4.8: *comparison of theoretical relationship of density change with hydrogen from RPT samples obtained at different vacuum levels –alloy LM4 (continued) (d) 50 mbar, (e) 10 mbar*

temperature / *pressure*	*700°C*	*800°C*	*900°C*
1000 mbar	 d=2727 kg/m^3 d_{index}=0.00% H=1.1 mL/kg	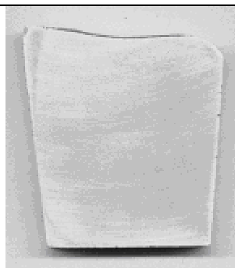 d=2725 kg/m^3 d_{index}=0.00% H=2.1 mL/kg	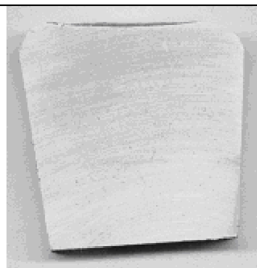 d=2731 kg/m^3 d_{index}=0.00% H=3.6 mL/kg
200 mbar	 density = 2616 kg/m^3 d_{index}=3.51% H_2= 1.8 mL/kg	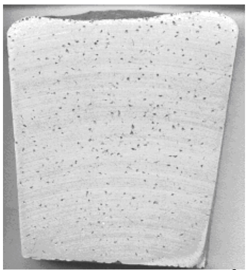 density = 2621 kg/m^3 d_{index}= 3.27% H_2 = 3.5 m/kg	 density = 2686 kg/m^3 d_{index}= 0.86% H_2= 2.2 mL/kg
100 mbar	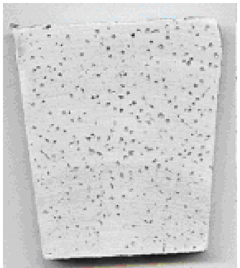 d=2530 kg/m^3 d_{index}=6.14% H_2 content=4.1 mL/kg	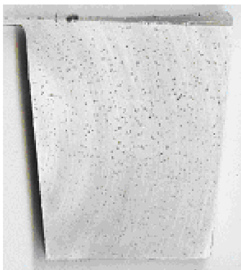 d=2593 kg/m^3 d_{index}=4.09% H_2 content=2.6 mL/kg	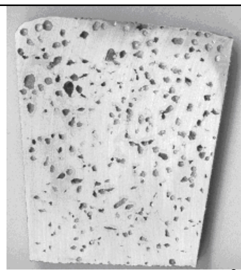 density = 2409 kg/m^3 d_{index}= 11.08 % H_2= 5.1 mL/kg
50 mbar	 density = 2513 kg/m^3 d_{index}= 7.25% H_2 = 3.0 mL/kg	 density = 2539 kg/m^3 d_{index}= 6.31% H_2= 1.3 mL/kg	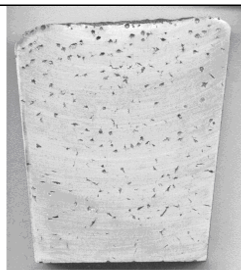 density = 2606 kg/m^3 d_{index}= 3.83 % H_2= 1.8 mL/kg
10 mbar	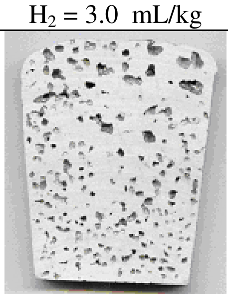 d=2207 kg/m^3 d_{index}=19.5% H_2 content=4.4 mL/kg	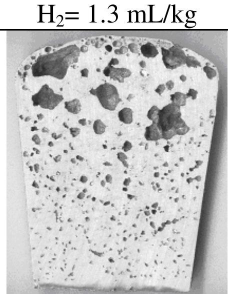 density=2205 kg/m^3 d_{index}=18.6% H_2=3.5 m/kg	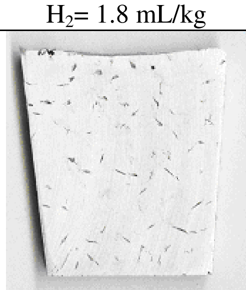 d=2640 kg/m^3 d_{index}=2.58% H_2 content=3.9 mL/kg

10 mm

Figure 4.9: *different morphology and size of pores in RPT sample at different vacuum levels and casting temperatures*

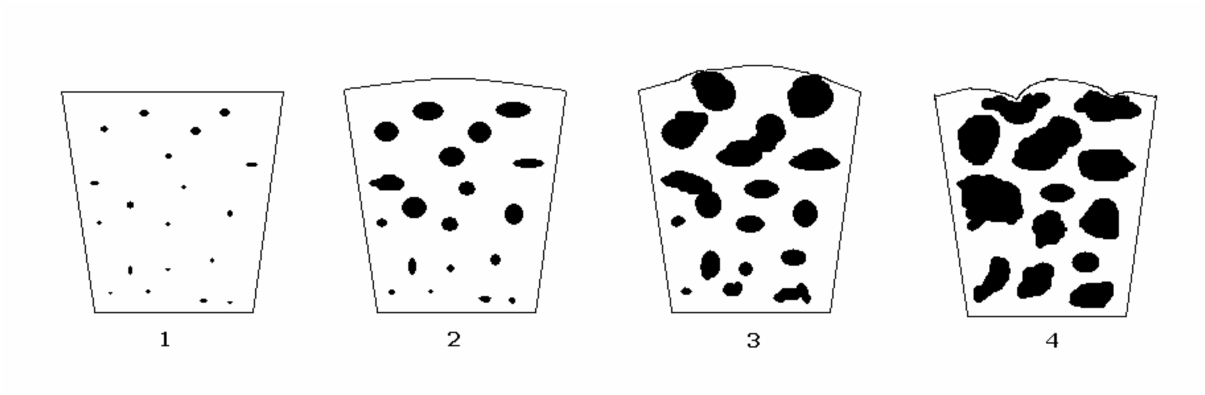

Figure 4.10: *schematic bursting of bubbles from the surface*

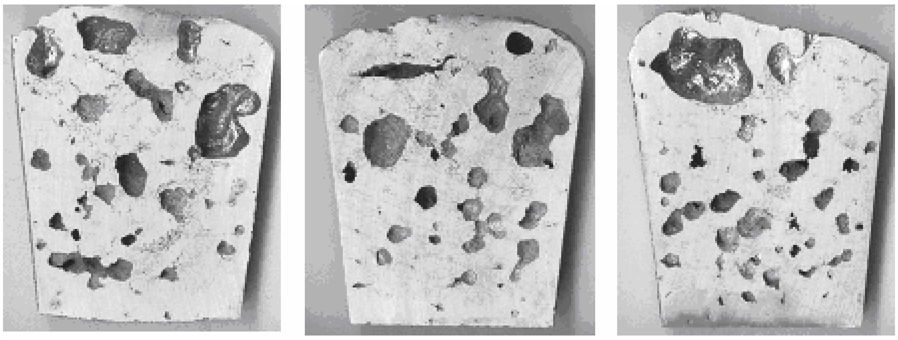

Figure 4.11: *Examples of bursting shown from sectioned surfaces of the reduced pressure test samples at 10 mbar*

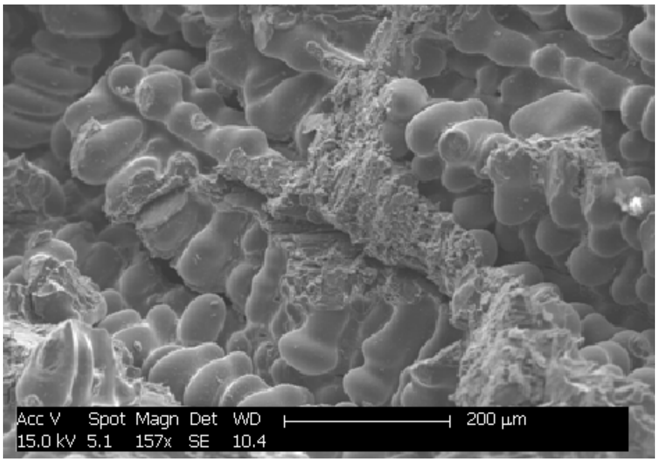

(a)

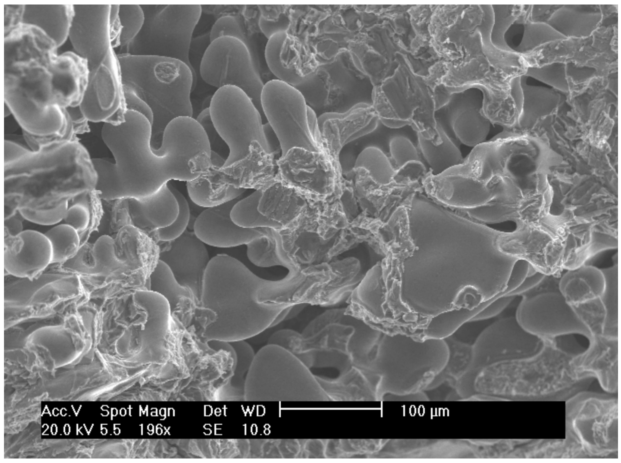

(b)

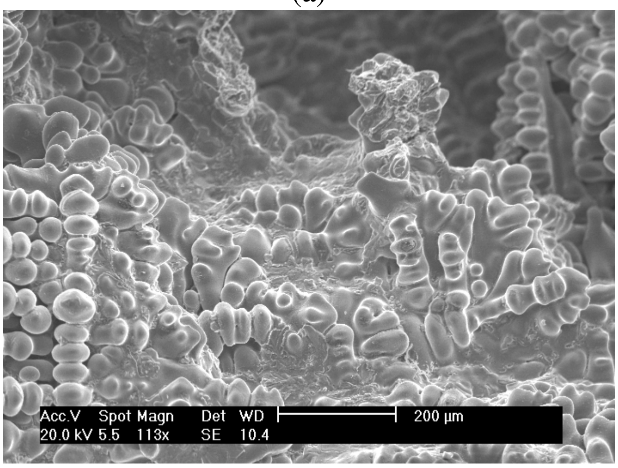

(c)

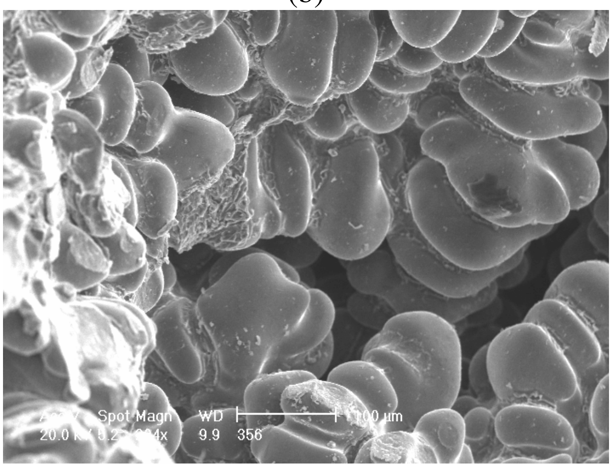

(d)

Figure 4.12: *SEM images of inside the pores of RPT samples (LM4)*

(dendrites are smooth and oxides are roughened areas) (cont…)

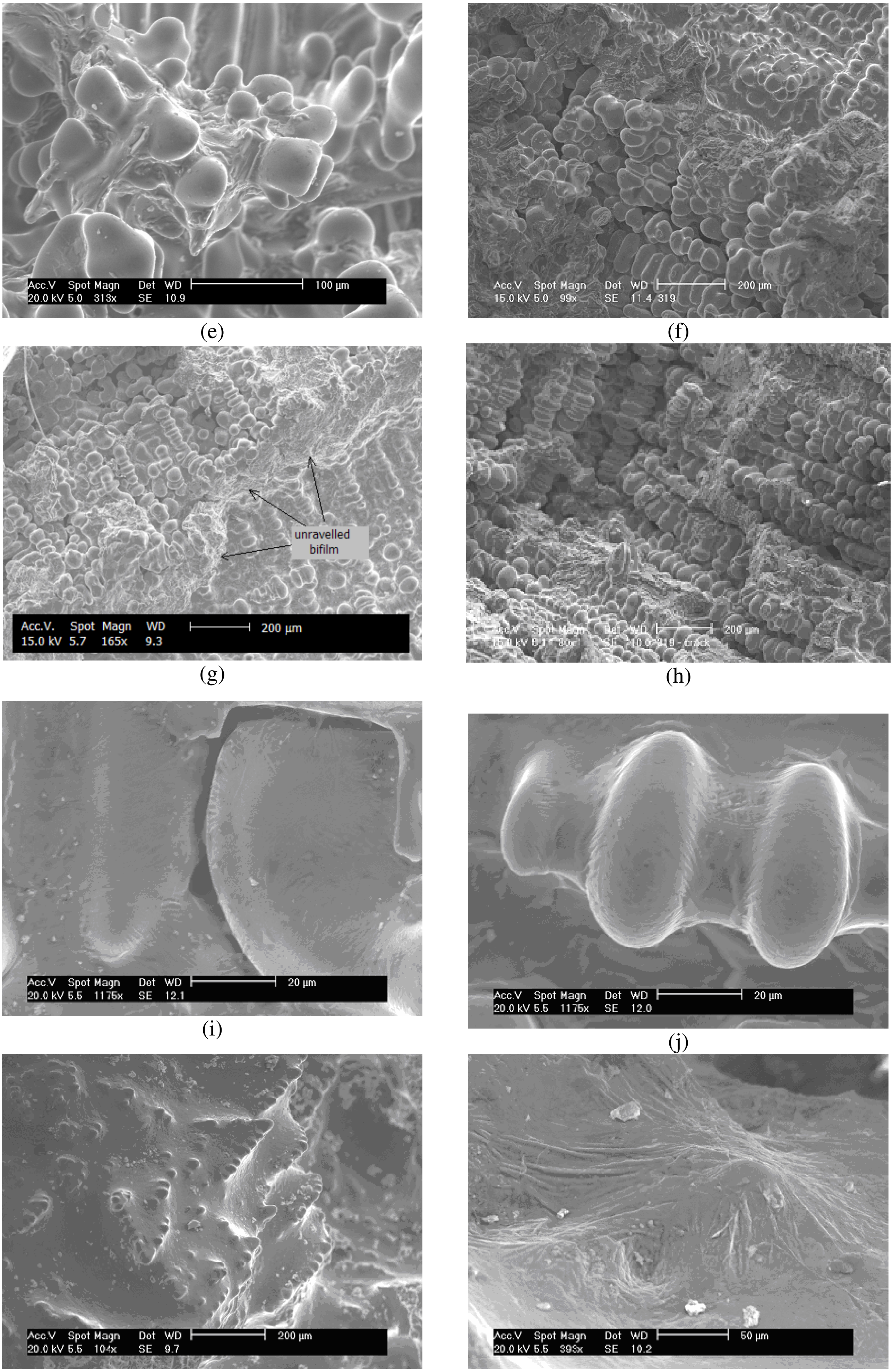

Figure 4.12: *SEM images of inside the pores of RPT samples (LM4)*

(dendrites are smooth and oxides are roughened areas)

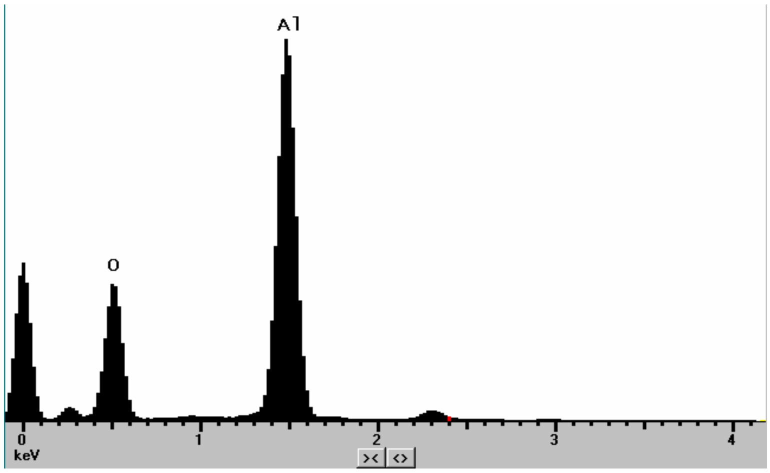

(a)

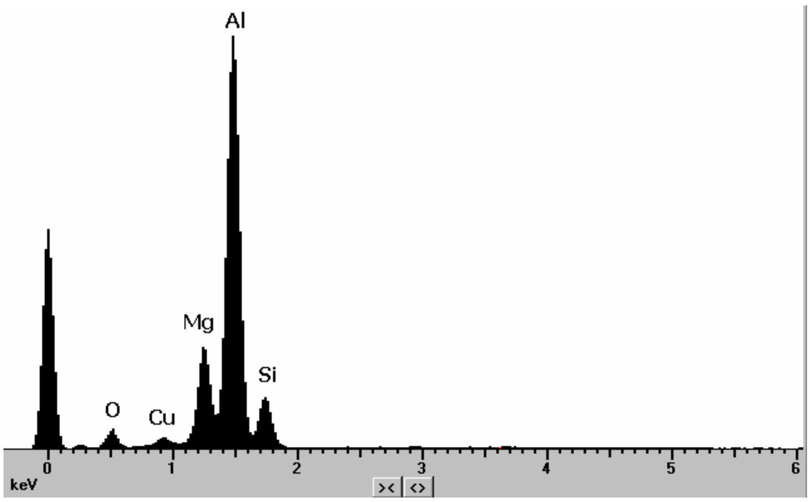

(b)

Figure 4.13: *EDS analysis of roughened areas shown in Figure 4.12*

(a) Some thick oxides gave only Al and O peaks

(b) In some cases Mg, Si and Cu phases under the thin oxide were detected

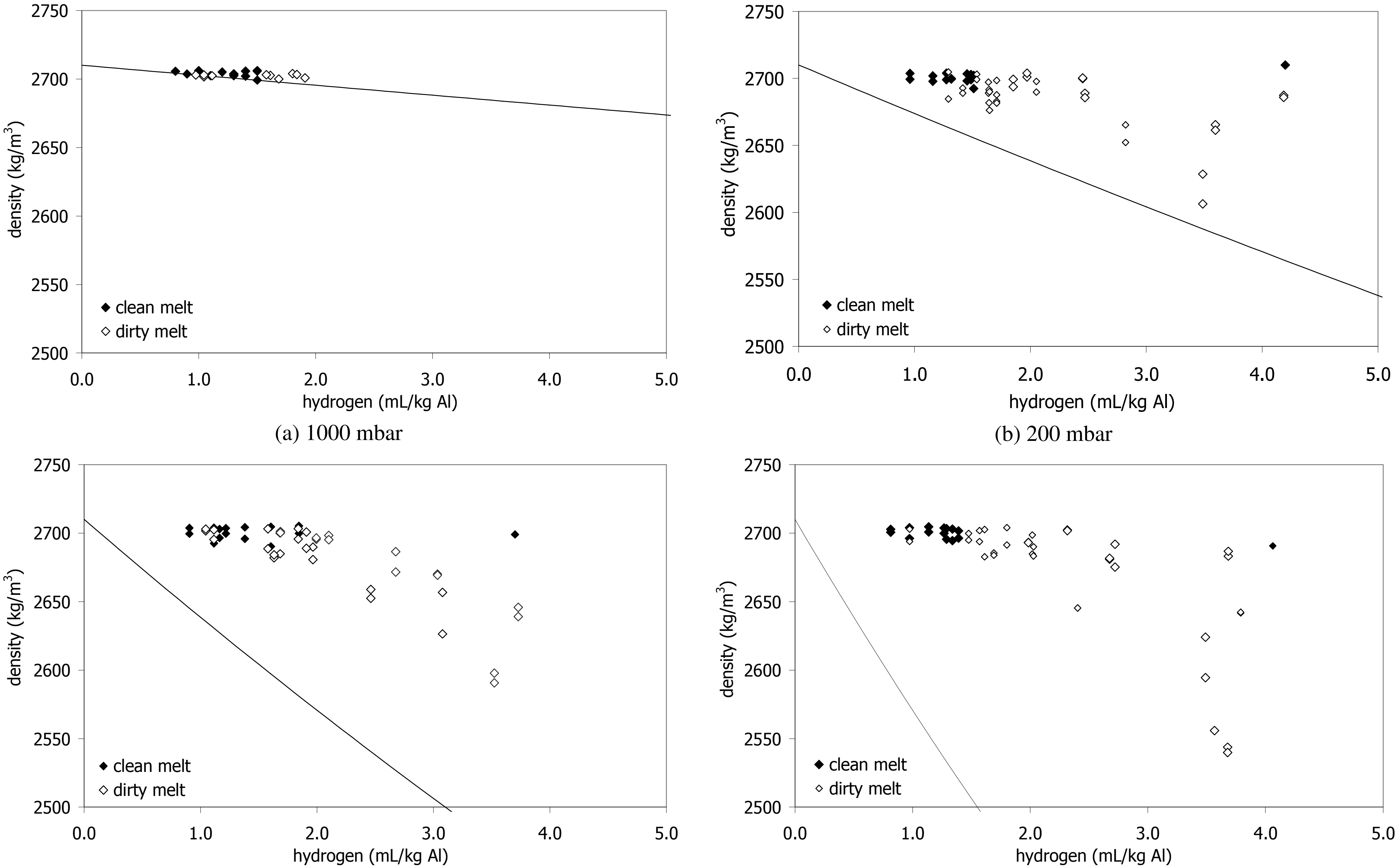

(a) 1000 mbar
(b) 200 mbar
(c) 100 mbar
(d) 50 mbar

Figure 4.14: *density-hydrogen relationship at different vacuum levels; LM0 melt at 750°C*

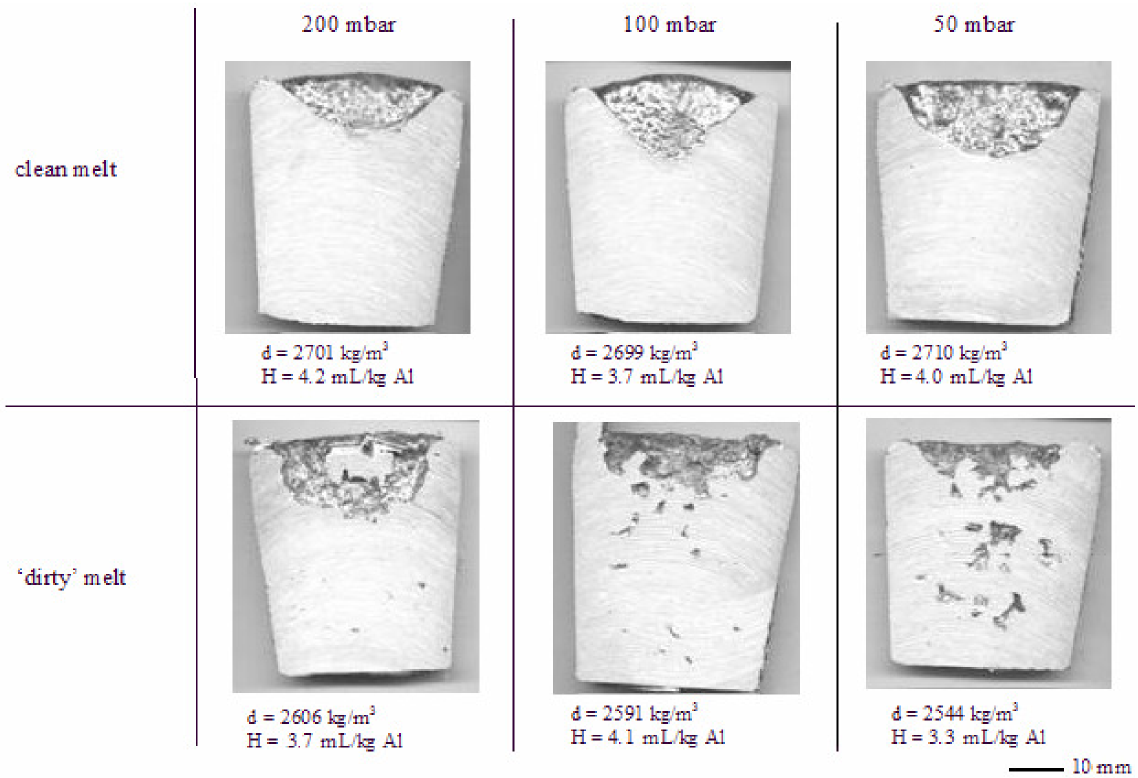

Figure 4.15: *Sectioned surfaces of 99% Al (LM0) samples cast at 750°C: clean and unclean melts (200 mbar, 100 mbar, 50 mbar)*

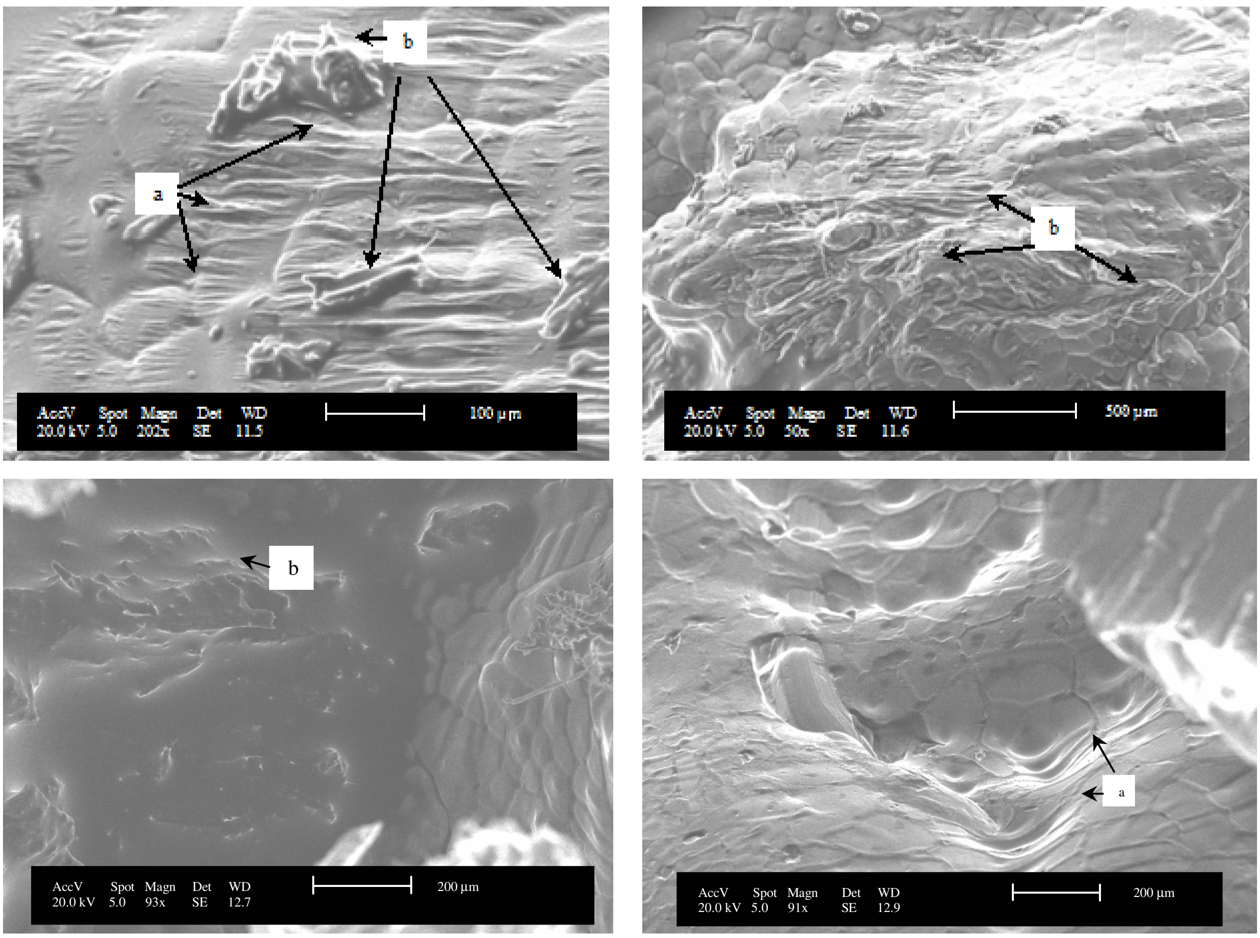

Figure 4.16: *SEM pictures of LM0: oxide covered surfaces inside the pores (a) young oxides, (b) old oxides*

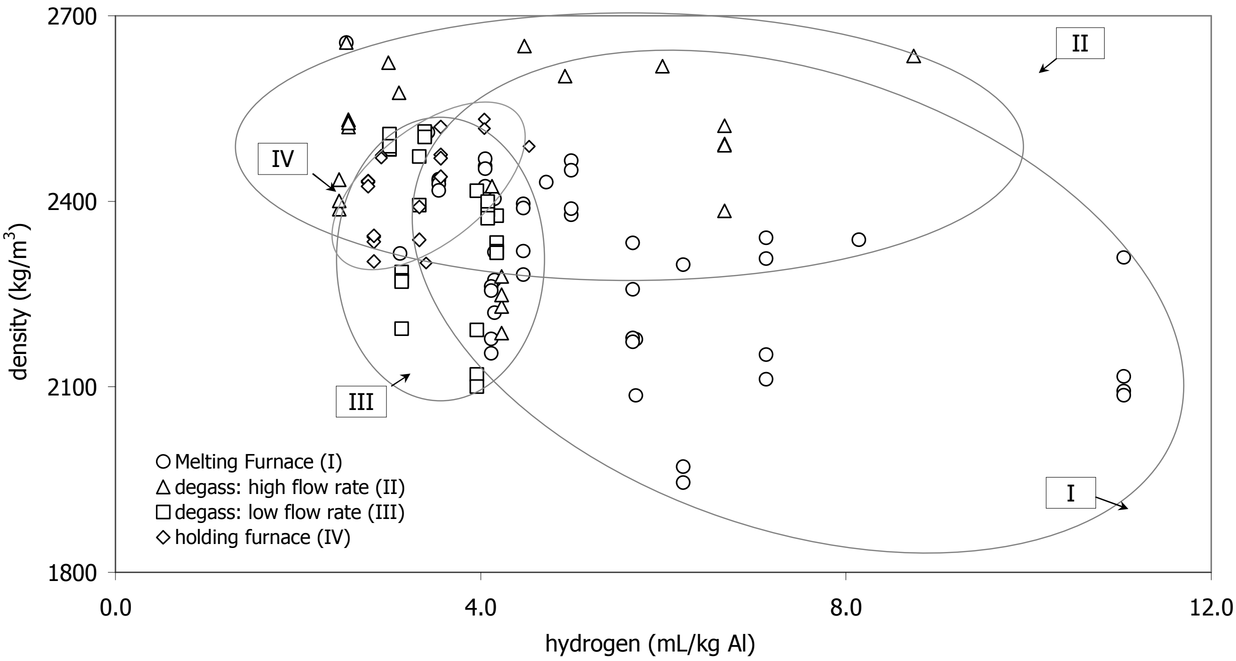

Figure 4.17: *Alloy LM27: degassing studies with high gas flow rate and low gas flow rate (50 and 100 mbar)*

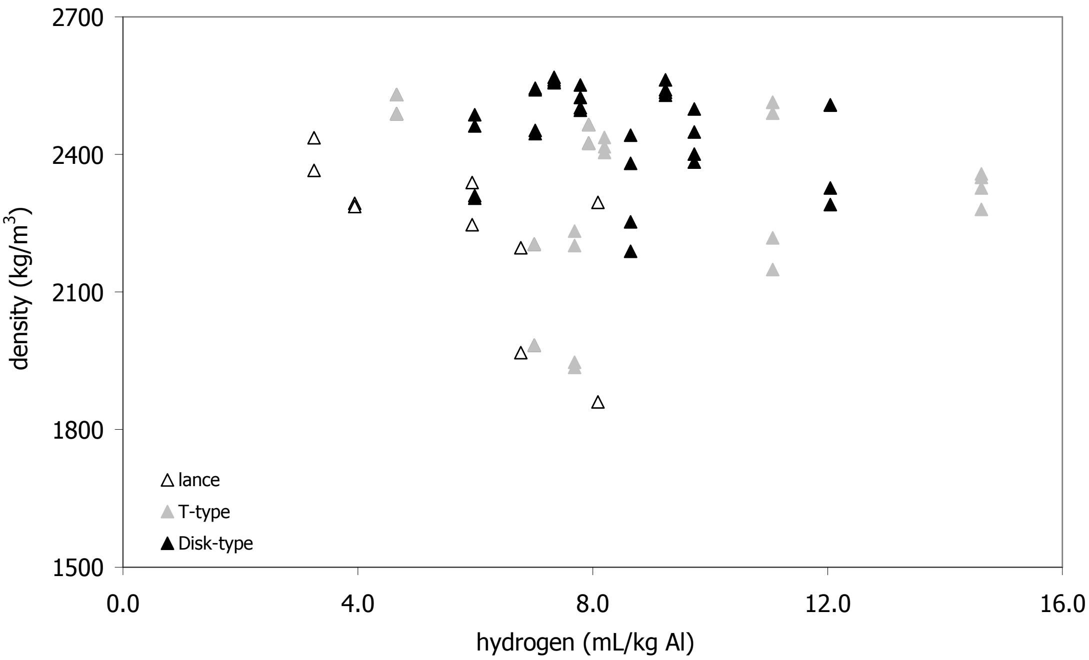

Figure 4.18: *fluxing and degassing with different diffusors (alloy LM4 - 50 and 100 mbar)*

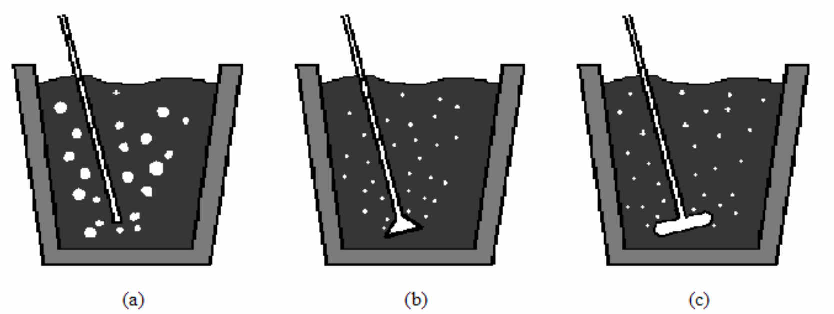

Figure 4.19: *The predicted bubble distribution with different diffusors*
a) lance: coarse and few bubbles,
b) disc type ceramic: finer and more bubbles,
c) T-type ceramic: finer and evenly distributed

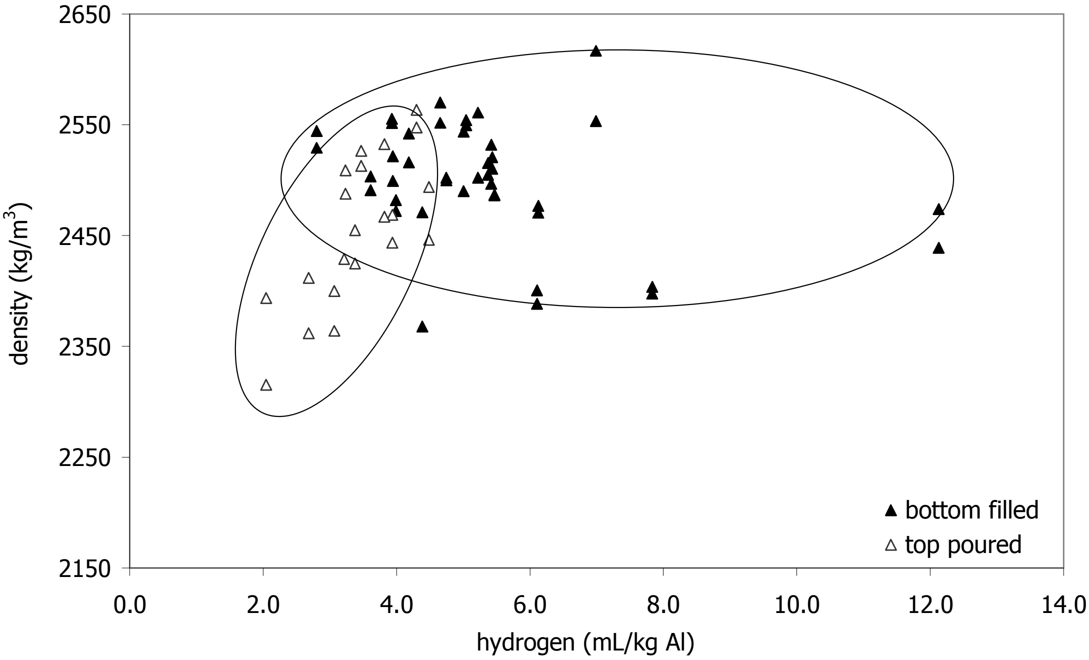

(a)

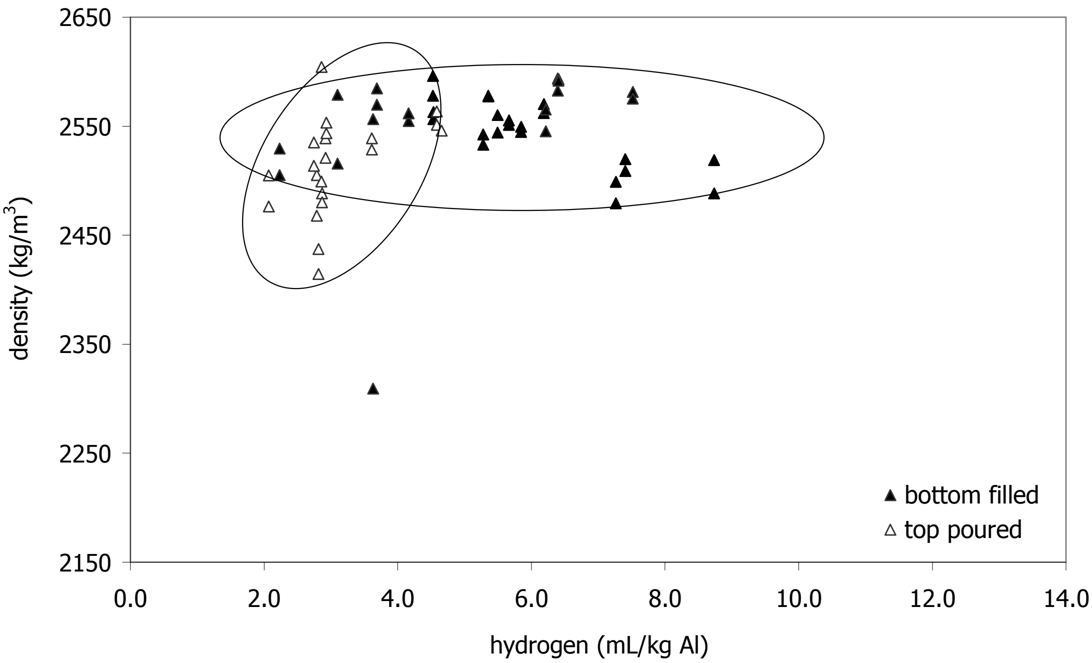

(b)

Figure 4.20: *density-hydrogen relationship at different casting levels (LM24); a) 50 mbar, b) 100 mbar*

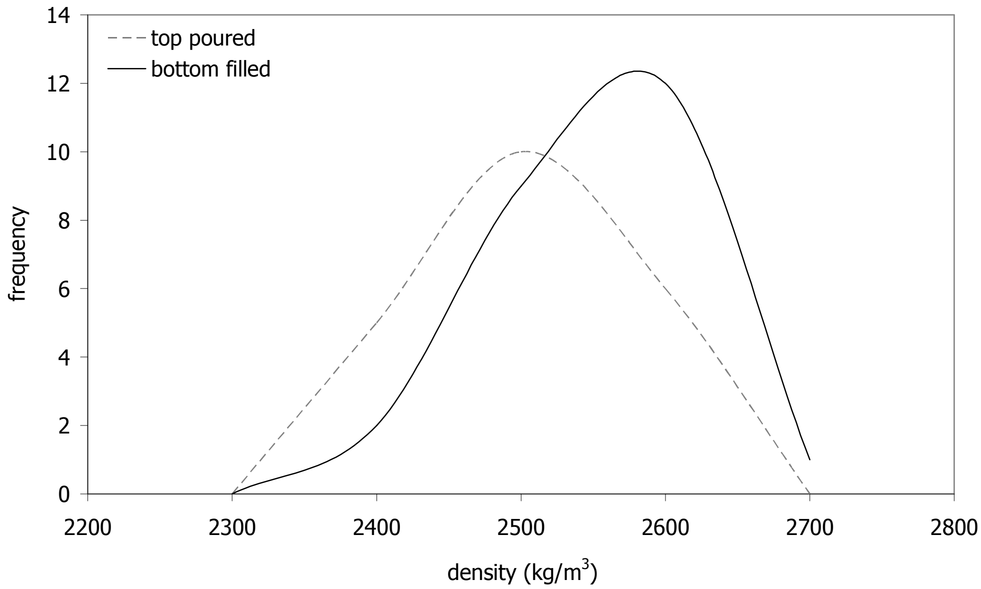

(a)

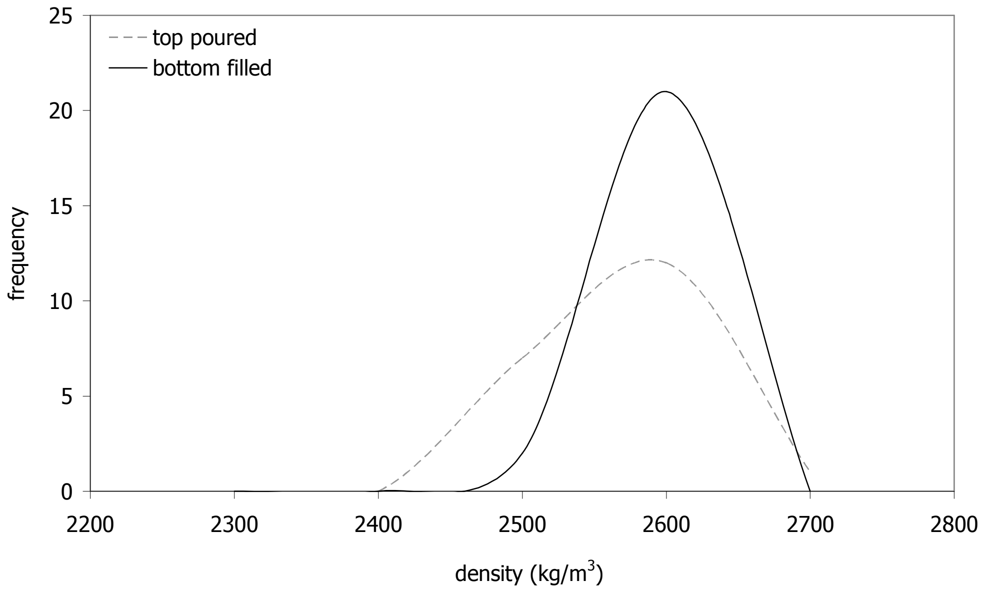

(b)

Figure 4.21: *histogram of density of the RPT samples (LM24)*

(a) 50 mbar, (b) 100 mbar

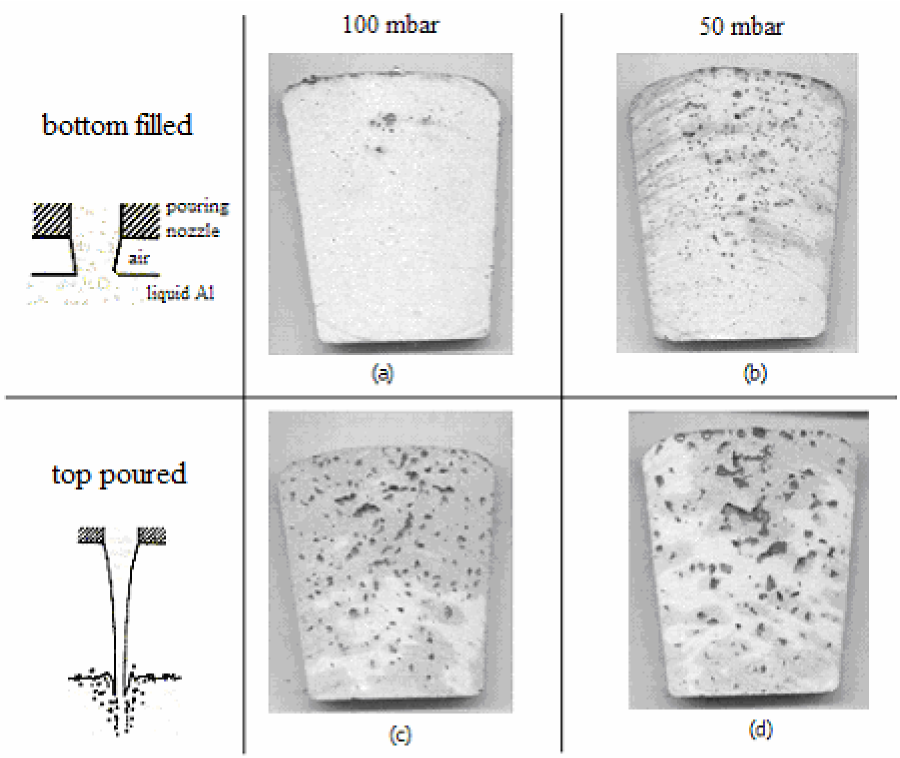

Figure 4.22: *the effect of casting height and bifilms on the pore morphology (LM24)*

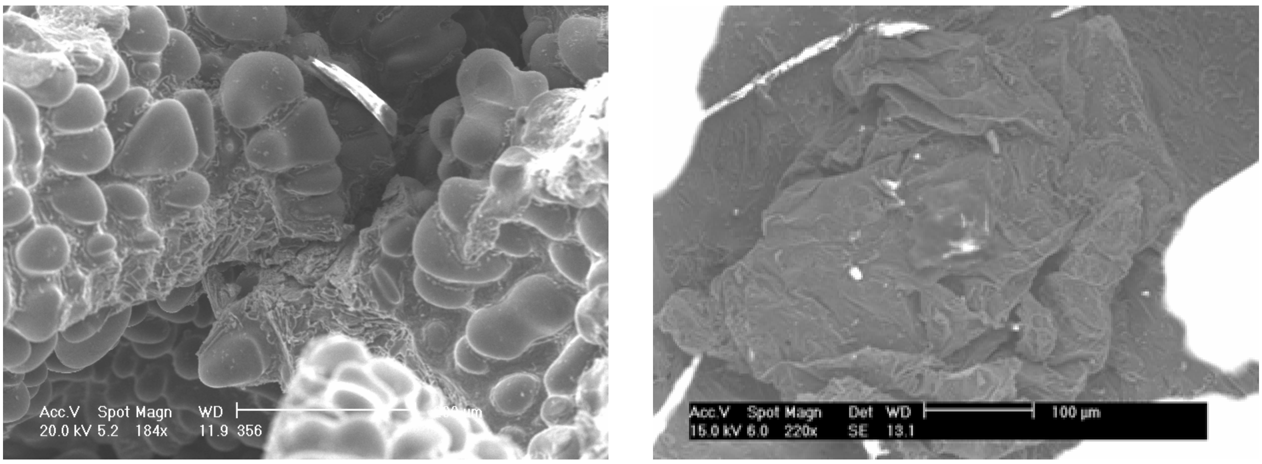

(a) *(b)*

Figure 4.23: *SEM images inside the pore (LM24):*
a) bottom filled: fragments of a bifilm in between dendrites,
b) top poured: close up of an internal crumpled oxide

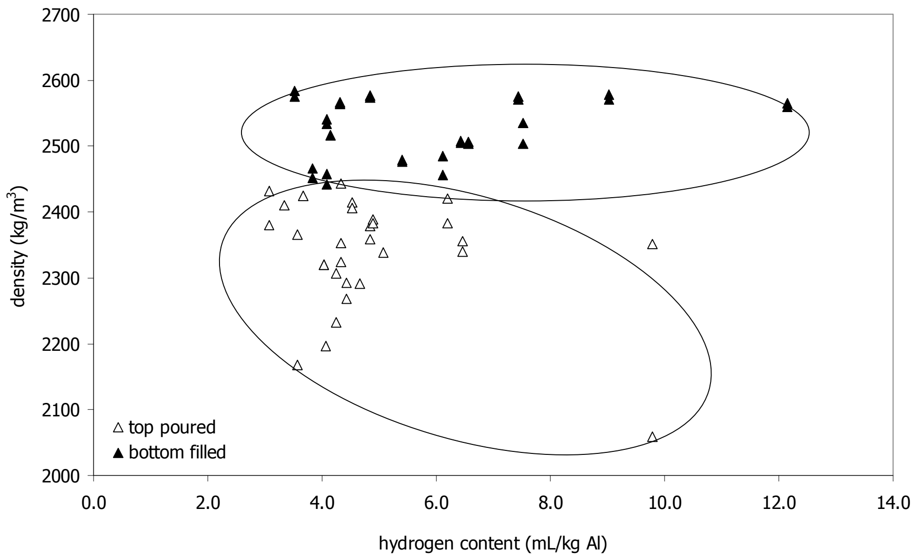

Figure 4.24: *The density change of the reduced pressure test samples cast at different heights (alloy LM25 – 100 mbar)*

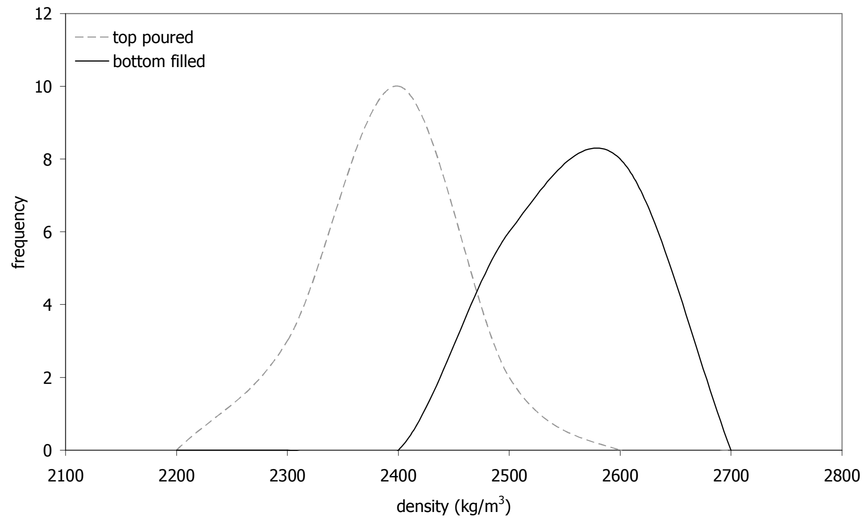

Figure 4.25: *The density histogram of the reduced pressure test samples cast at different heights (alloy LM25)*

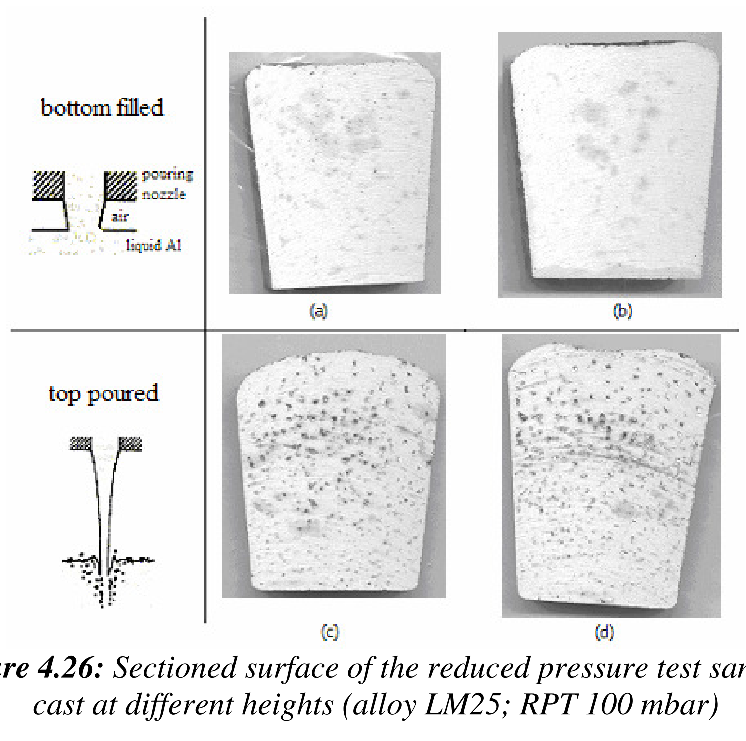

Figure 4.26: *Sectioned surface of the reduced pressure test samples cast at different heights (alloy LM25; RPT 100 mbar)*

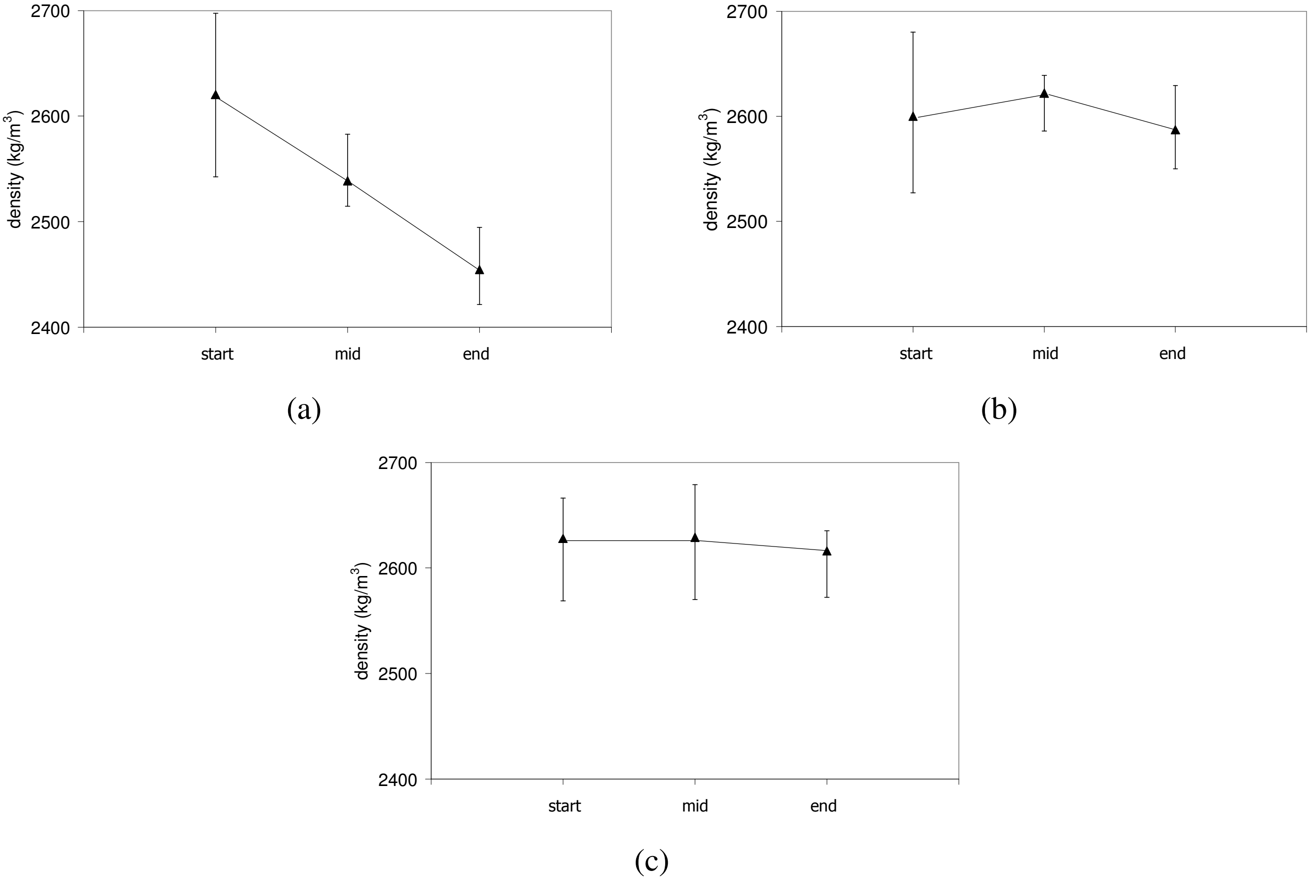

Figure 4.27:*Density change of RPT samples (100 mbar) from start, mid to end when running: (a) 0 diffuser, (b) 1 diffuser, (c) 2 diffusers*

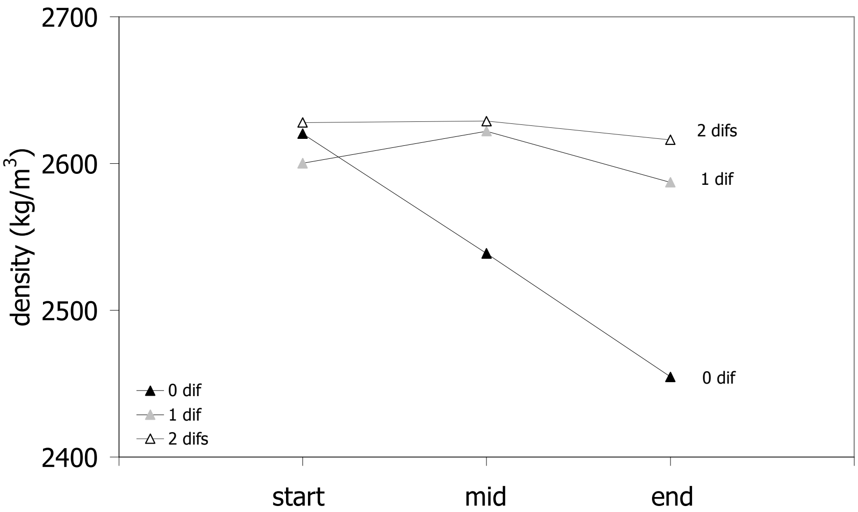

Figure 4.28: *Density of RPT samples comparing different number of diffusers (100 mbar)*

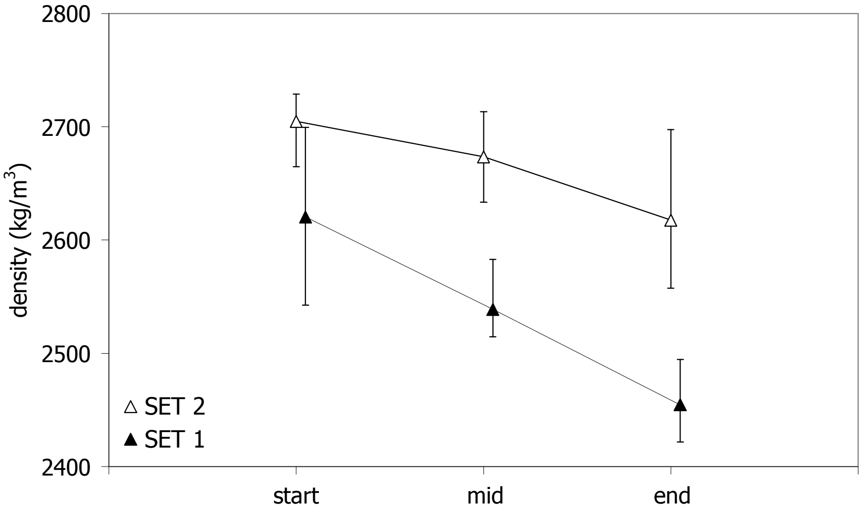

(a)

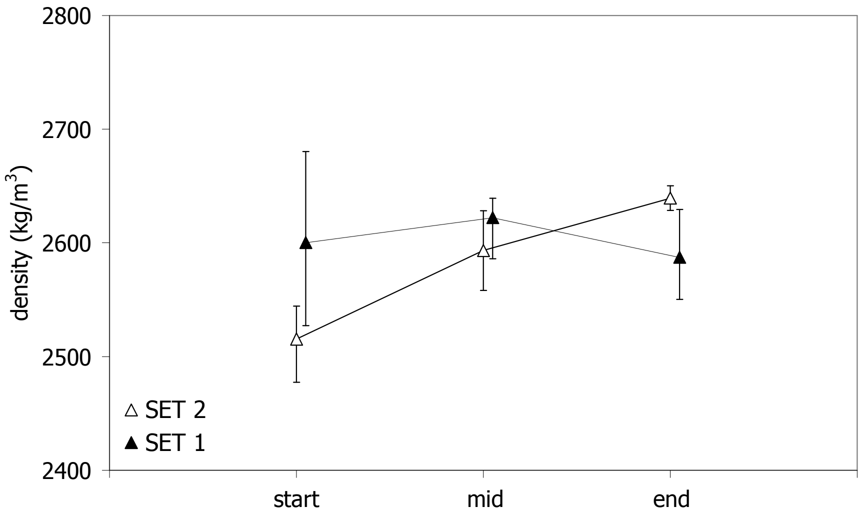

(b)

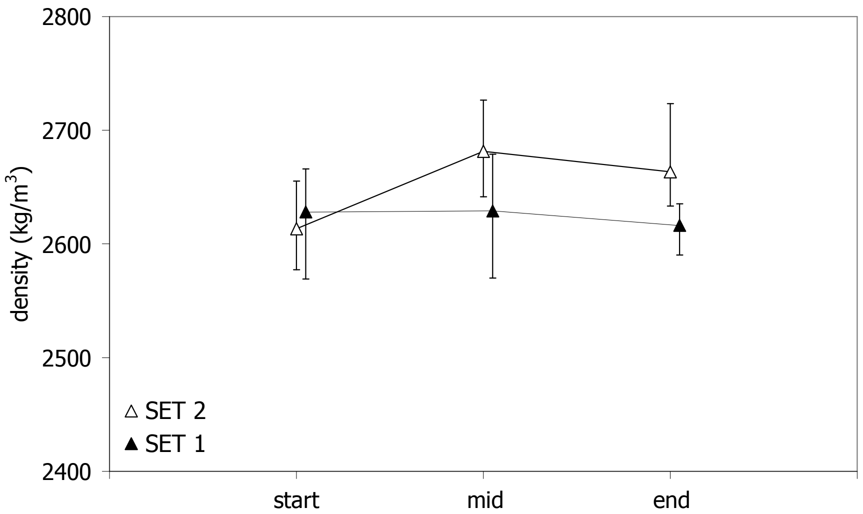

(c)

Figure 4.29: *The density of RPT samples comparing the different techniques (100 mbar)*
(a) 0 diffuser, (b) 1 diffuser, (c) 2 diffusers
(SET 1: non-quiescent conditions, SET 2: quiescent conditions)

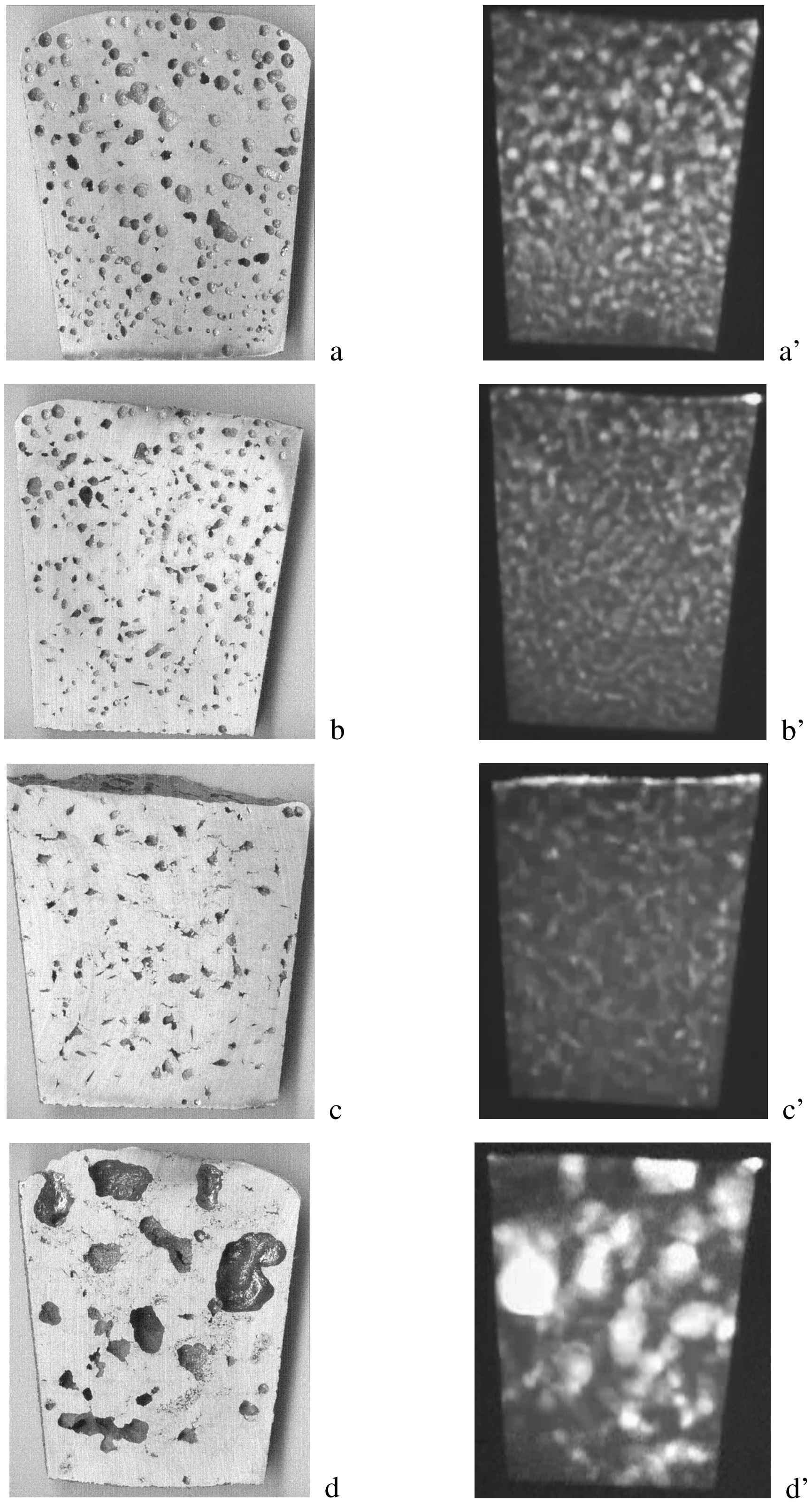

Figure 4.30: *X-RAY images of some of RPT samples*
conditions: a, b, c and d: digitalised image of sectioned surface of RPT samples
a’, b’, c’ and d’: X-Ray images of the same samples before they were sectioned

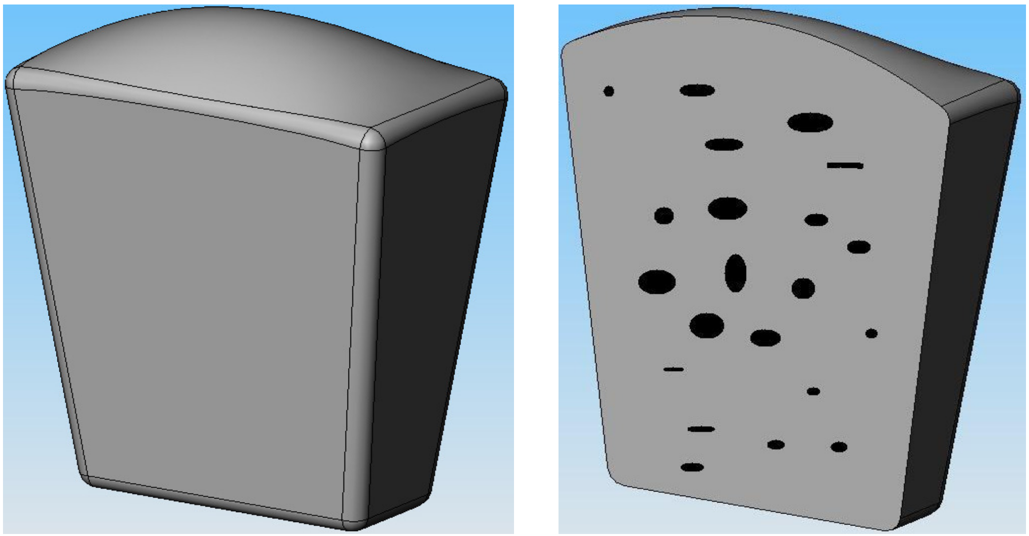

Figure 4.31: *Schematic illustration of sectioning of RPT samples*

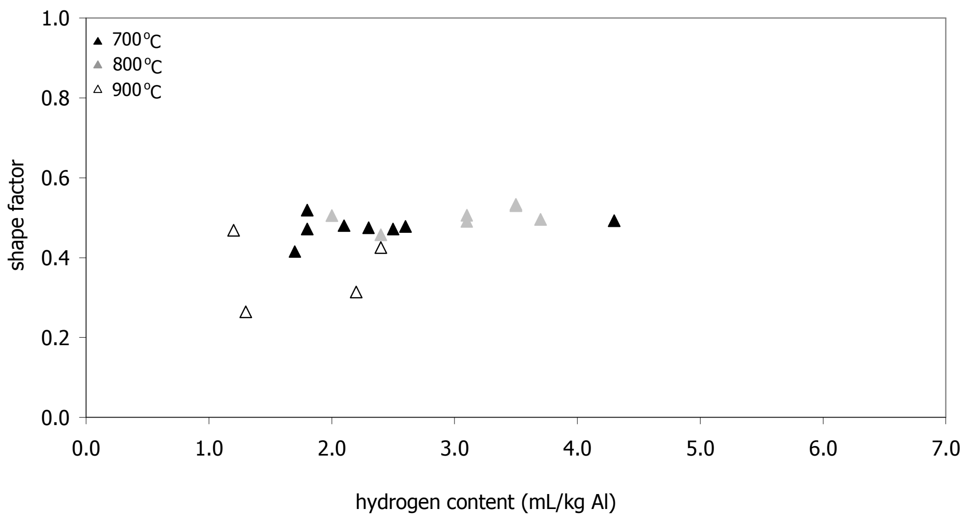

Figure 4.32: *shape factor change with the hydrogen level (LM4: RPT at 200 mbar)*

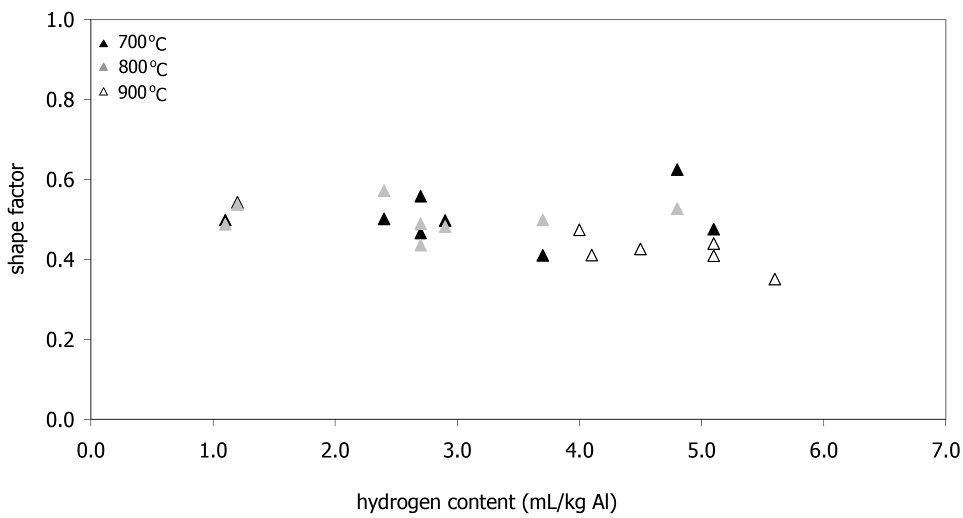

Figure 4.33: *shape factor change with the hydrogen level (LM4: RPT at 100 mbar)*

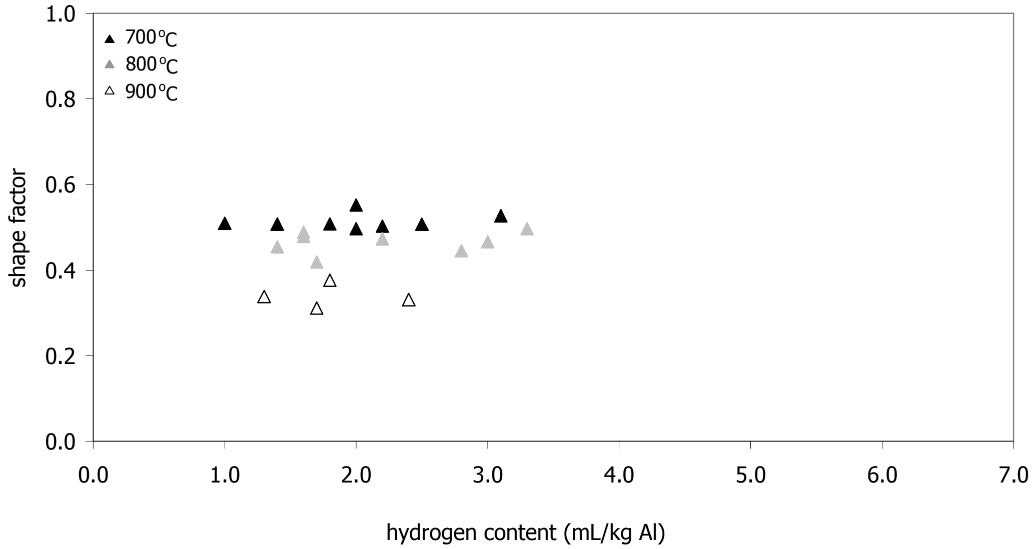

Figure 4.34: *shape factor change with the hydrogen level (LM4: RPT at 50 mbar)*

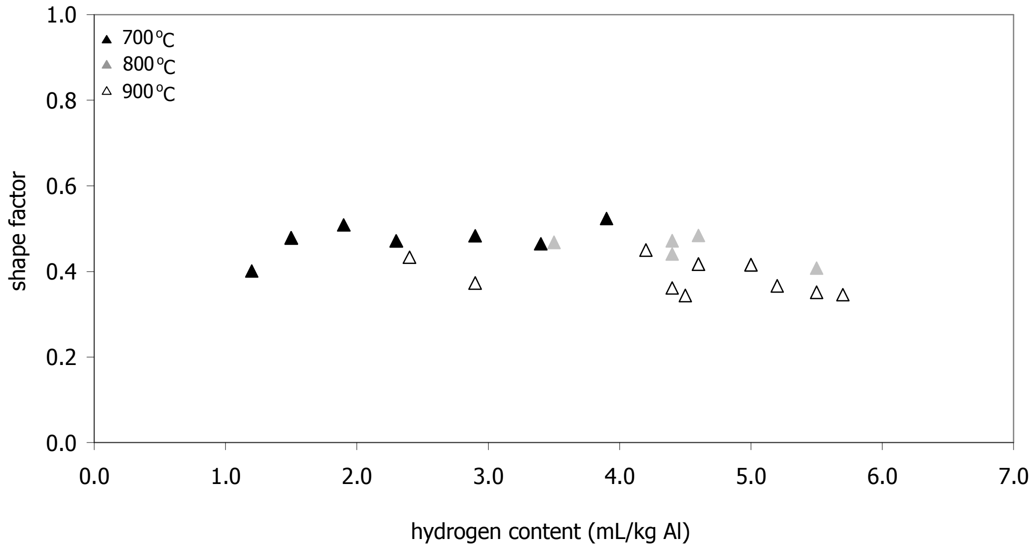

Figure 4.35: *shape factor change with the hydrogen level (LM4: RPT at 10 mbar)*

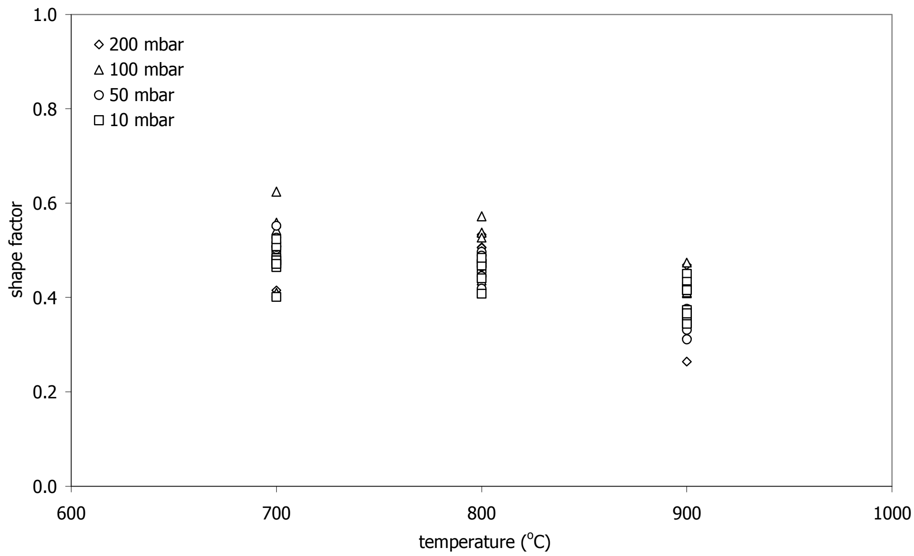

Figure 4.36: *shape factor change with temperature at different vacuum levels (LM4)*

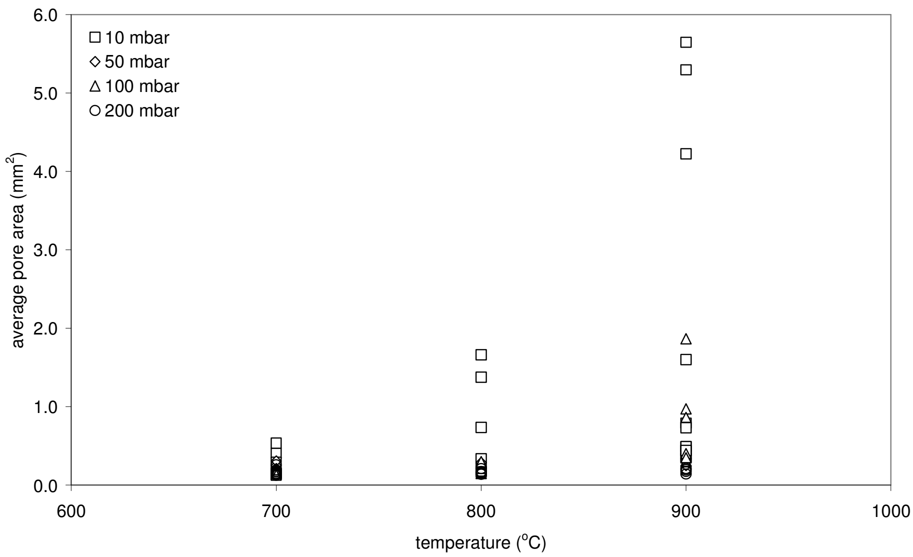

Figure 4.37: *average pore area with temperature and pressure (LM4)*

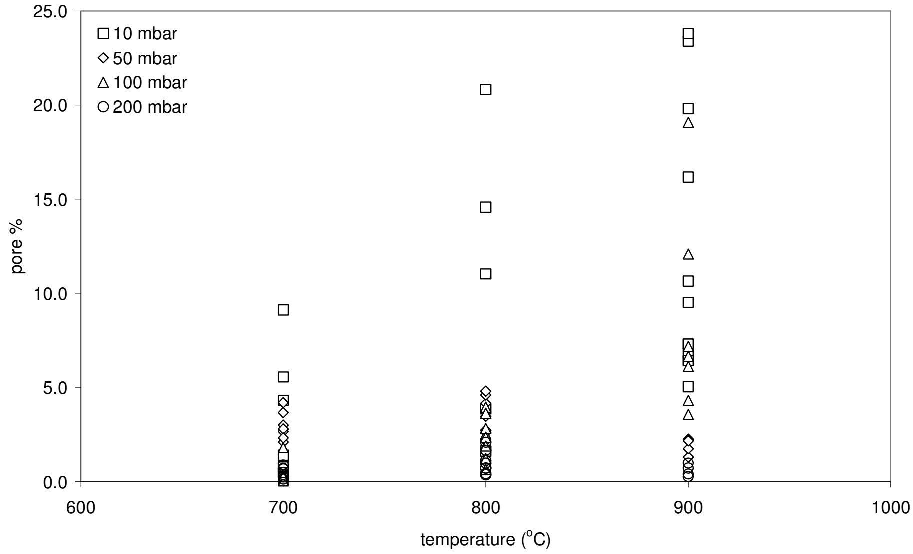

Figure 4.38: *porosity % versus temperature and pressure (LM4)*

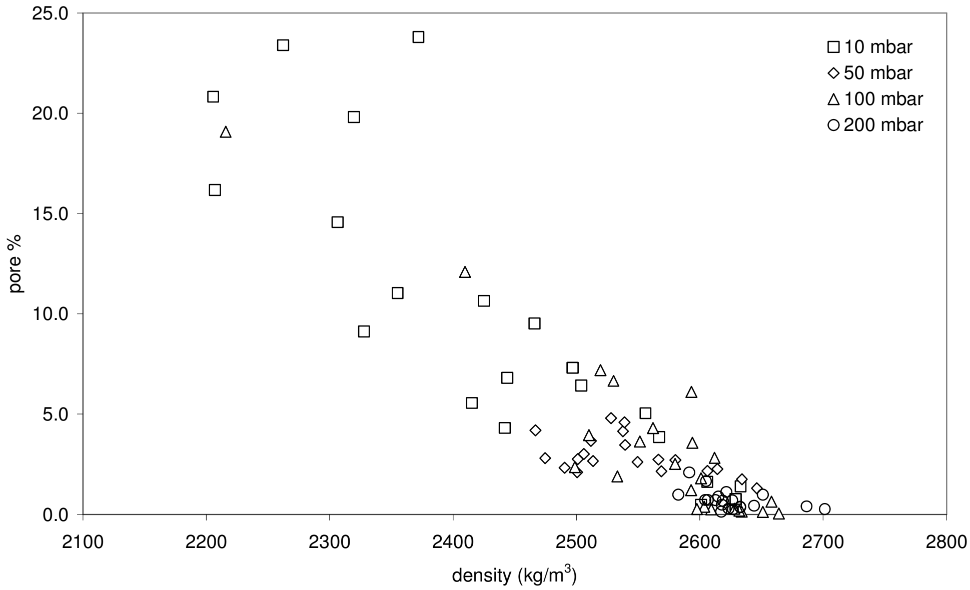

Figure 4.39: *Porosity % versus density and pressure (LM4: at all temperatures)*

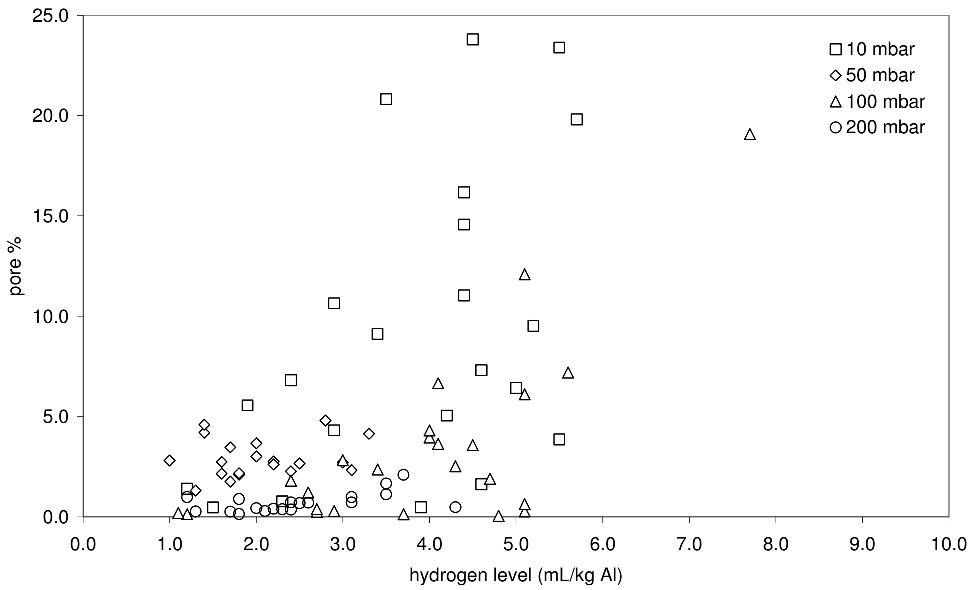

Figure 4.40: *relationship between porosity %, hydrogen and pressure (LM4: at all temperatures)*

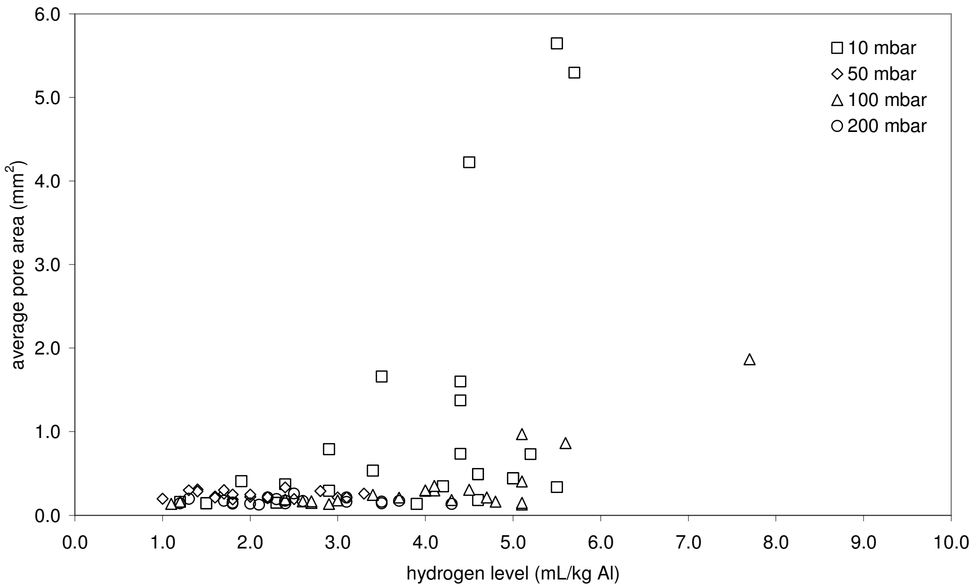

Figure 4.41: *relationship between average pore area with hydrogen and pressure (LM4: at all temperatures)*

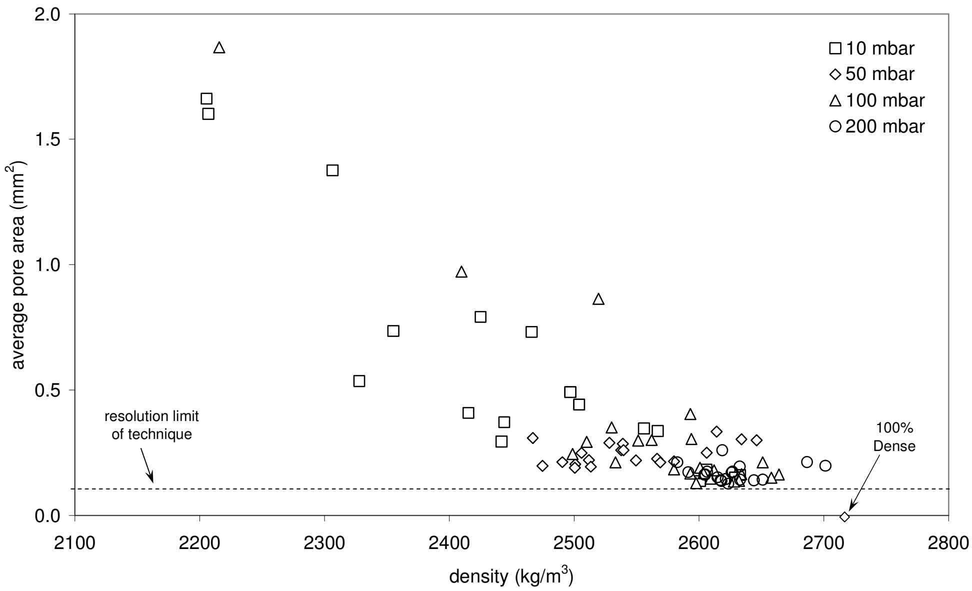

Figure 4.42: *average pore area change with density (LM4: at all temperatures)*

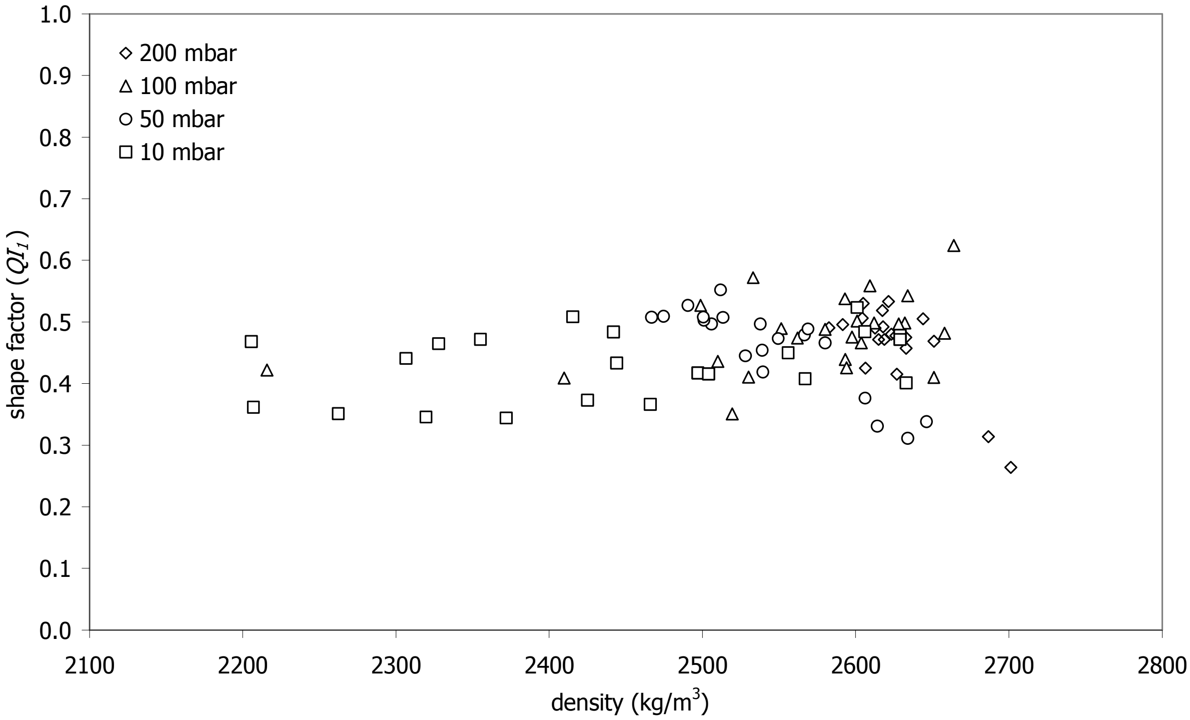

(a)

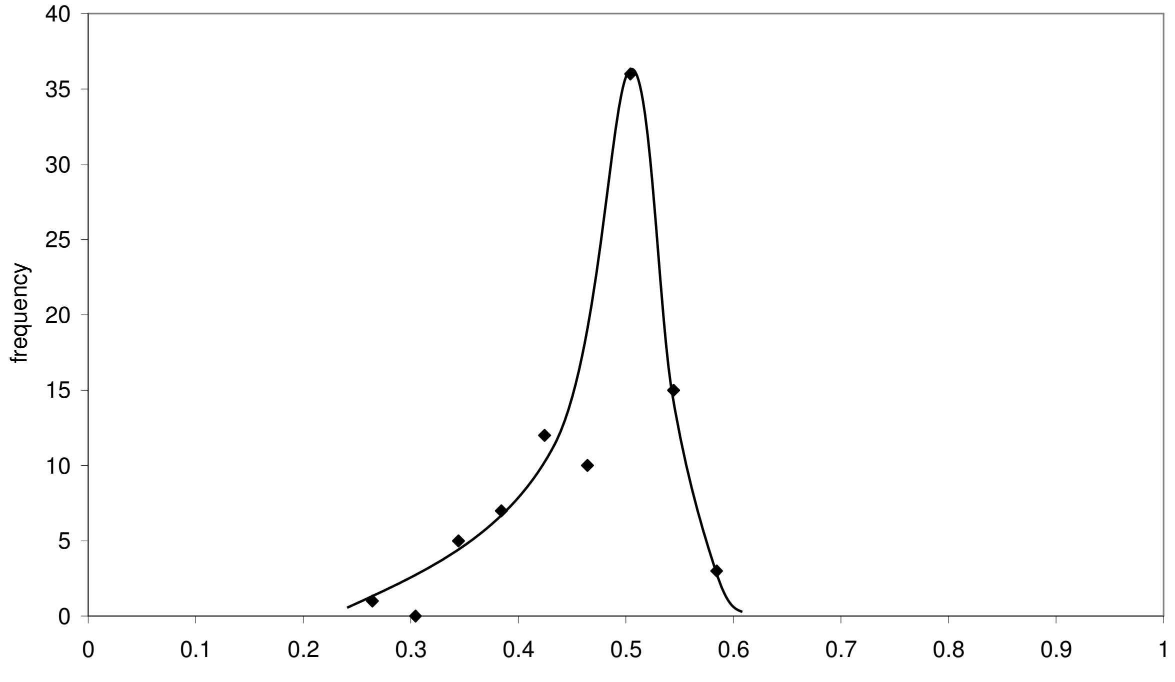

(b)

Figure 4.43: *alloy LM4: (a) shape factor change with density at different vacuum levels (b) shape factor distribution*

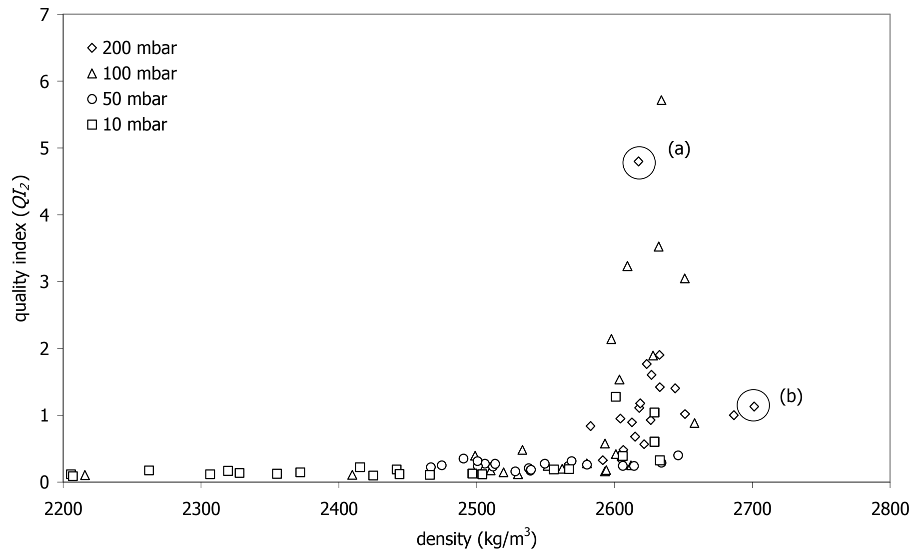

Figure 4.44: *quality index (QI_2) change with the RPT density (Alloy LM4)*
(a: QI_2=5, density=2600 kg/m^3, b: QI_2=1, density=2700 kg/m^3)

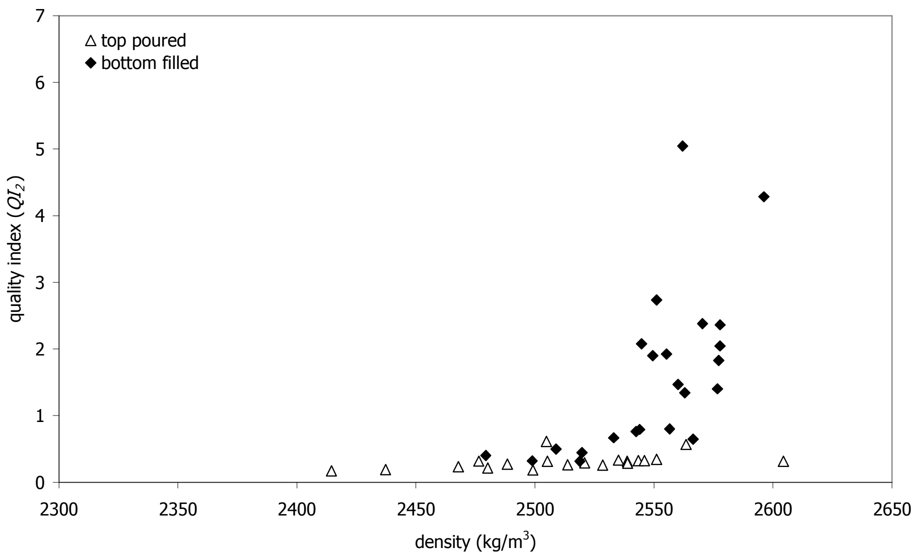

(a)

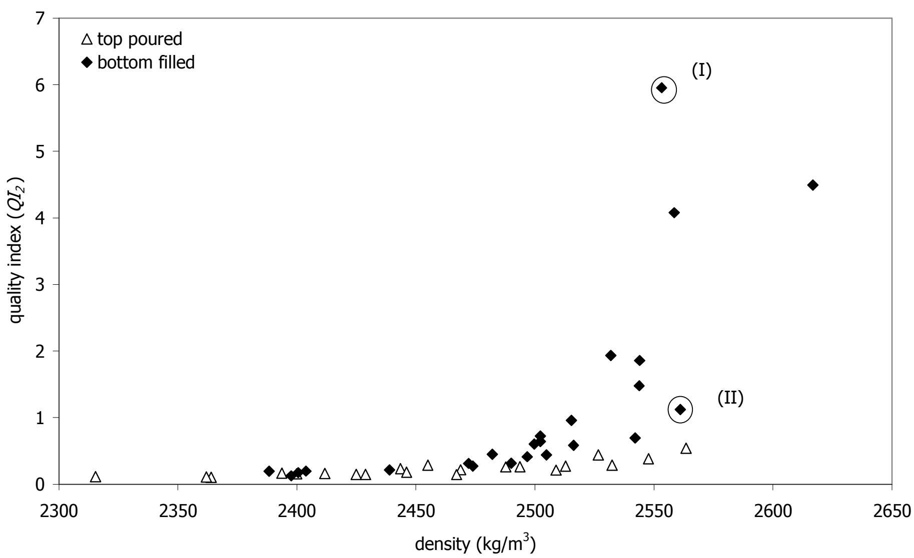

(b)

Figure 4.45: *quality index (QI_2) change with the density (Alloy LM24); Comparison of different castings heights*
(a) 100 mbar, (b) 50 mbar

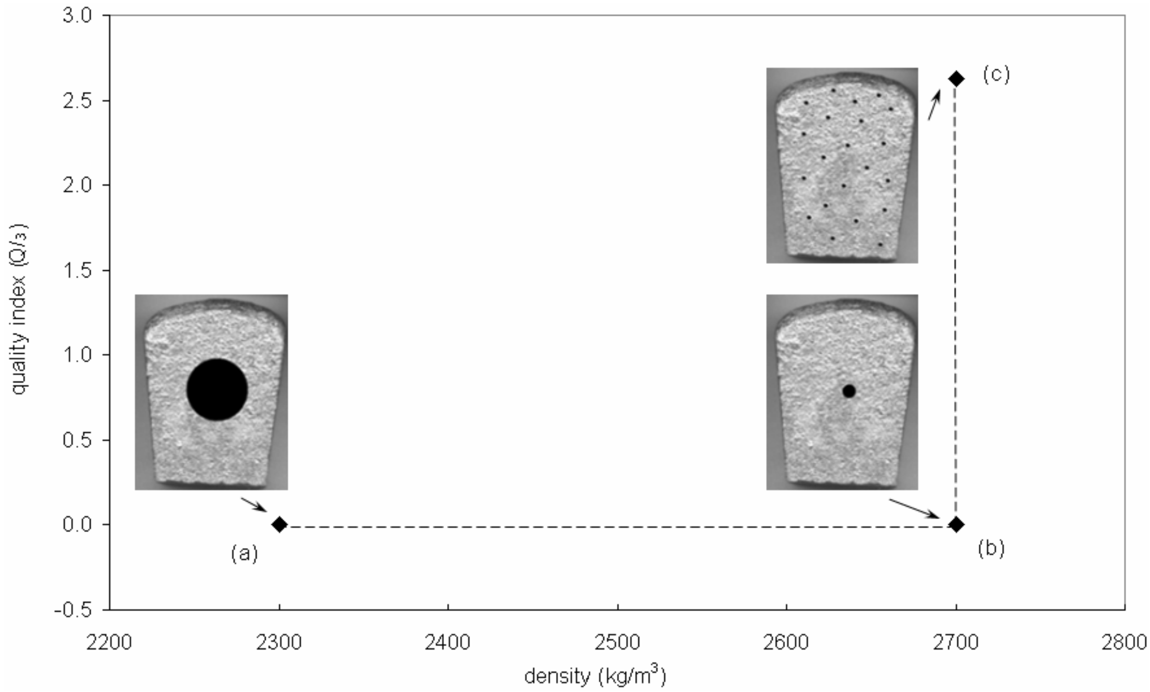

Figure 4.46: *Concept of QI_3 change with density*

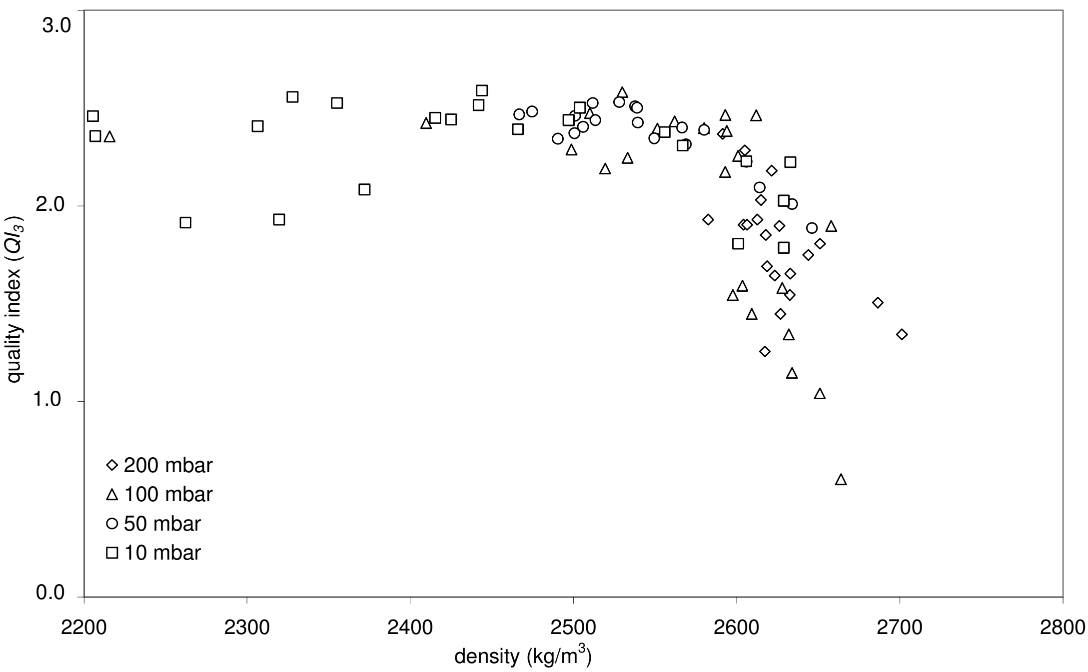

Figure 4.47: *QI_3 change with density - data from experiments (LM4)*

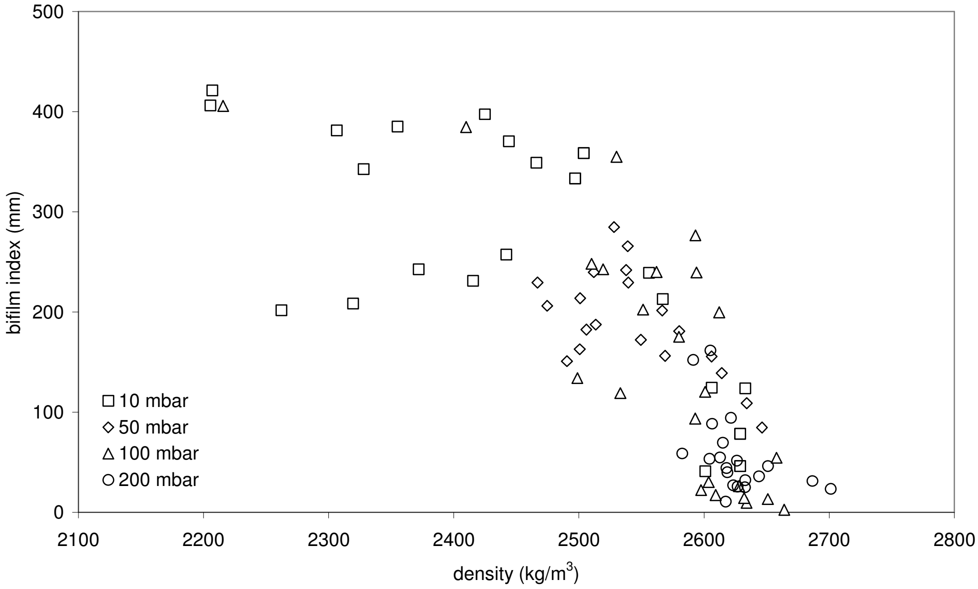

Figure 4.48: *Bifilm index versus density at different vacuum levels (LM4) (all temperatures)*

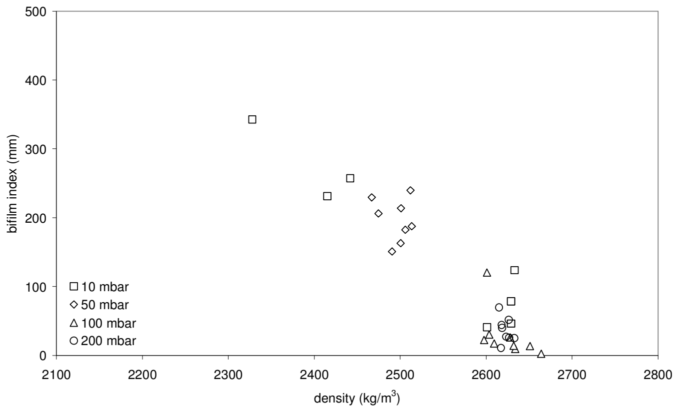

(a)

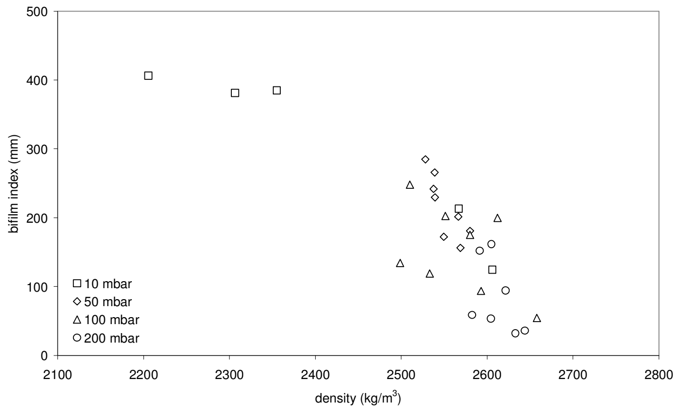

(b)

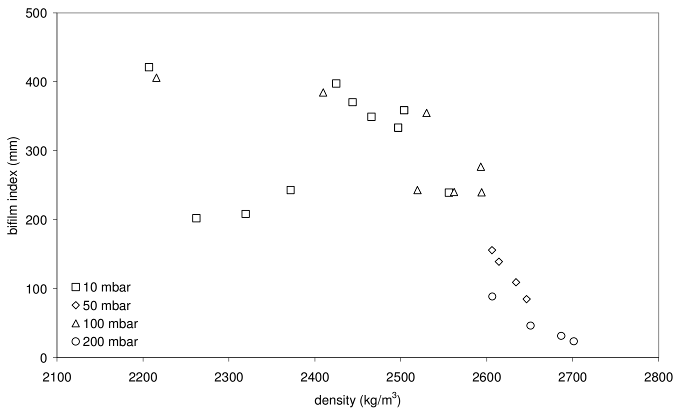

(c)

Figure 4.49: *Bifilm index versus density at different vacuum levels (LM4) (a) 700°C, (b) 800°C, (c) 900°C*

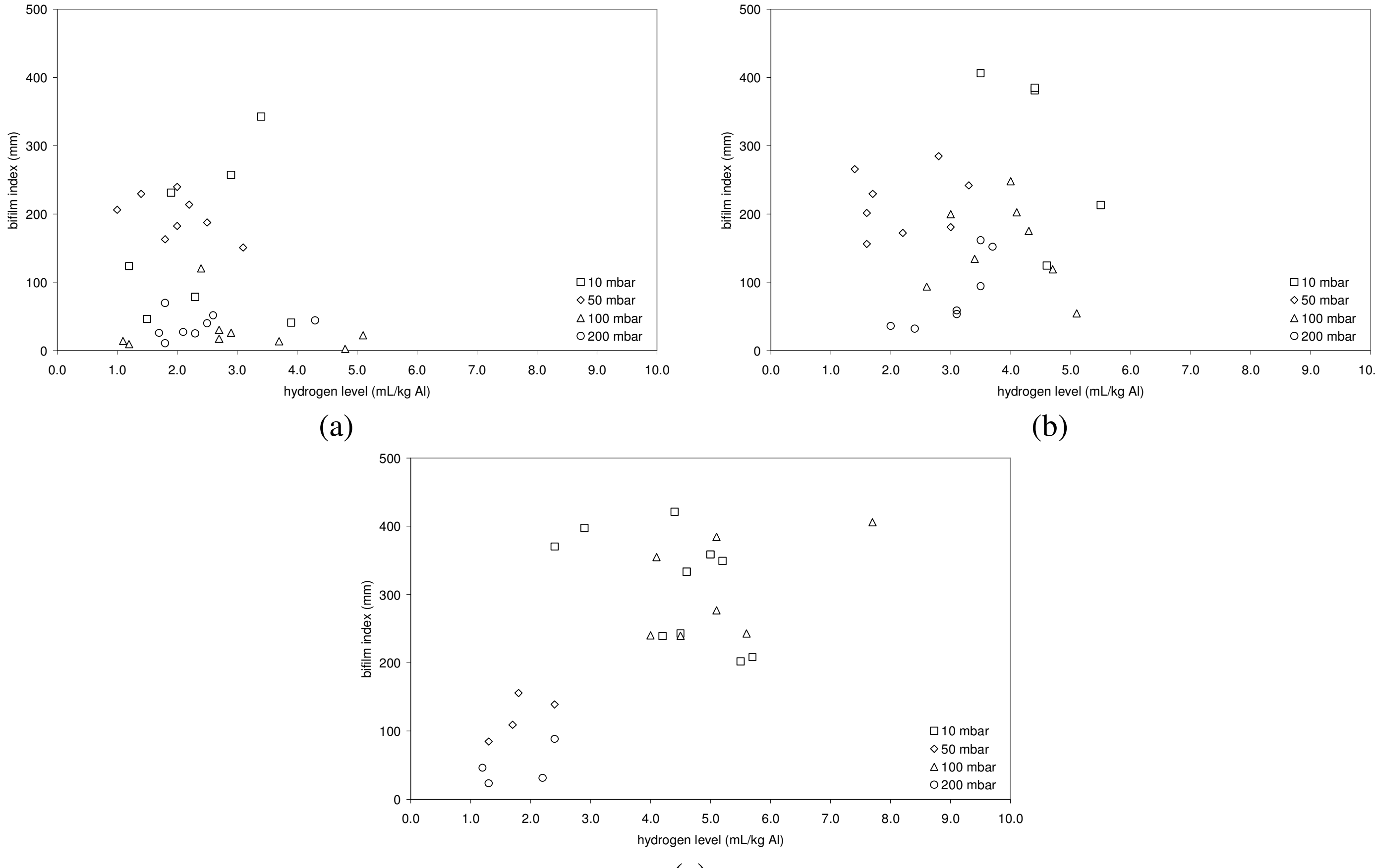

Figure 4.50: *Bifilm index versus hydrogen at different vacuum levels (LM4) (a) 700^oC, (b) 800^oC, (c) 900^oC*

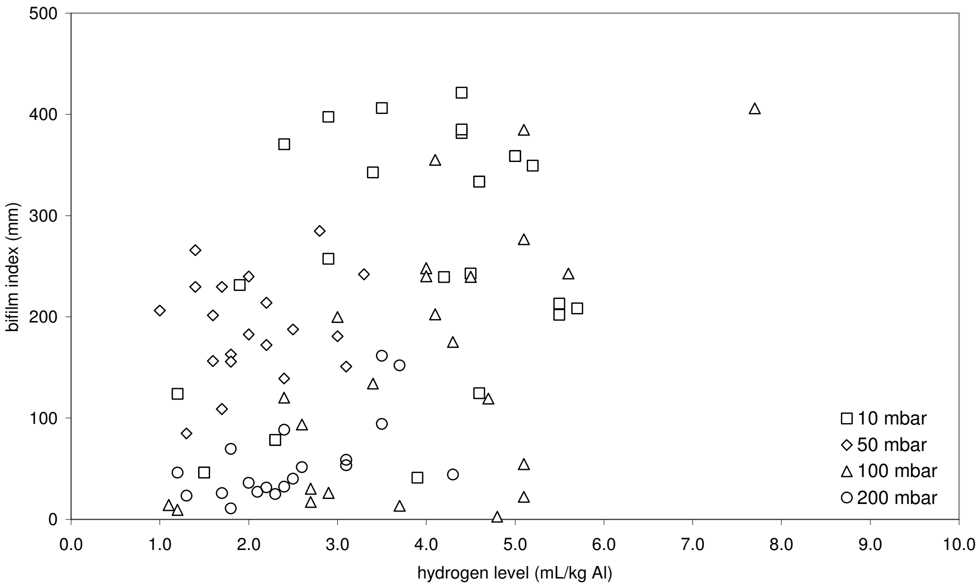

Figure 4.51: *Bifilm index versus hydrogen at different vacuum levels (LM4) (all data from Figure 4.50 superimposed here on the same graph)*

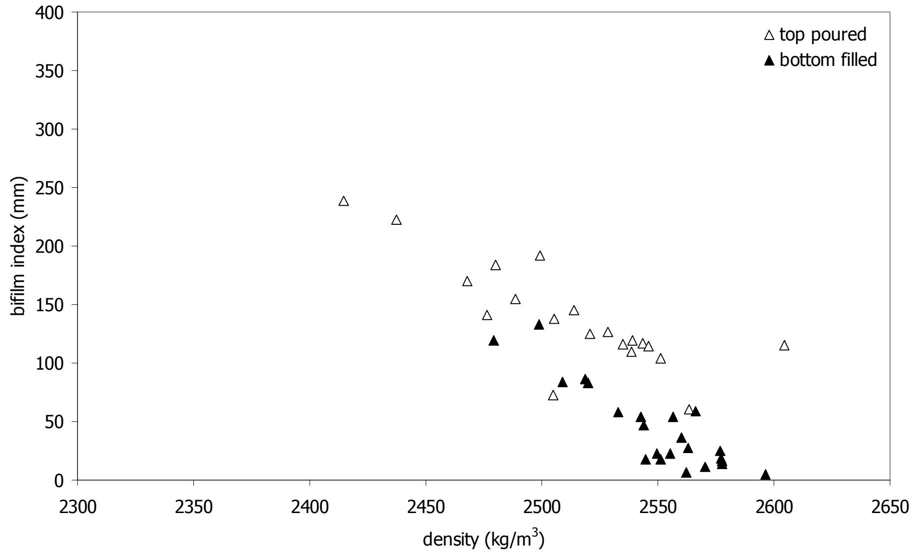

(a)

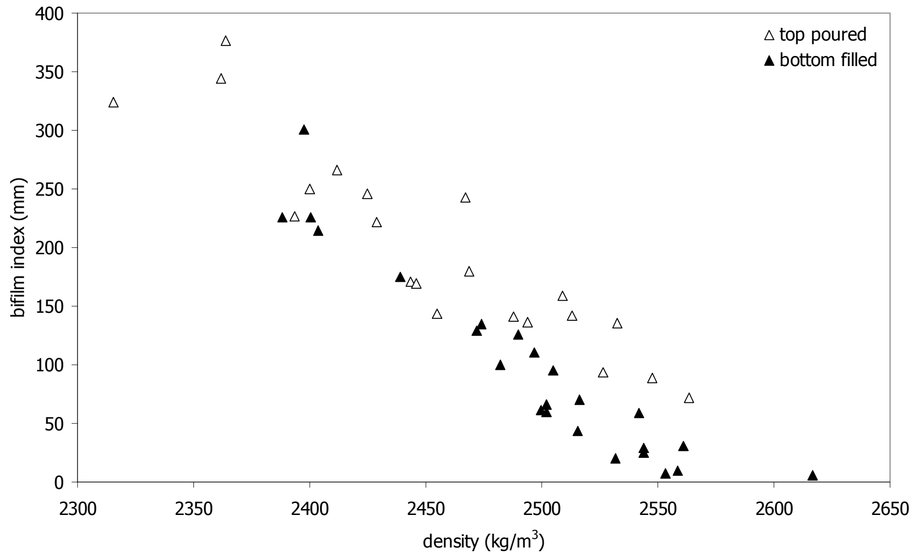

(b)

Figure 4.52: *Bifilm index versus density as a function of casting height; LM24 (a) 100 mbar, (b) 50 mbar*

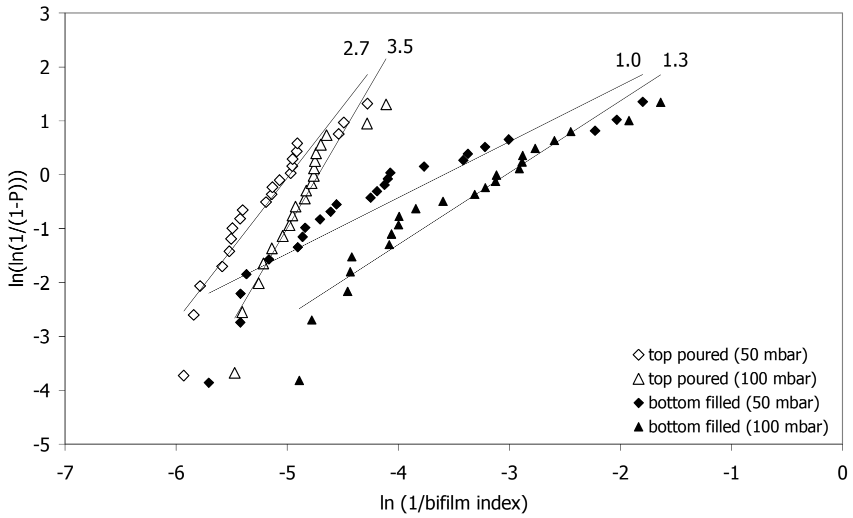

Figure 4.53: *Weibull distribution change of bifilm index of different casting heights (LM24)*

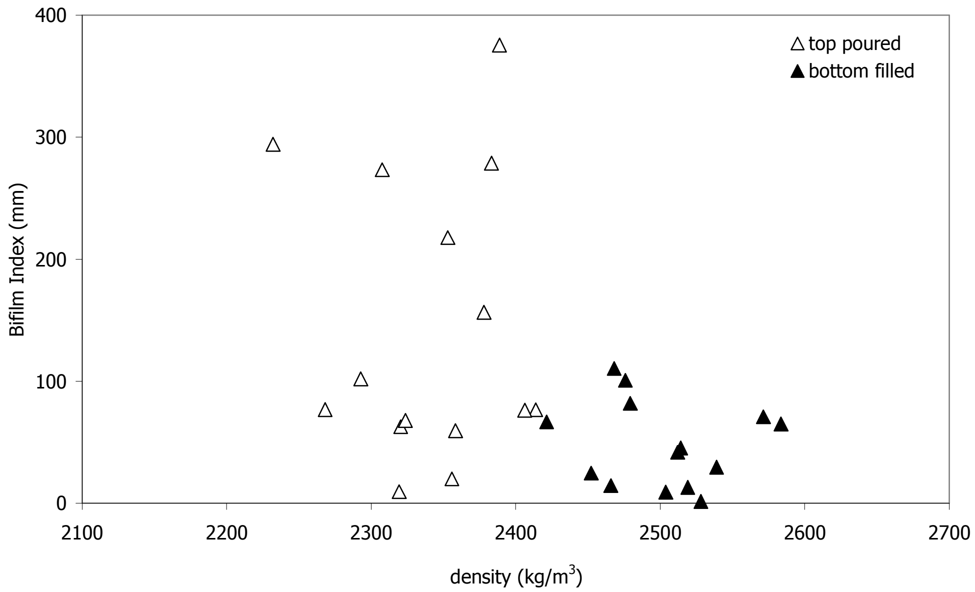

Figure 4.54: *Bifilm index versus density; LM25 (100 mbar)*

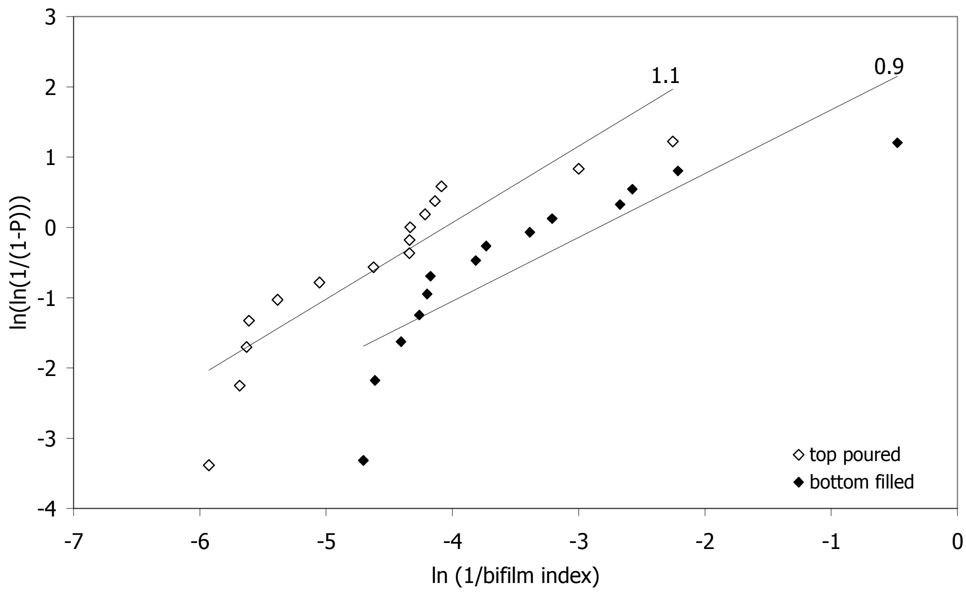

Figure 4.55: *Weibull distribution change of bifilm index of different casting heights (LM25 - 100 mbar)*

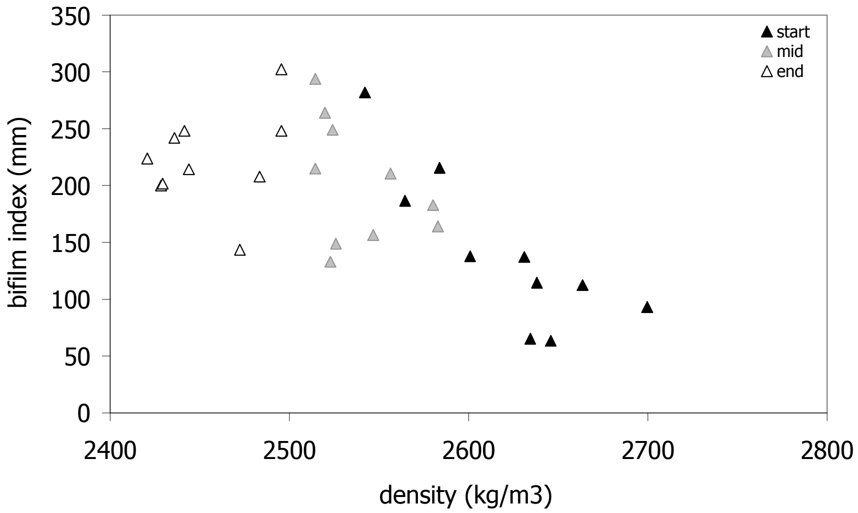

(a)

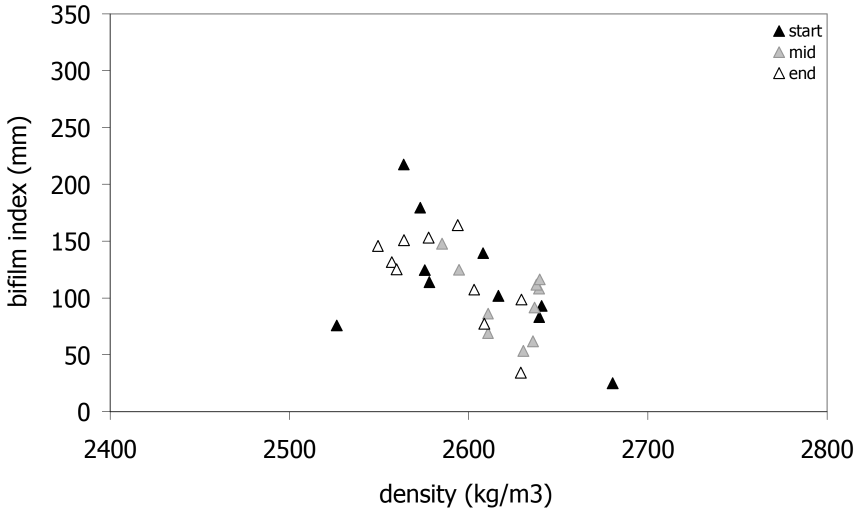

(b)

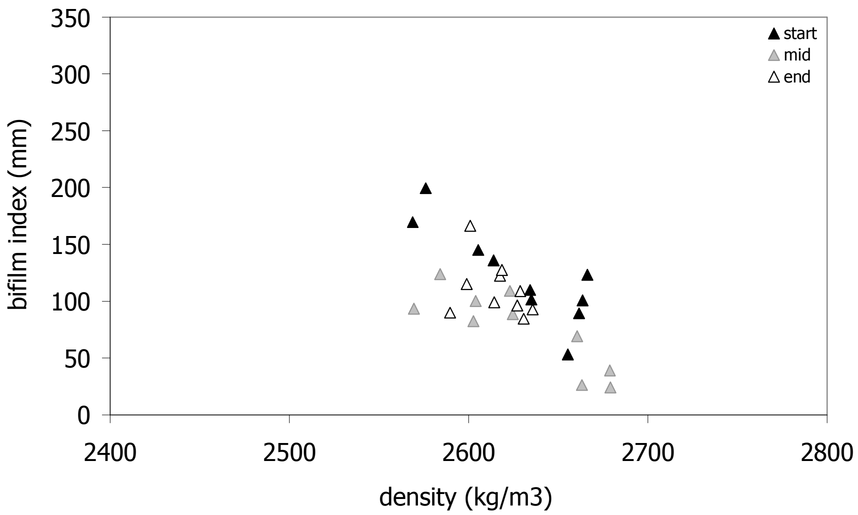

(c)

Figure 4.56: *Bifilm index versus density (LM24-100 mbar)*
(a) 0 diffuser
(b) 1 diffuser
(c) 2 diffusers

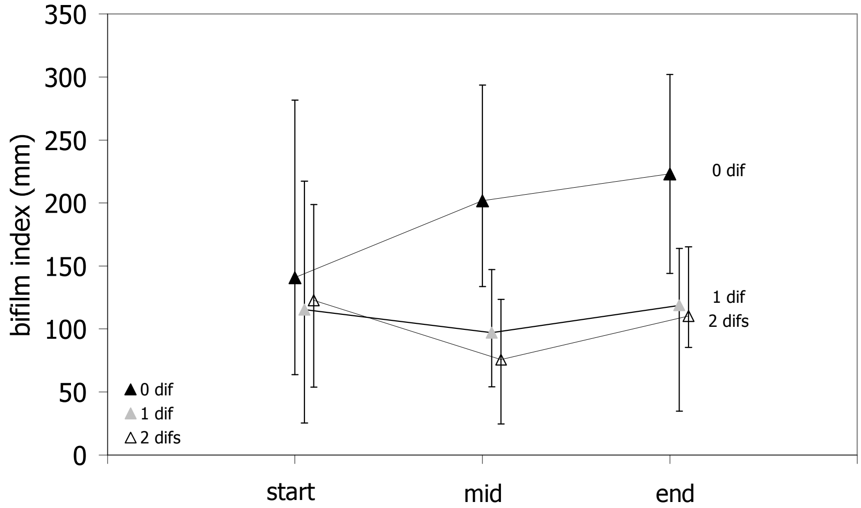

Figure 4.57: *Bifilm index (determined at 100 mbar) change from start, mid to end Comparing different number of diffusers (LM24)*

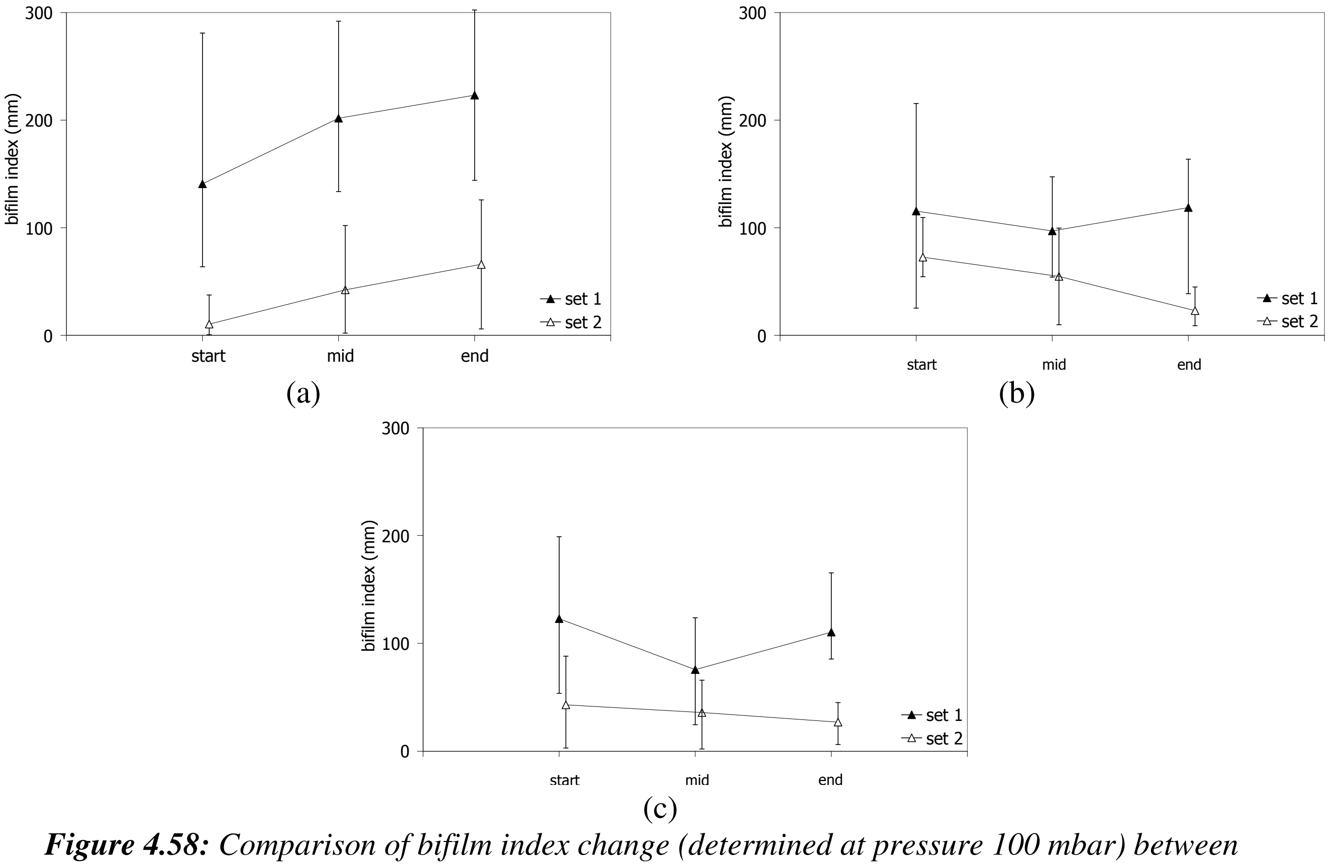

Figure 4.58: *Comparison of bifilm index change (determined at pressure 100 mbar) between non-quiescent (SET 1) and quiescent conditions (SET 2)*
(a) 0 diffuser, (b) 1 diffuser, (c) 2 diffusers

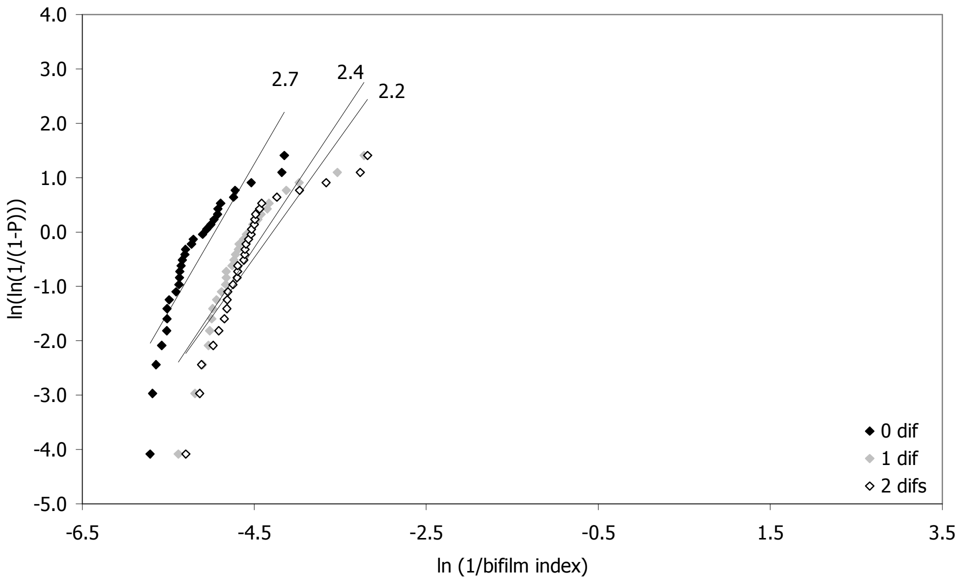

(a)

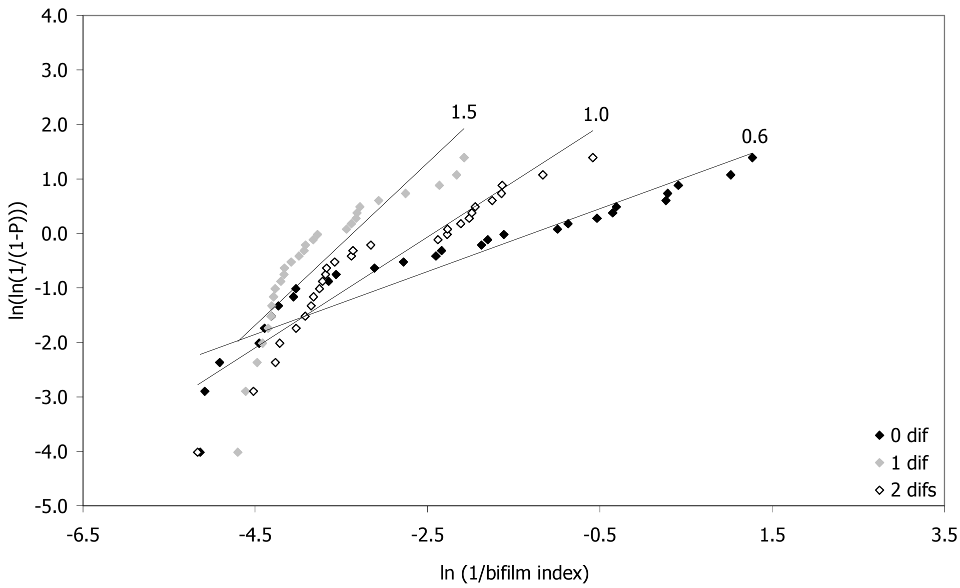

(b)

Figure 4.59: *Weibull distribution change of bifilm index of different casting conditions (LM24 -100 mbar)*

(a) Non-quiescent conditions (SET 1)

(b) Quiescent conditions (SET 2)

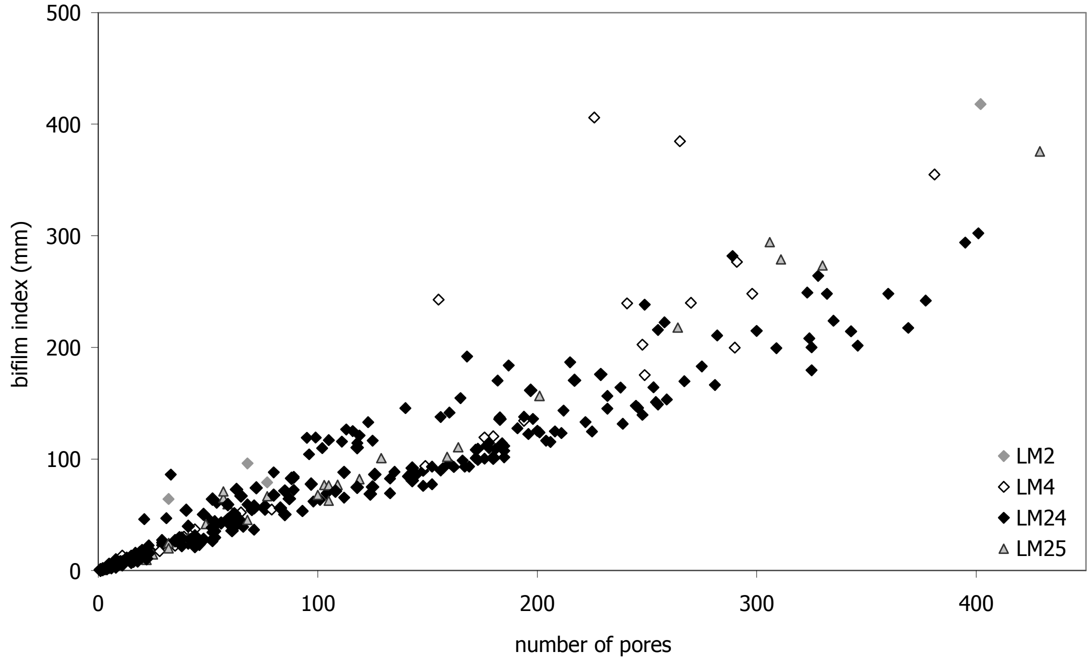

Figure 4.60: *The relationship between the number of pores and bifilm index (determined at pressure 100 mbar)*

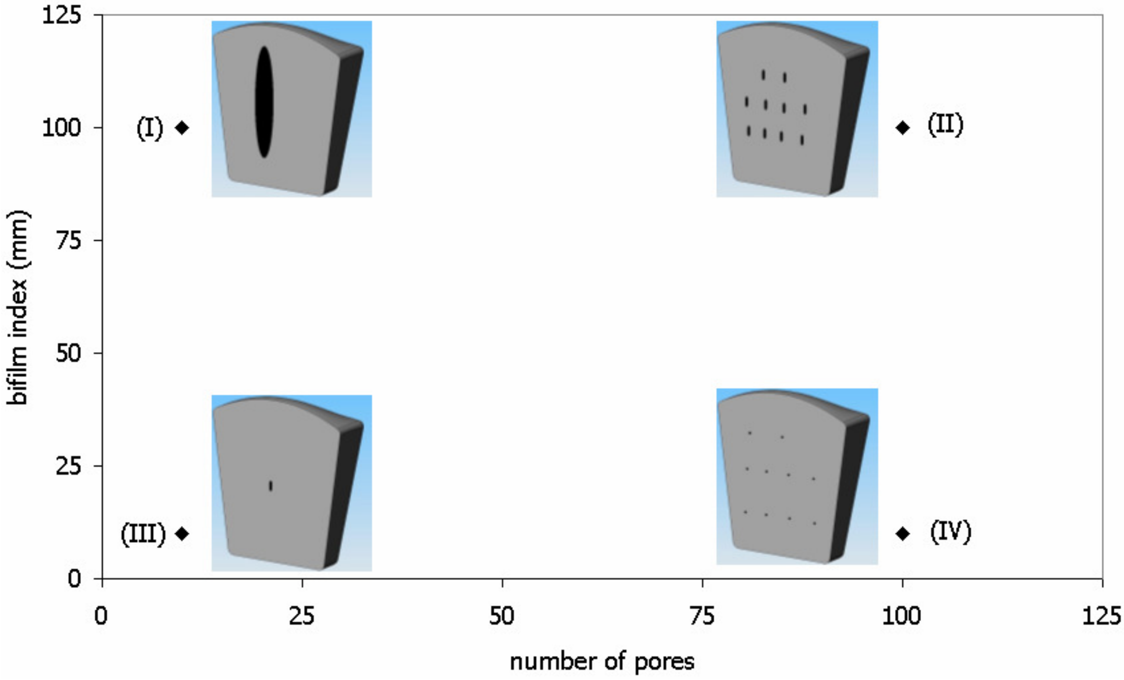

Figure 4.61: *Schematic illustration of sectioned surface of RPT samples illustrating the relationship between the number of pores and bifilm index*

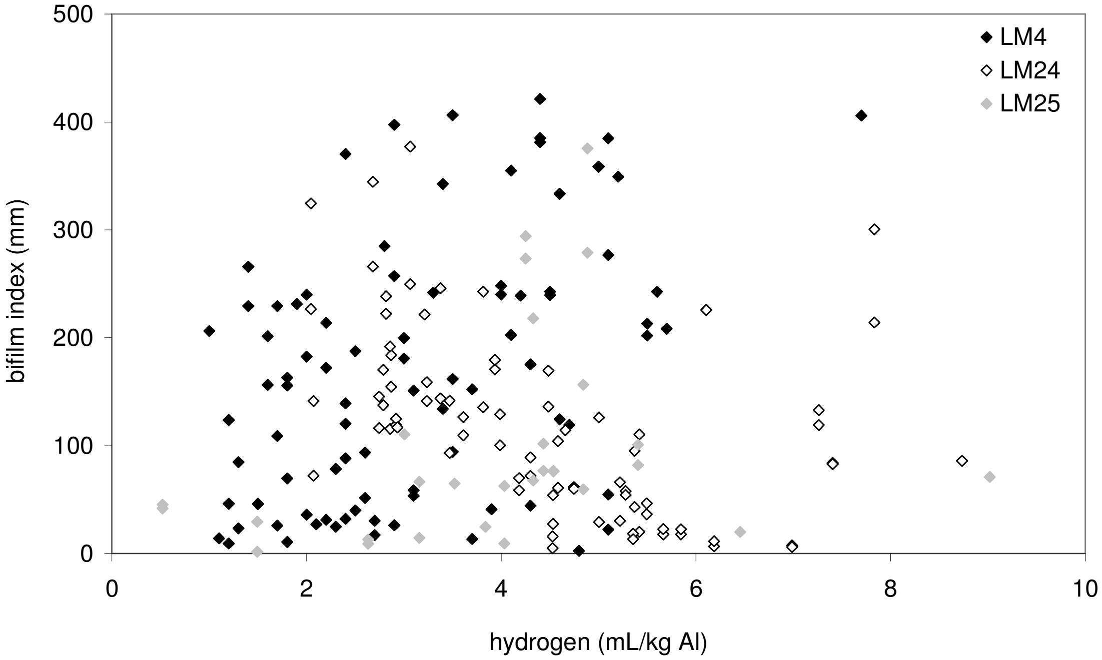

Figure 4.62: *The relationship between bifilm index (determined at 100 mbar) and hydrogen content of the melt*

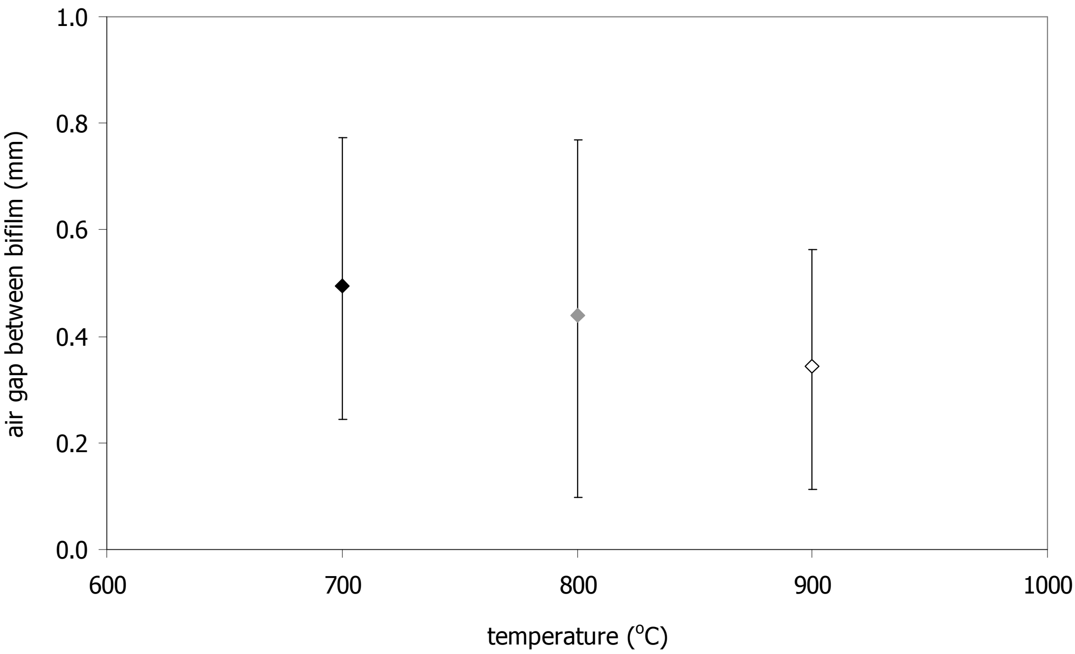

Figure 4.63: *Change in the average air gap between bifilms with temperature*

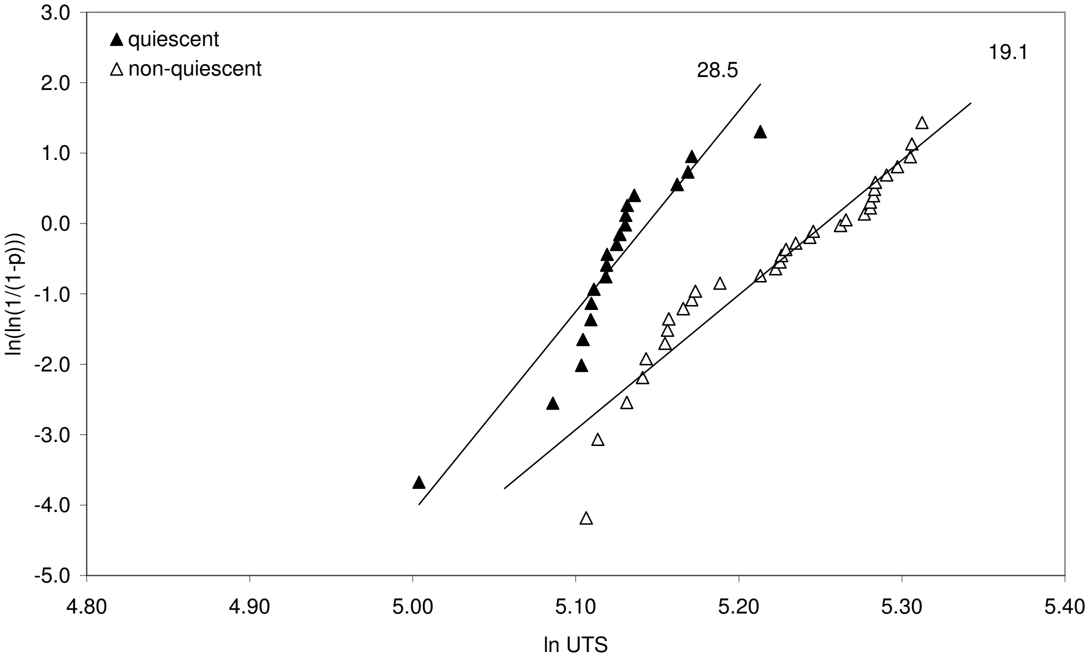

(a)

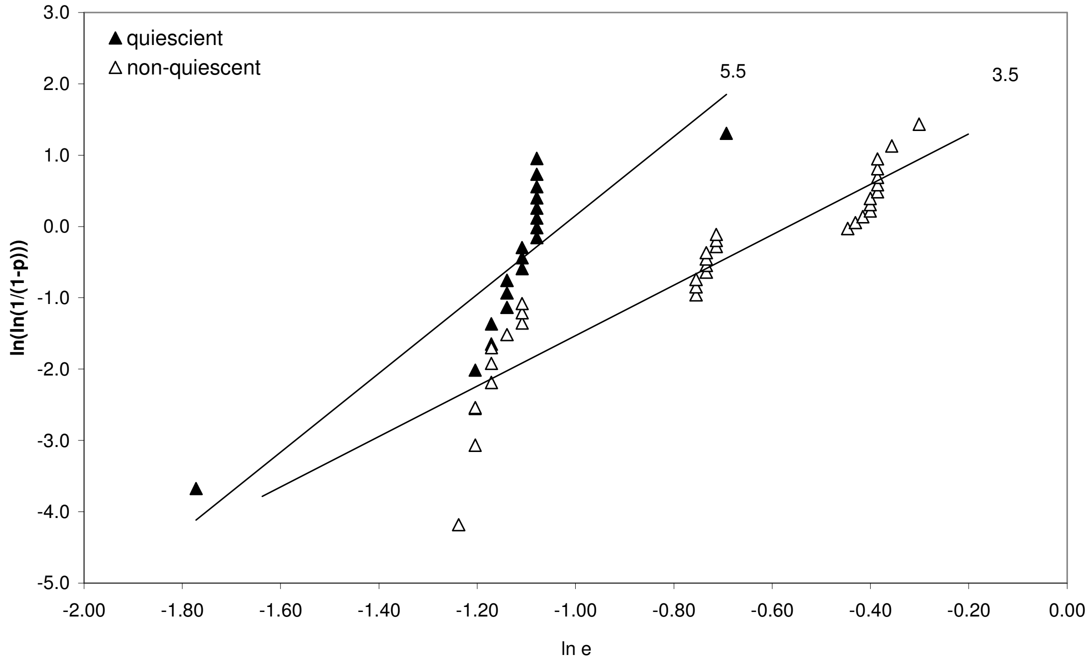

(b)

Figure 4.64: *Comparison of Weibull distribution of tensile properties developed under conditions of quiescent and non-quiescent filling: Alloy LM27 (a) UTS, (b) elongation*

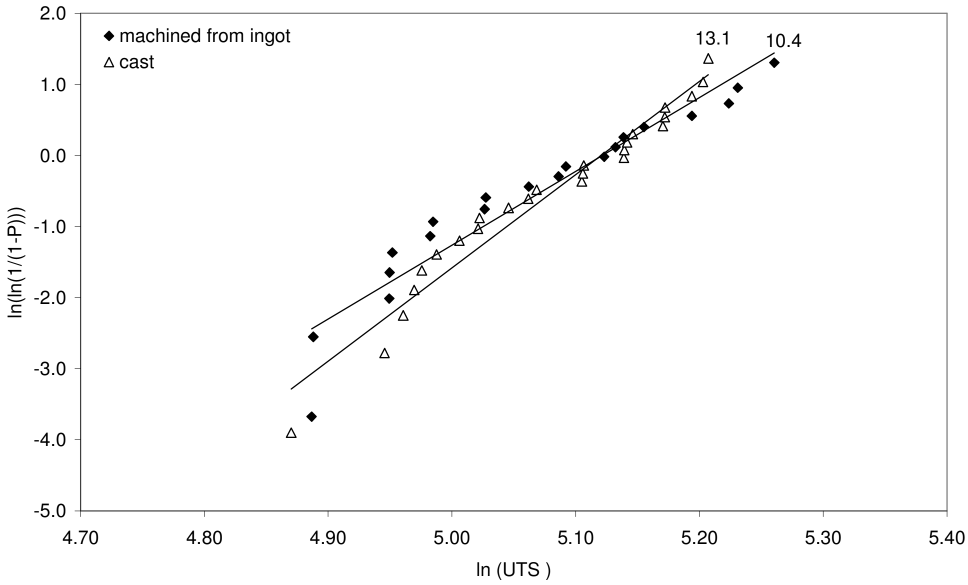

(a)

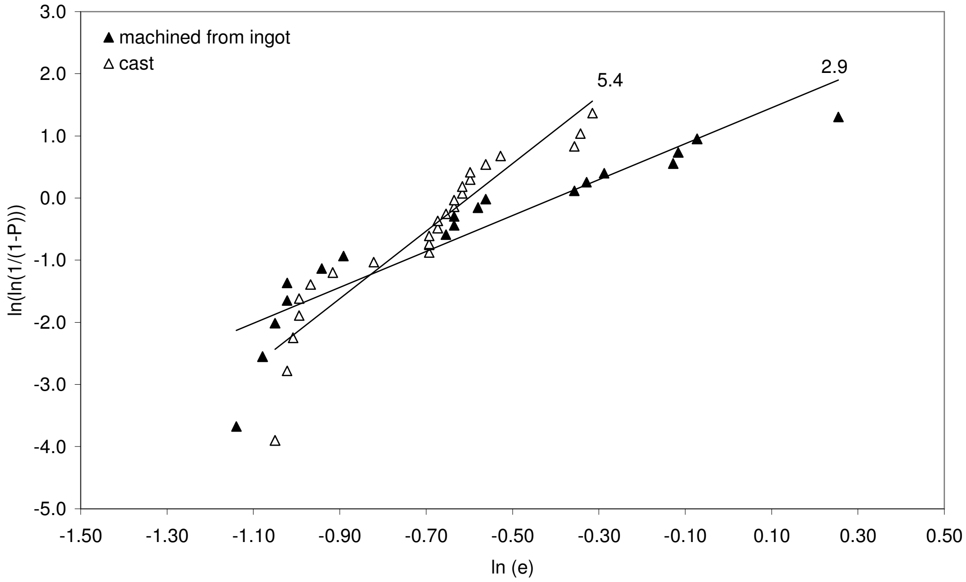

(b)

Figure 4.65: *Comparison of Weibull distribution of mechanical test results of bars obtained by machining of ingots and by re-melting and casting into test bars, Alloy LM4. (a) The Weibull plot of UTS and (b) the Weibull plot of elongation e*

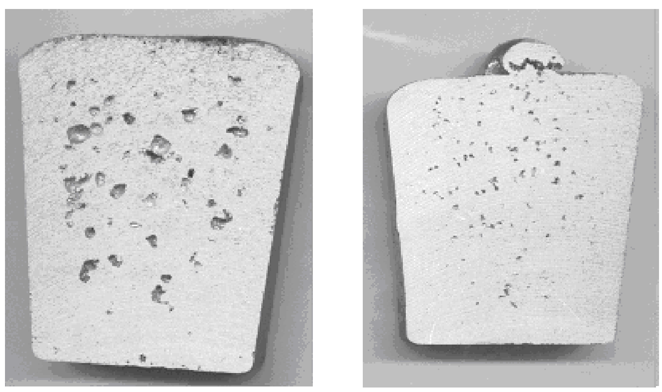

(a) (b)

Figure 4.66: *Sectioned surface of RPT samples alloy LM2 (100 mbar) (a) High Mg, (b) Low Mg*

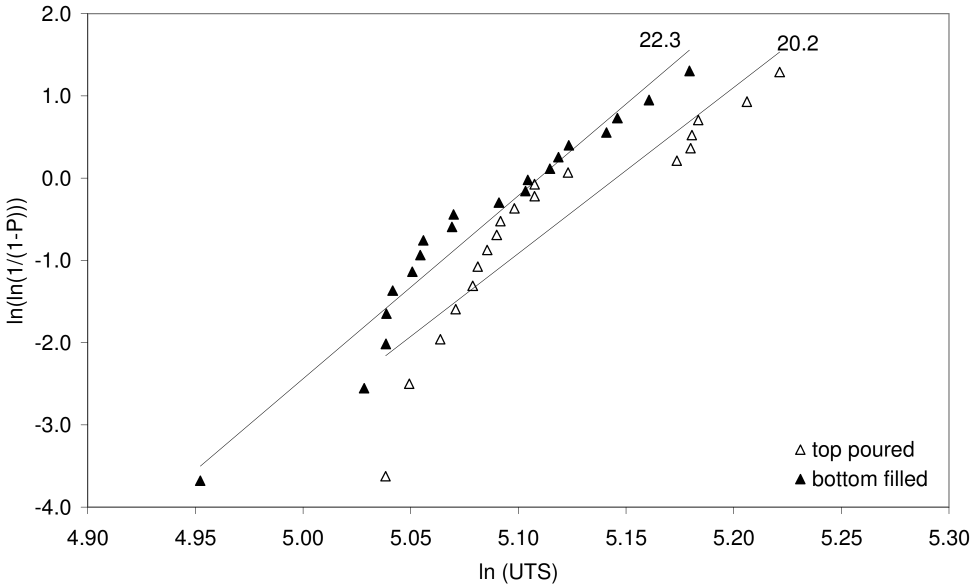

(a)

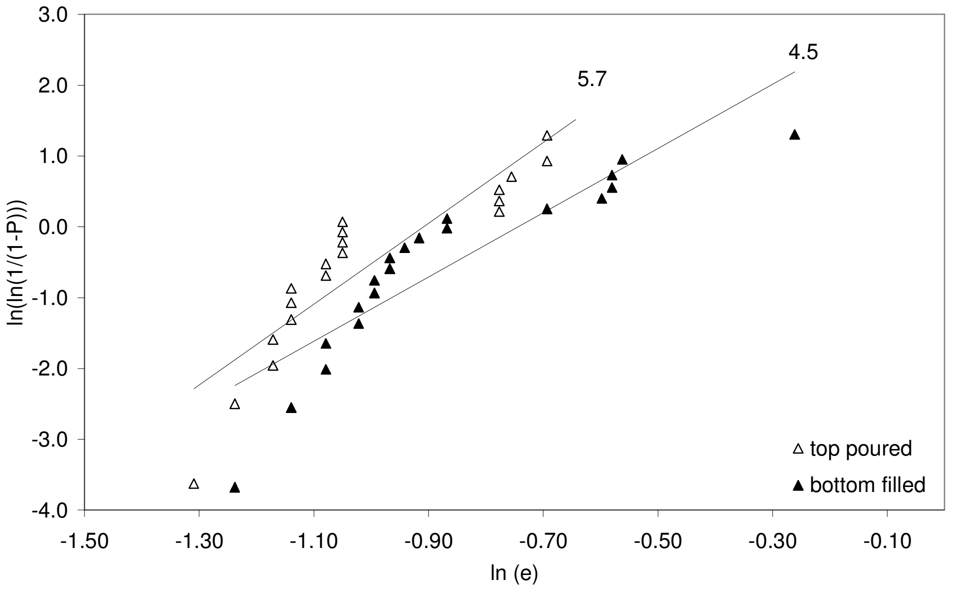

(b)

Figure 4.67: *Alloy LM2 Weibull distribution change of two different casting heights showing (a) UTS, (b) elongation*

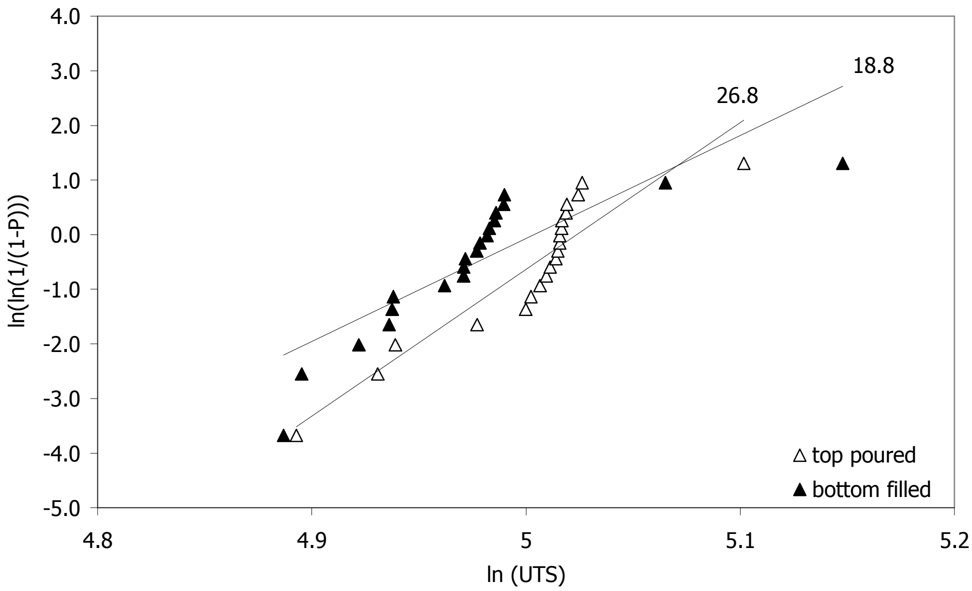

(a)

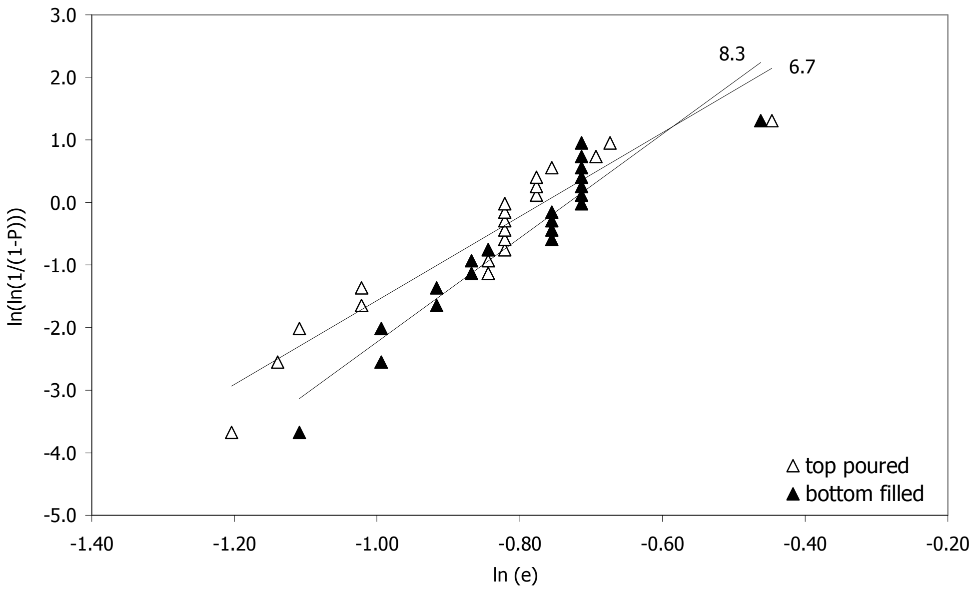

(b)

Figure 4.68: *Alloy LM2 (low Mg) Weibull distribution change of two different casting heights showing (a) UTS, (b) elongation*

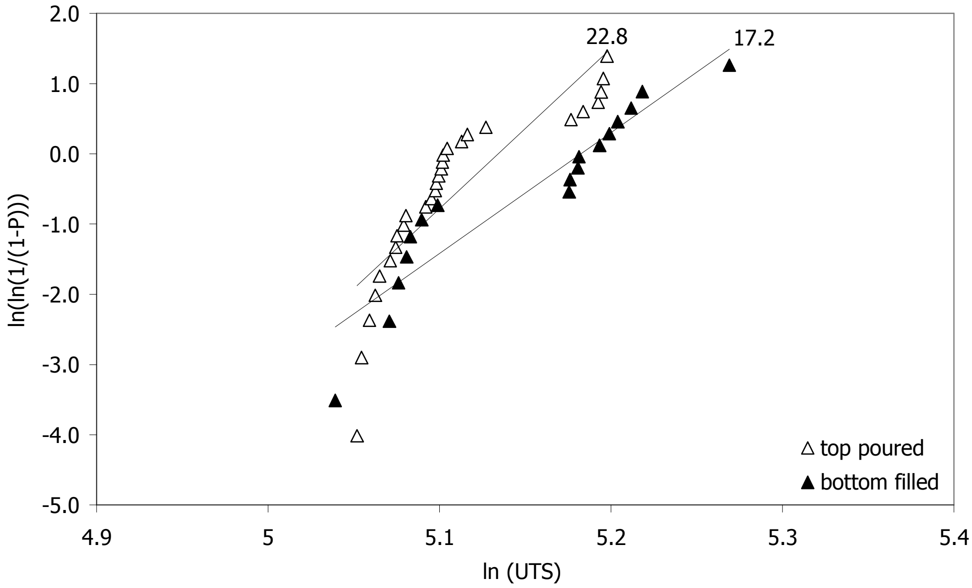

(a)

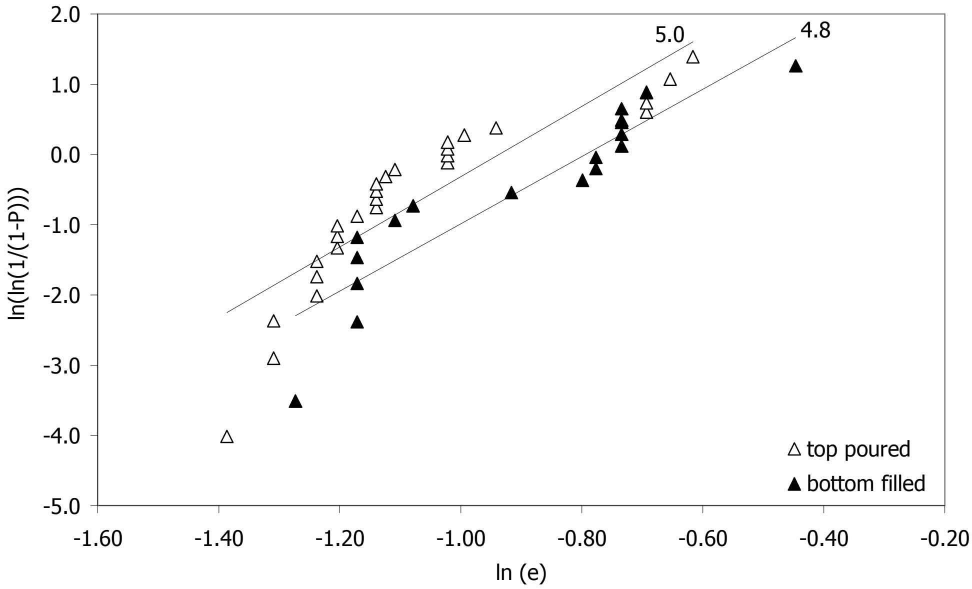

(b)

Figure 4.69: *Alloy LM2 (high Mg) Weibull distribution change of two different casting heights showing (a) UTS, (b) elongation*

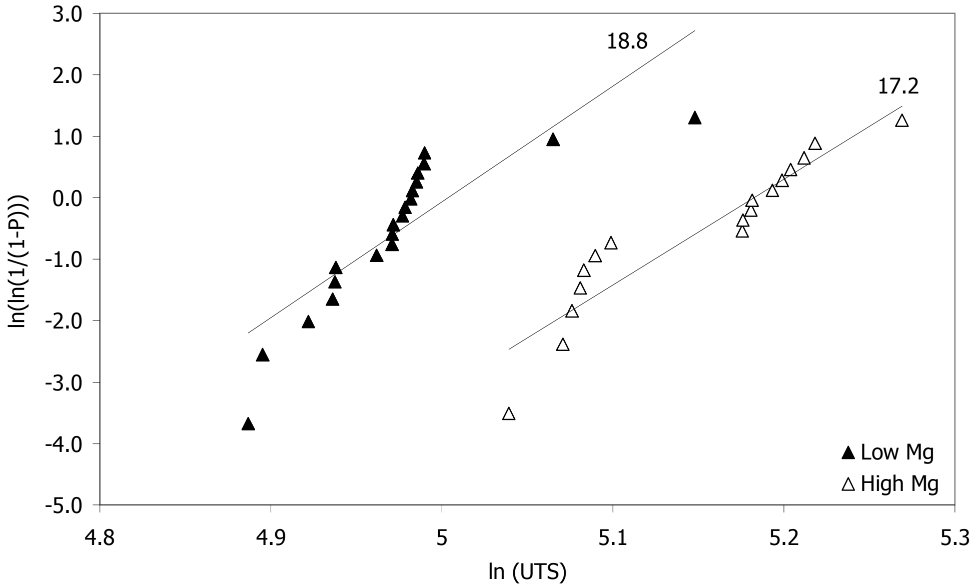

(a)

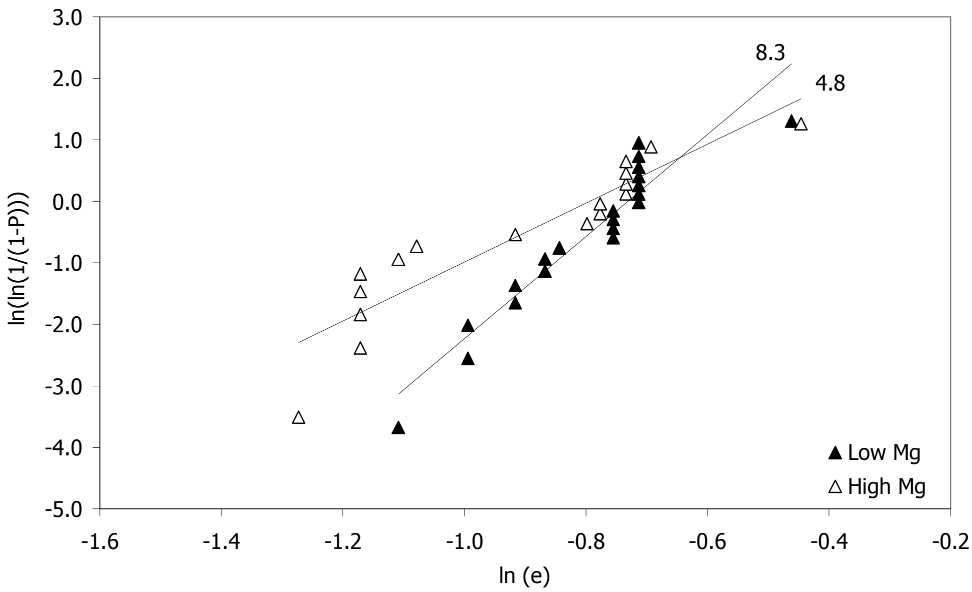

(b)

Figure 4.70: *Alloy LM2 (Bottom Filled): Weibull distribution change of different Mg content (a) UTS, (b) elongation values*

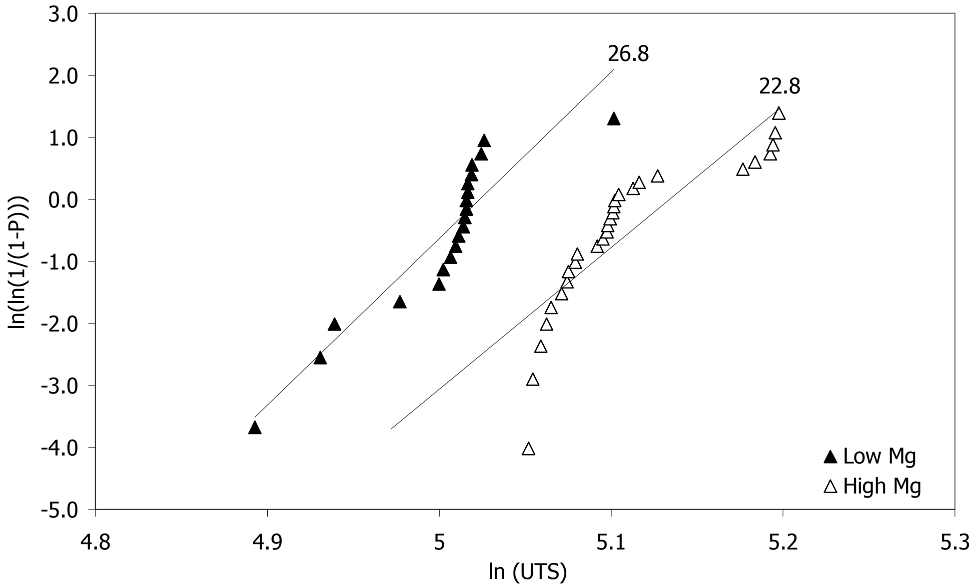

(a)

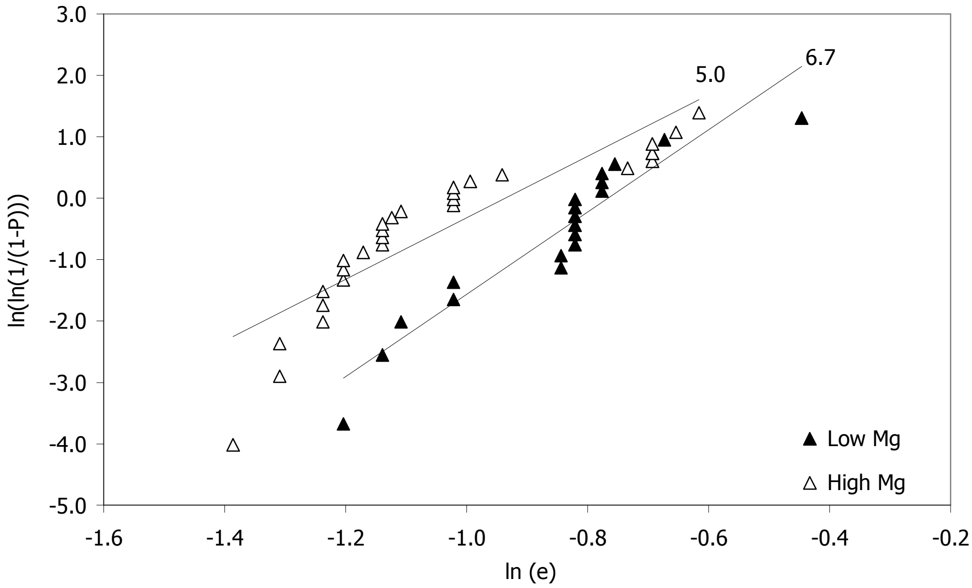

(b)

Figure 4.71: *Alloy LM2 (Top poured): Weibull distribution change of different Mg content (a) UTS, (b) elongation values*

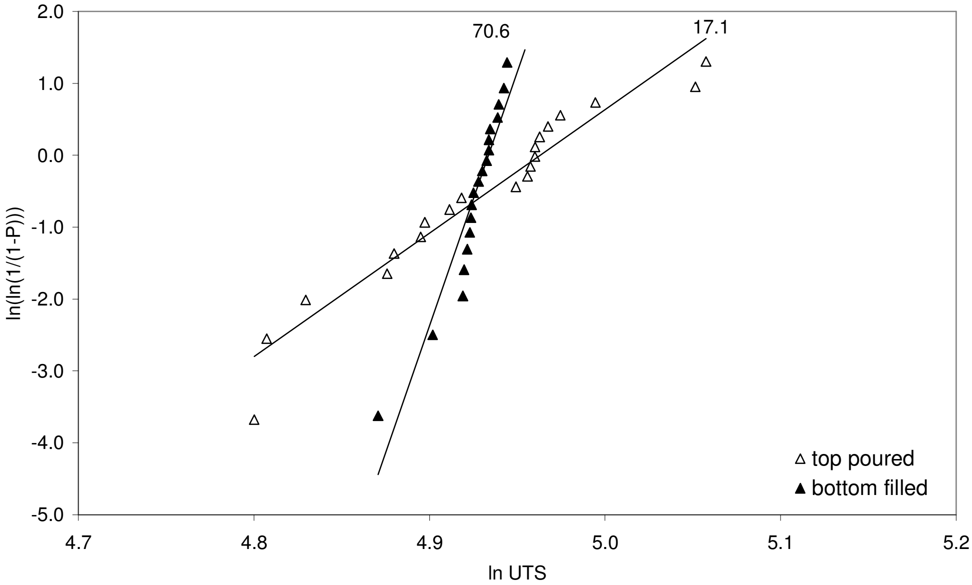

(a)

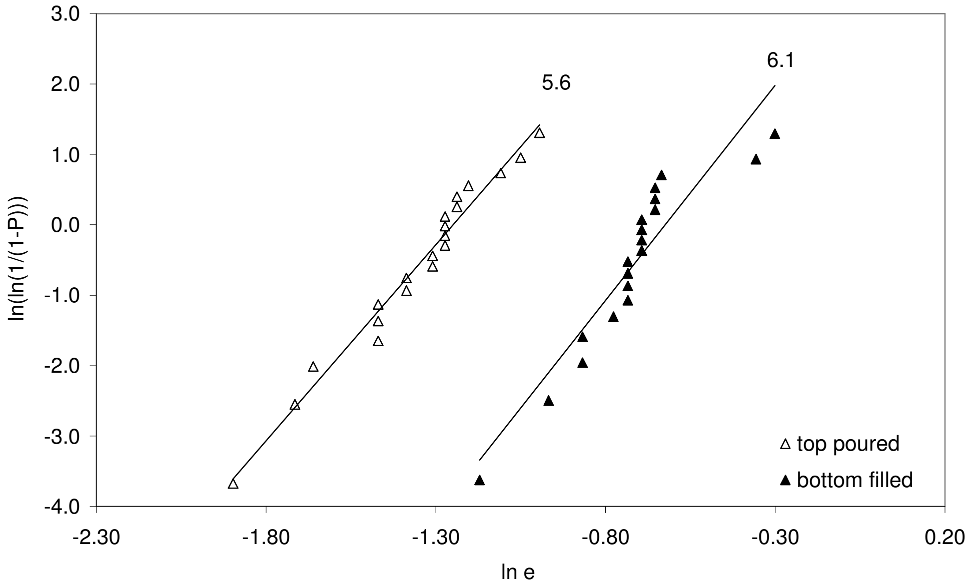

(b)

Figure 4.72: *Alloy LM2: Weibull distribution change of different casting height (a) UTS, (b) Elongation*

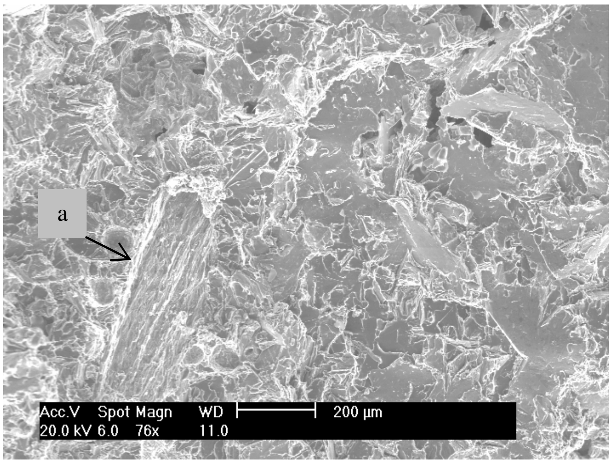

(a)

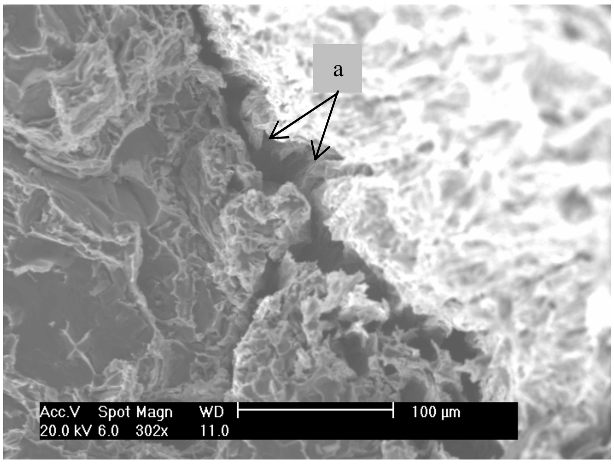

(b)

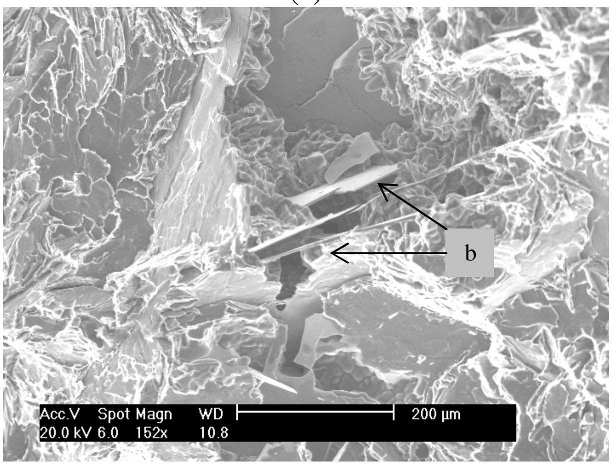

(c)

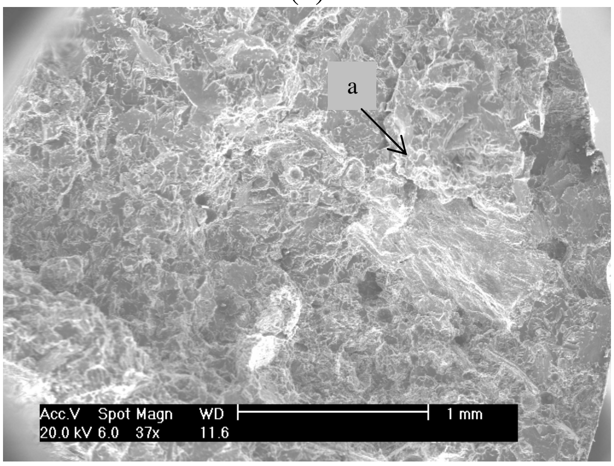

(d)

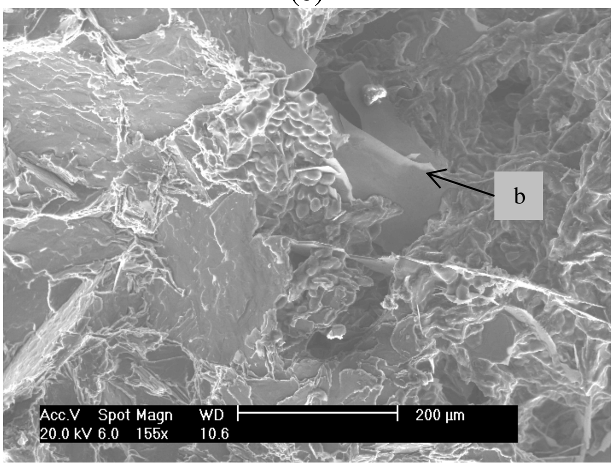

(e)

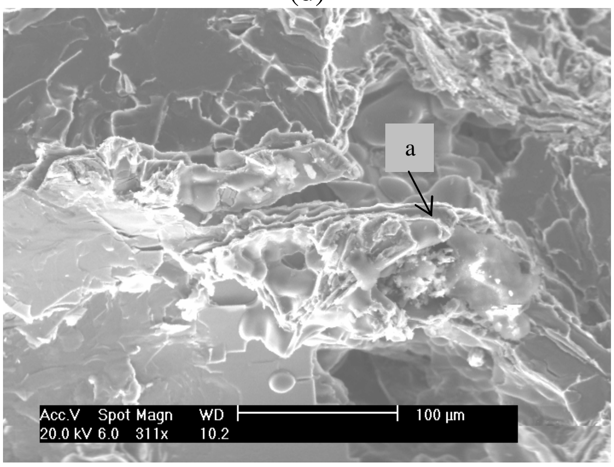

(f)

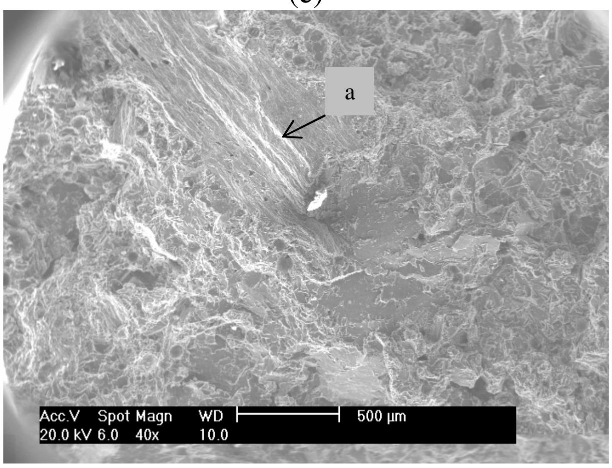

(g)

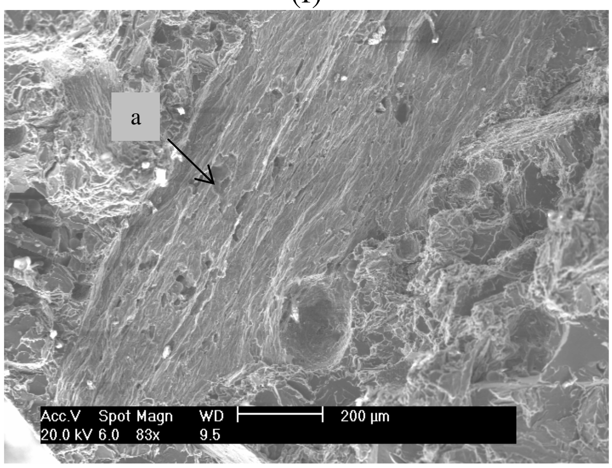

(h)

a: bifilm
b: Fe-phase

Figure 4.73: *SEM pictures from the fracture surface of tensile test bars (LM2 – low Mg)*

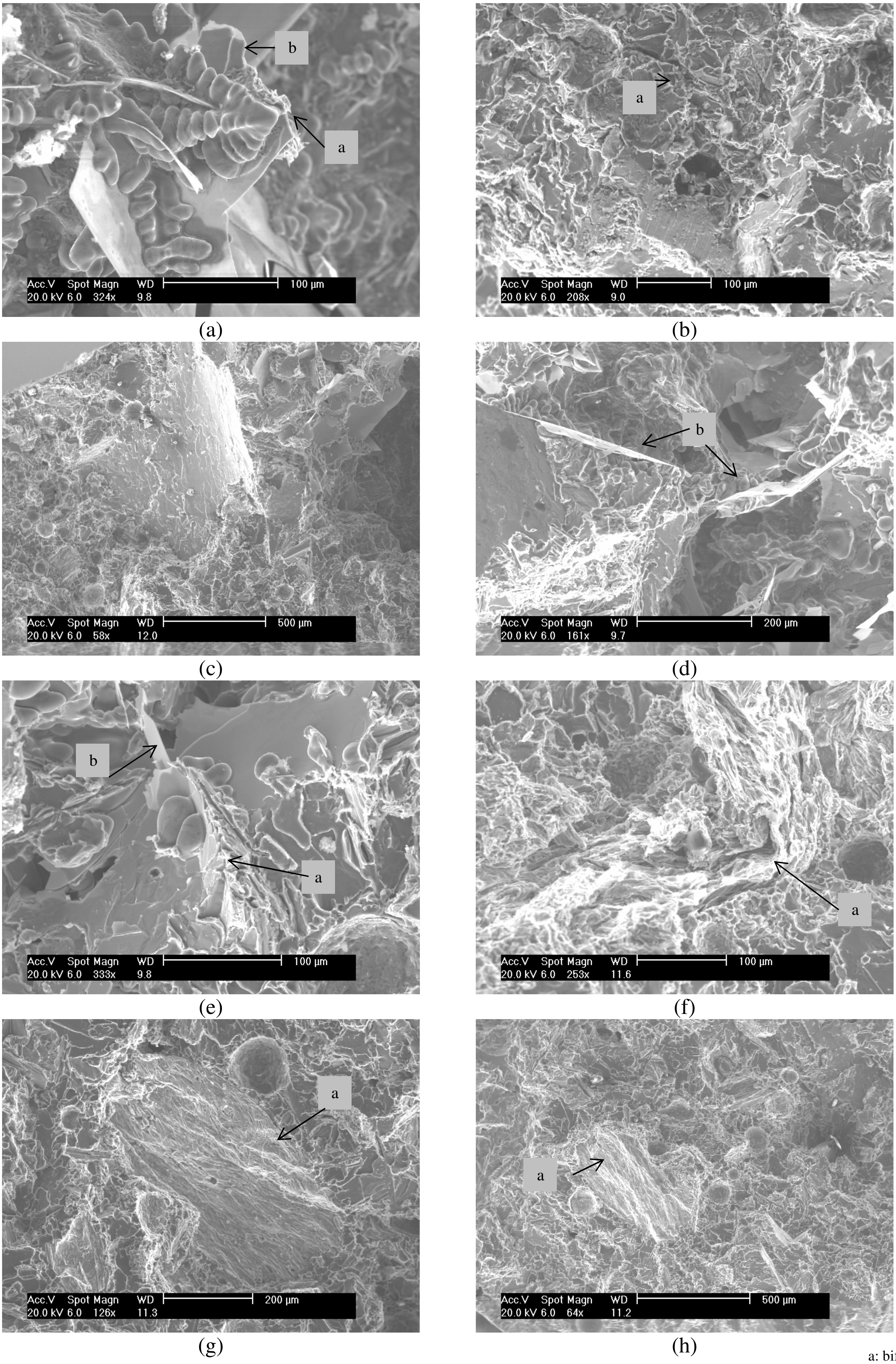

a: bifilm
b: Fe-phase

Figure 4.74: *SEM pictures from the fracture surface of tensile test bars (LM2 – high Mg)*

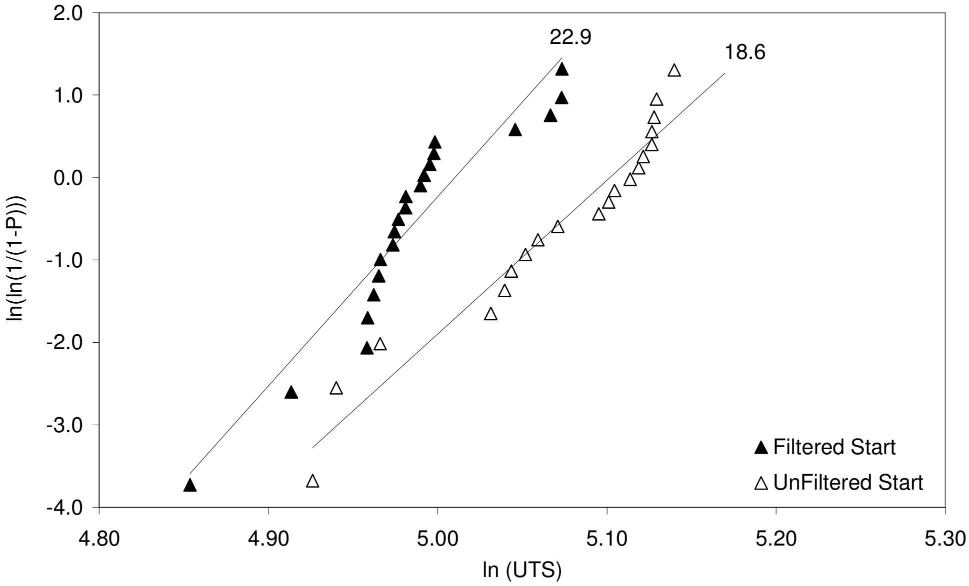

(a)

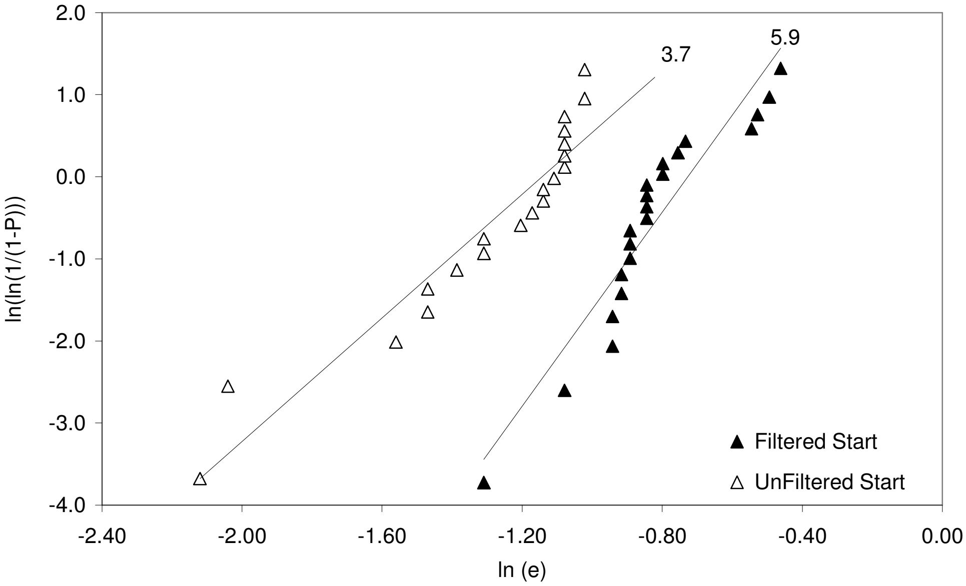

(b)

Figure 4.75: *LM24 comparison of distribution of tensile properties at the start of casting with and without filter (a) UTS, (b) Elongation*

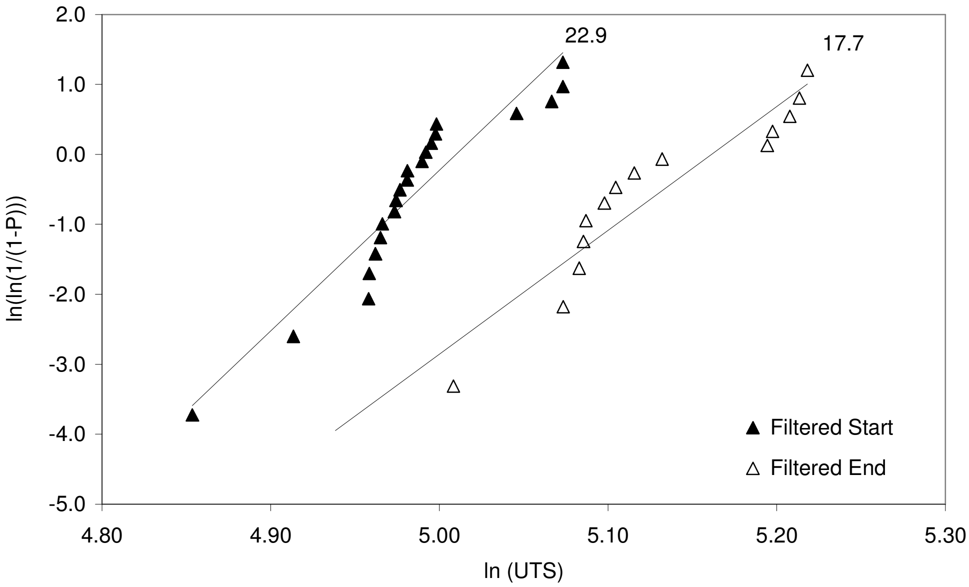

(a)

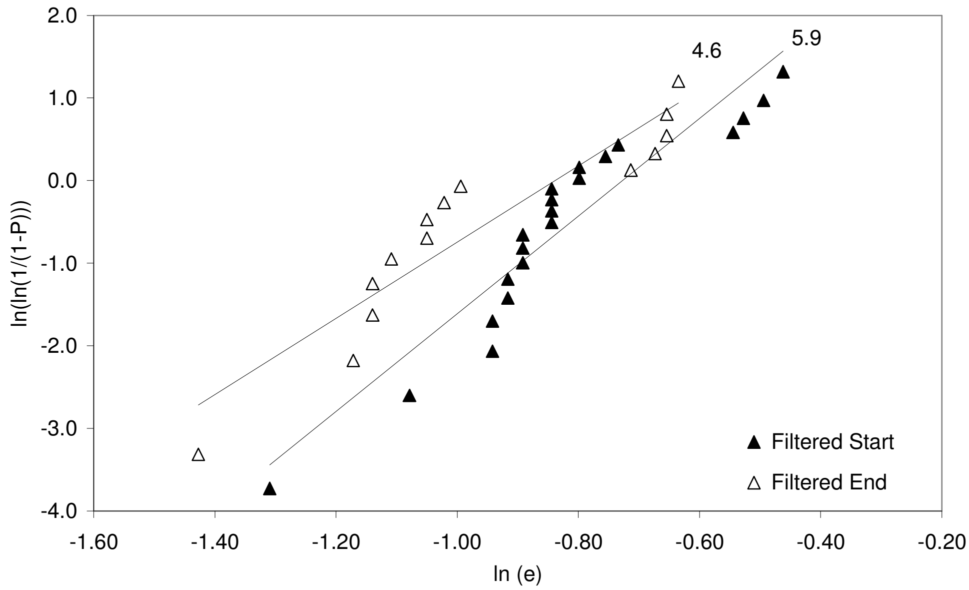

(b)

Figure 4.76: *Alloy LM24: Comparison of the Weibull distributions of strength and elongation at the start and end of casting*
(a) UTS, (b) Elongation

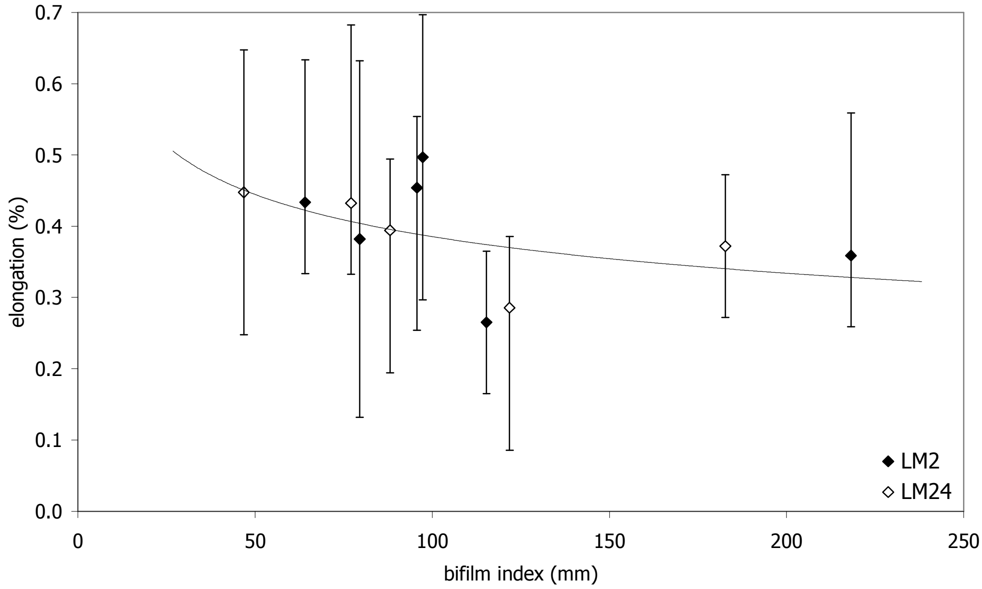

(a)

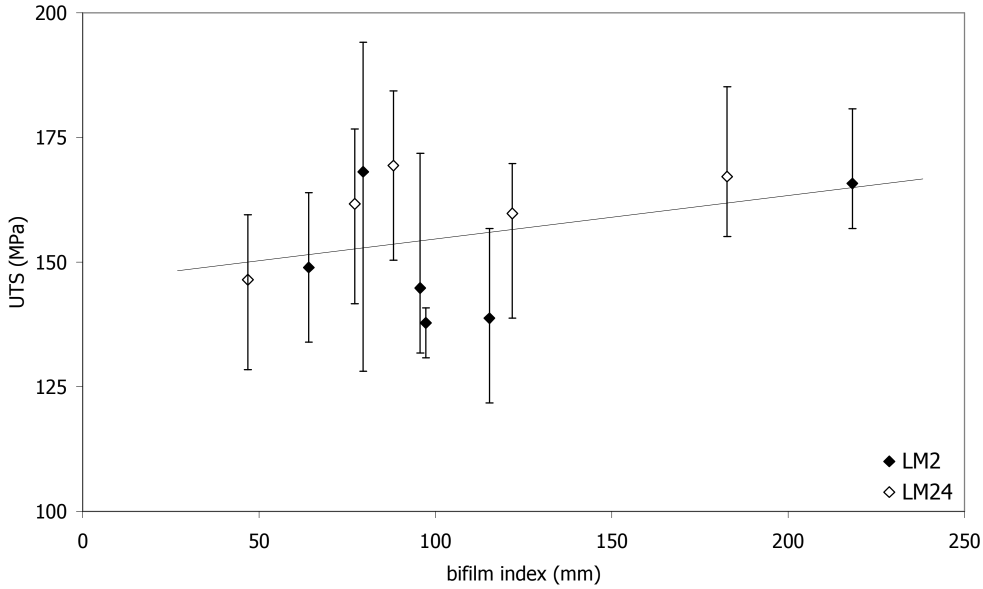

(b)

Figure 4.77: *Relationship between bifilm index (100 mbar) and tensile properties of LM24 and LM2 alloys (a) elongation, (b) UTS*

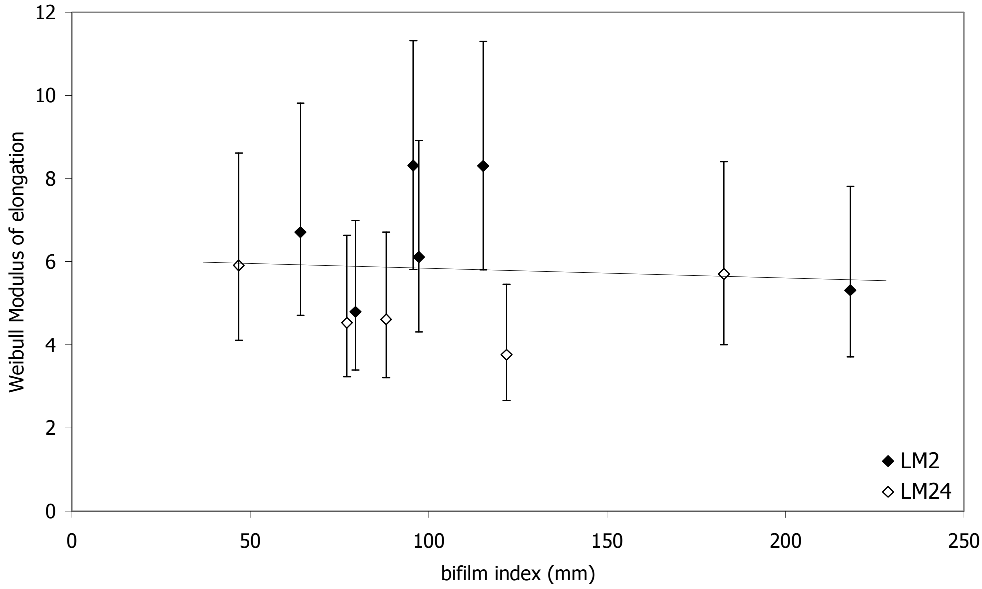

(a)

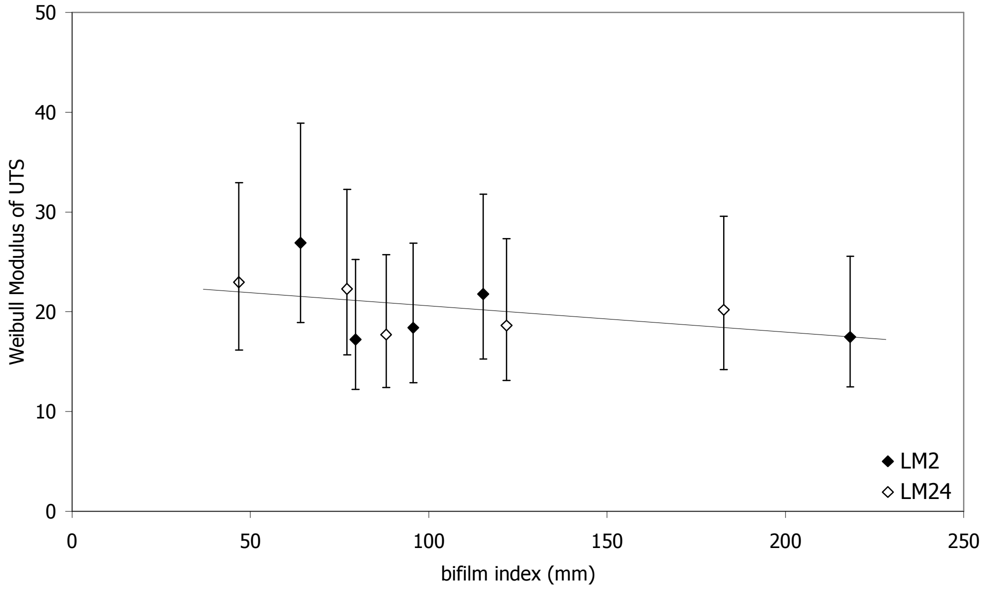

(b)

Figure 4.78: *Bifilm index (100 mbar) change with;*
(a) Weibull modulus of elongation values,
(b) Weibull modulus of UTS values
(the lines are drawn by software as a best-fit)

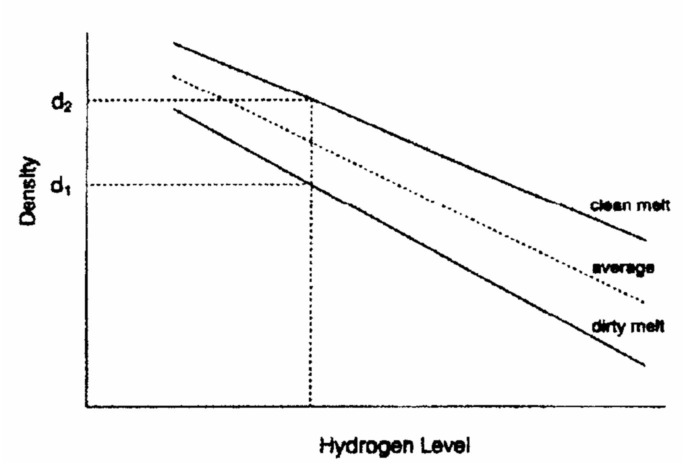

Figure 5.1: *Semi-quantitative predictions of melt cleanliness [246]*

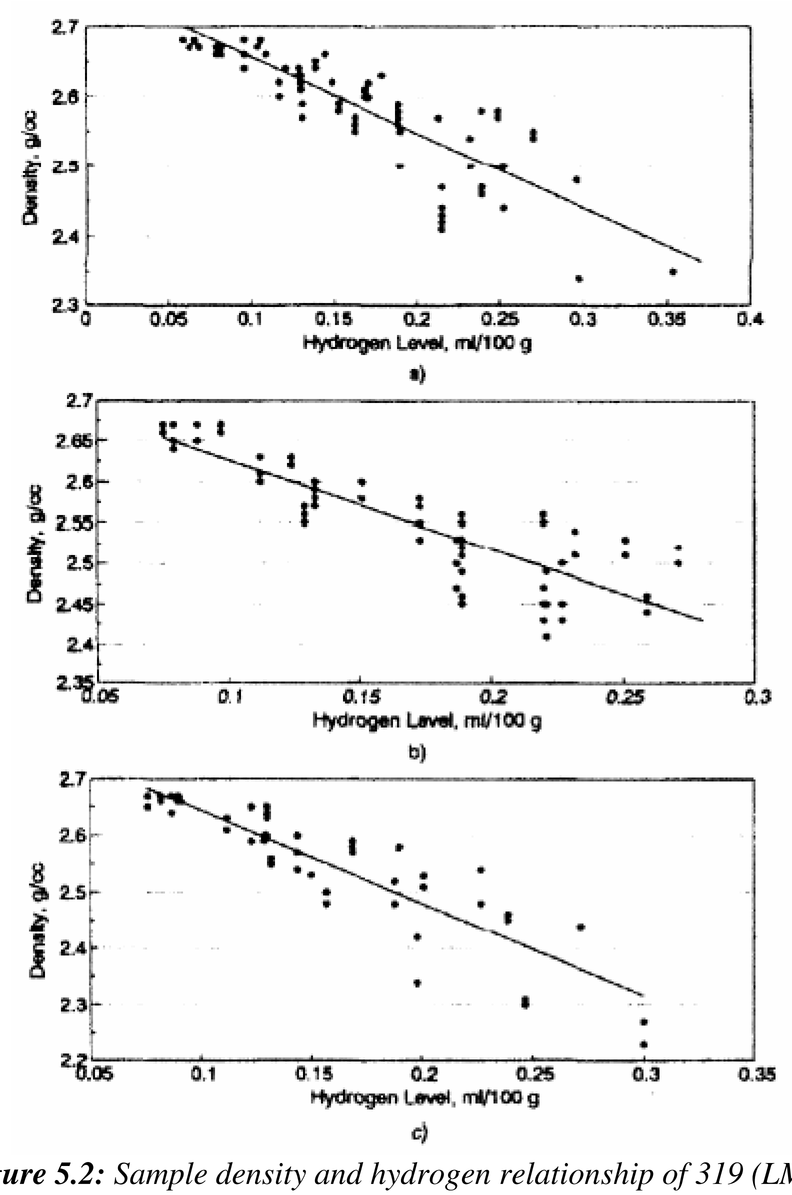

Figure 5.2: *Sample density and hydrogen relationship of 319 (LM24) for various melt treatments (100 mbar)[246]:*
(a) untreated, (b) grain refined, (c) modified

2221 kg/m^3 6.9 mL/kg Al 0-1 hr at 700^{o}C (a)	2523 kg/m^3 5.6 mL/kg Al 1-2 hrs at 800^{o}C (b)	2625 kg/m^3 5.0 mL/kg Al 2-3 hrs at 900^{o}C (c)

Figure 5.3: *The effect of holding time and temperature on pore morphology in alloyLM4 at 10 mbar RPT*

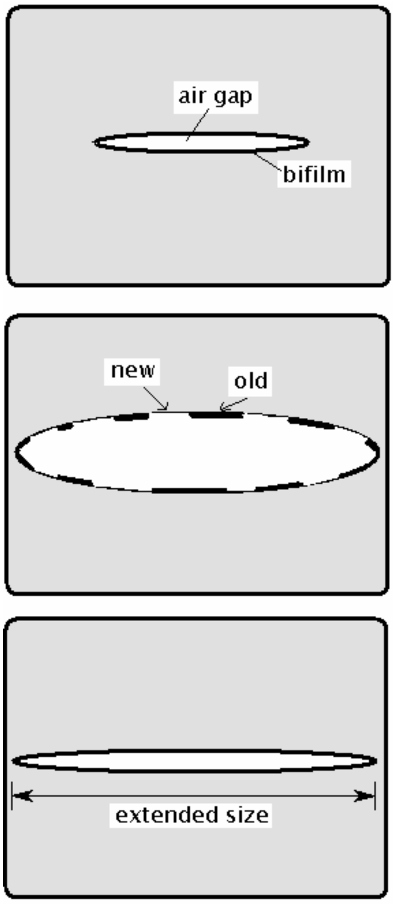

Figure 5.4: *Schematic representation of the ratcheting action:*

(a) air gap between original bifilm
(b) hydrogen diffuses or pressure may change to cause the pore to expand, increasing the area of its oxide film
(c) oxygen in the air gap between the bifilm oxidizes and fixes the new enlarged bifilm area, preventing its return to its original size.

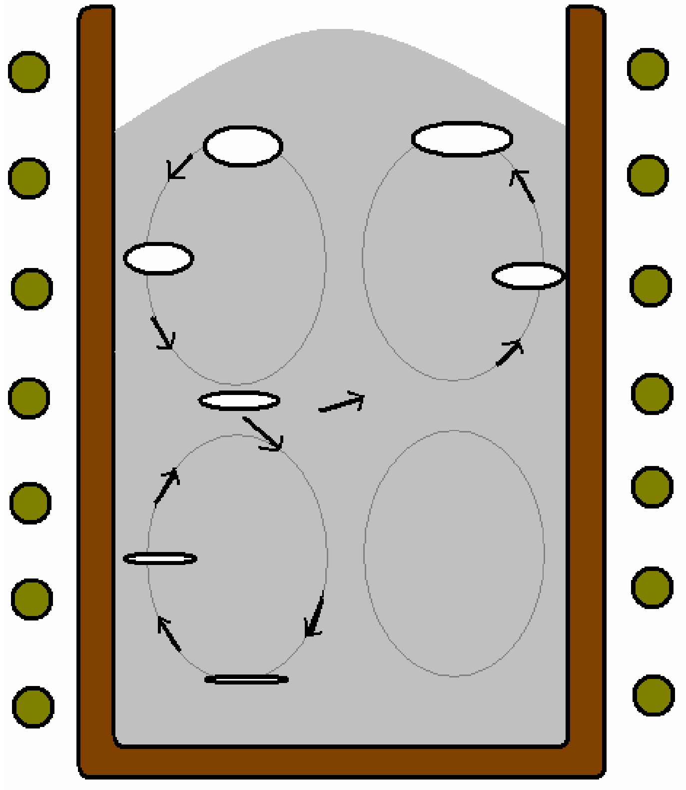

Figure 5.5: *As bifilms are carried from top to bottom of the melt by EM stirring action, they open and close under the cycling metallostatic pressure*

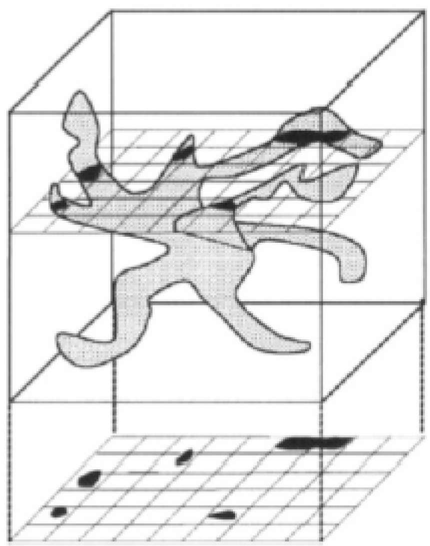

Figure 5.6: *Schematic image of a shrinkage pore in 3D and resulting 2D image [129]*

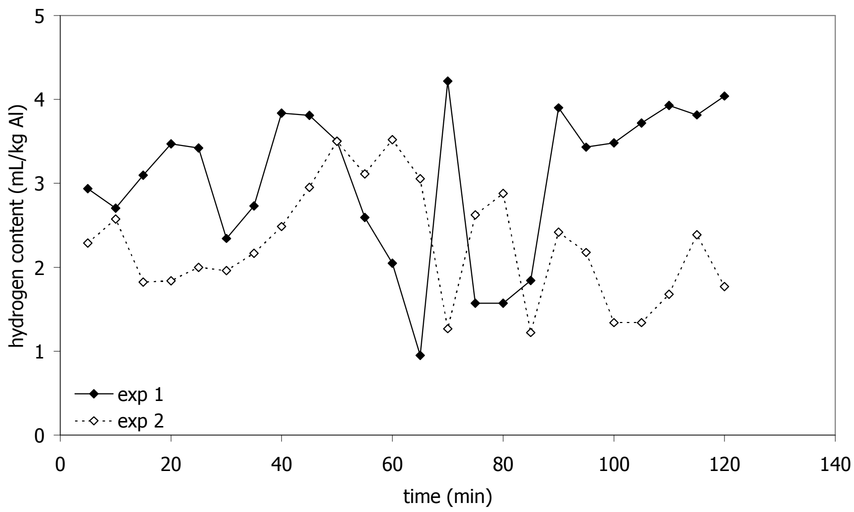

(a)

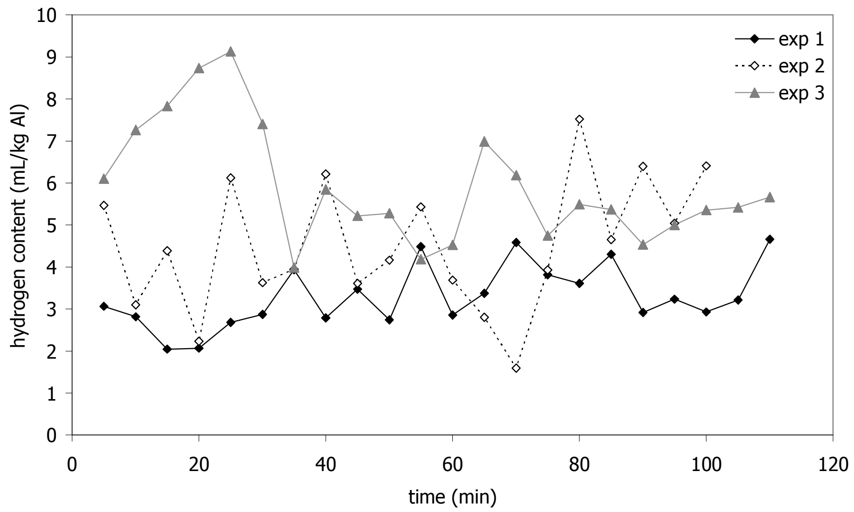

(b)

Figure 5.7: *Hydrogen measurement throughout a sequence of test*

(a) 2different tests from studies with LM4

(b) 3different tests from studies with LM24

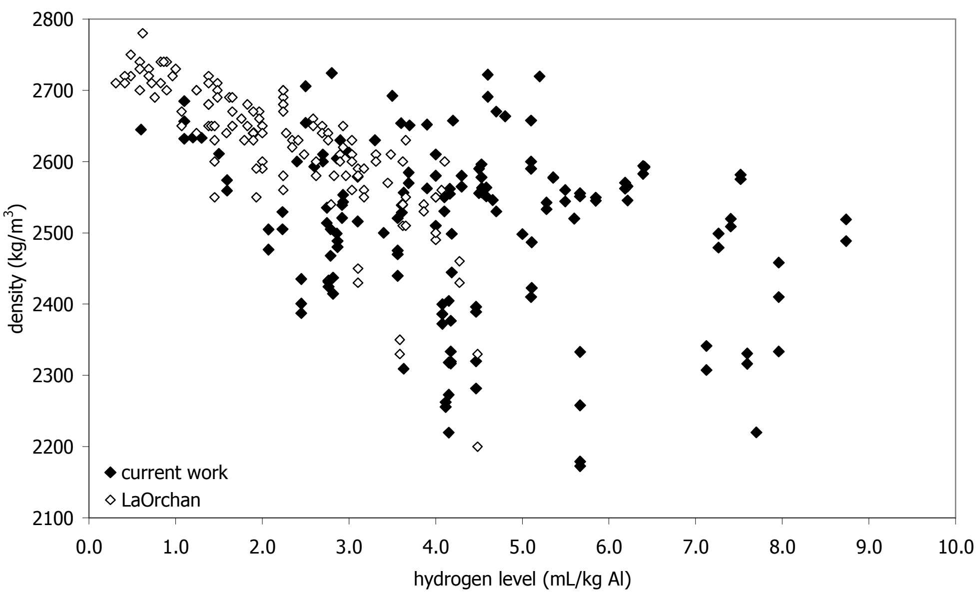

Figure 5.8: *Comparison of LaOrchan's RPT result [240] with the current work*

Table 2.1: *Summary of factors affecting porosity formation in aluminum castings*

Reference	Porosity Formation				
	Hydrogen	Shrinkage	Modification	Surface Tension	Oxides
Piwonka *et al* [108]	Threshold level below which no pore formation is observed	Resistance to flow is important		Additive force on pore formation	
Kubo *et al* [109]	Gas rejection into unfed zones	Limitations to feeding causes pore formation			
Lee *et al* [91-97, 110-117]	Initial hydrogen content and solidification velocity				
Knuutinen *et al* [118-120]		Interdendritic feeding	Eutectic solidification mode is dominant		
Taylor *et al* [121-125]		Feeding range is important	Effects on distribution of porosity	Alloying elements alter surface tension facilitate porosity	
Gruzleski *et al* [84, 87, 102, 126-134]	Linear relationship with porosity	Feeding is important	Increase hydrogen pick up, modifies pore volume but not the amount	Decrease surface tension will facilitate porosity	Oxides and inclusions increase pore

Table 2.1: Summary of factors affecting porosity formation in aluminum castings (cont…)

Samuel *et al* [86, 135-139]	Gas evolution: nucleation starts at base of dendrite arm: geometry and design	Porosity is caused by limitations to feeding			
Tiwari *et al* [140]	Hydrogen is incapable of nucleating in absence of inclusions				Oxides act as potential nucleants
Li *et al* [141-145]	Instead of melt hydrogen level, local solidification kinetics are included in model: hydrogen is needed for nucleation	Negligible		Negligible	
Chen *et al* [89, 146, 147]	Homogenous nucleation not possible, Heterogeneous nucleation on oxides	Depends on hydrogen content		Is a factor to decrease energy for heterogeneous nucleation	Easier bubble formation on oxides
Laslaz *et al* [88]	Hydrogen content does not effect the number but the size of pores		Cleanliness is major factor for pore formation		Pore nucleation on oxides
Kuznetsov *et al* [148]	Initial and threshold hydrogen content	Mushy zone			
Poirier *et al* [103-105, 149, 150]		Interdendritic feeding important: predominant factor in pore formation			
Sigworth *et al* [151-156]		Feeding is dominant factor in pores formation			

Table 2.2: Techniques for oxide detection and measurement [18]:

Tests	Sample weight (grams)	Particle size (μm)
Porous Disk Filtration Analysis (PoDFA) Liquid Aluminium Inclusion Sampler (LAIS) Prefil Footprinter	< 2000 <1000	All sizes
Electric resistivity LiMCA, LiMCA II (Liquid Metal Cleanliness Analyser)	<100	>15
Acoustic detection Signal-noise technique Pulse-echo technique		>10
Electrochemical dissolution	<100	All sizes
Chemical analysis Emission spectroscopy, hot extraction, combustion analysis, neutron activation, gas chromatography	0.5-30	All sizes
Eddy current method	*	*
Capacitance probe	*	*
X-ray detection	Any size	>300
Electromagnetic detection	<200	>10

(* not known)

Table 2.3: Specification of the alloys that are used in the experiments

Alloy	Cu	Mg	Si	Fe	Mn	Ni	Zn	Pb	Sn	Ti	Al
99% Al	0.03	0.03	0.30	0.40	0.03	0.03	0.07	0.03	0.03	-	rem.
LM2	0.7-2.5	0.30	9.0-11.5	1.0	0.5	0.5	0.07	0.3	0.2	0.2	rem.
LM4	2.0-4.0	0.20	4.0-6.0	0.8	0.2-0.6	0.3	0.5	0.1	0.1	0.2	rem.
LM24	3.0-4.0	0.30	7.5-9.5	1.3	0.5	0.5	3.0	0.3	0.2	0.2	rem.
LM25	0.2	0.2-0.6	6.5-7.5	0.5	0.3	0.1	0.1	0.1	0.05	0.2	rem.
LM27	1.5-2.5	0.35	6.0-8.0	0.8	0.2-0.6	0.3	1.0	0.2	0.1	0.2	rem.

Table 2.4: Similar alloy specifications

UK	ASTM (USA)	ISO (Europe)
LM0	150	Al99.5
LM2	384	Al-10Si-2Cu-Fe
LM4	319	Al-5Si-3Cu
LM24	380	Al-8Si-3Cu-Fe
LM25	356	Al-7Si-Mg
LM27	332	Al-7Si-2Cu

Table 2.5: Application area of alloys

Alloy	Application area
LM0	Electrical, food and chemical plant
LM2	Almost any pressure die-cast component
LM4	General engineering, cylinder head, inlet manifold, crankcase, clutch-case, gearbox, engine mounts, tool handle, household fittings, electrical tools, office equipment, mainly used in gravity die casting.
LM24	Engineering die castings, brake components, carburettor parts, axle housing, motor housing, doors, vacuum cleaners, floor polisher, road wheel, mainly used in pressure die casting.
LM25	Aircraft pump parts, aircraft fittings, nuclear energy installations, food equipment, chemical equipment, marine parts, cylinder blocks, cylinder heads, wheels, generally only gravity cast into either dies or sand moulds.
LM27	General engineering components, domestic and office equipment household fittings, electrical tools, car engines, gearbox housing and axle housings, generally cast in gravity dies.

Table 3.1: Composition of the alloys that were used in the experiments

Alloy	Cu	Mg	Si	Fe	Mn	Ni	Zn	Pb	Sn	Ti	Al
99% Al	0.03	0.03	0.30	0.40	0.03	0.03	0.07	0.03	0.03	-	rem.
LM2	2.50	0.30	11.0	0.8	0.25	0.07	0.50	0.05	0.02	0.2	rem.
LM4	3.10	0.06	5.79	0.5	0.17	0.3	0.5	0.1	0.1	0.2	rem.
LM24	3.35	0.06	8.0	0.95	0.5	0.5	2.5	0.3	0.2	0.2	rem.
LM25	0.2	0.6	7.1	0.5	0.3	0.1	0.1	0.1	0.05	0.2	rem.
LM27	2.8	0.38	8.5	0.8	0.34	0.3	0.2	0.2	0.1	0.2	rem.

Table 3.2: RPT test matrix followed in the laboratory

Temperature (^oC)	700	800	900
Pressure (mbar)	10 mbar	10 mbar	10 mbar
	50 mbar	50 mbar	50 mbar
	100 mbar	100 mbar	100 mbar
	200 mbar	200 mbar	200 mbar
	1000 mbar	1000 mbar	1000 mbar

Table 4.1: Weibull modulus of bifilm indices of different alloy and casting conditions

Alloy	RPT Pressure (mbar)	Casting Condition	Average Bifilm index (mm)	Weibull Modulus (m)
LM25	100	Top poured	143.2	1.2
	100	Bottom filled	48.3	1.1
LM24	50	Top poured	196.6	2.6
	50	Bottom filled	138.3	1.1
	100	Top poured	96.8	3.5
	100	Bottom filled	44.2	1.3
LM24	100	Non-Quiescent (0 diffuser)	188.6	3.1
	100	Non-Quiescent (1 diffuser)	110.4	2.5
	100	Non-Quiescent (2 diffusers)	102.9	2.6
LM24	100	Quiescent (0 diffuser)	37.7	0.6
	100	Quiescent (1 diffuser)	52.1	1.7
	100	Quiescent (2 diffusers)	34.6	1.1

Table 4.2: Coordinates of points shown in Figure 4.61

	X-axis (Number of Pores)	Y-axis (Bifilm Index)
Point I	1	100
Point II	100	100
Point III	1	1
Point IV	100	1

Table 4.3: Chemical analysis change from start to end of casting 2.5 ton melt of LM24 from holding furnace

	Cu	Mg	Si	Fe	Mn	Ni	Zn	Pb	Sn	Ti	Al
Start	3.424	0.058	8.168	0.868	0.167	0.053	2.422	0.124	0.104	0.057	rem.
End	3.365	0.057	8.185	0.874	0.163	0.053	2.424	0.124	0.104	0.057	rtem.

Table 4.4: Mechanical test results and Weibull Modulus of alloys LM2 and LM24

Alloy	Bifilm Index[a] (mm)	UTS[b] (MPa)	Weibull Modulus "m"	Proof Stress[b] (MPa)	Weibull Modulus "m"	Elongation[b] (%)	Weibull Modulus "m"
LM2 (Low Mg) (Top Poured)	64.1	148.93	26.90	121.15	38.90	0.43	6.71
LM2 (Low Mg) (Bottom Filled)	95.7	144.79	18.38	116.15	10.09	0.45	8.31
LM2 (High Mg) (Top Poured)	218.2	161.38	17.46	154.61	56.85	0.25	5.31
LM2 (High Mg) (Bottom Filled)	79.5	172.77	17.22	149.0	38.68	0.41	4.79
LM24 (Top Poured)	182.7	167.15	20.18	146.37	40.95	0.37	5.70
LM24 (Bottom Filled)	77.1	161.66	22.27	135.45	25.62	0.43	4.53
LM24 (Filtered) (Start)	46.8	146.46	22.95	119.95	57.97	0.45	5.91
LM24 (Filtered) (End)	88.1	169.33	17.71	145.64	50.41	0.39	4.61
LM24 (UnFiltered) (Start)	121.8	159.75	18.62	146.70	41.81	0.29	3.76

a: For each mechanical test, one Bifilm Index was calculated
b: Values represent averages of 20 bars for each test